Modeling and Measurement of Tissue Compartments with Fast Signal Decay in Whole-Body Magnetic Resonance Imaging

Dissertation

der Mathematisch-Naturwissenschaftlichen Fakultät

der Eberhard Karls Universität Tübingen

zur Erlangung des Grades eines

Doktors der Naturwissenschaften

(Dr. rer. nat.)

vorgelegt von

Anja Maria Fischer

aus Bad Saulgau

Tübingen

2022

Gedruckt mit Genehmigung der Mathematisch-Naturwissenschaftlichen Fakultät der Eberhard Karls Universität Tübingen.

Tag der mündlichen Qualifikation:	04.05.2023
Dekan:	Prof. Dr. Thilo Stehle
1. Berichterstatter:	Prof. Dr. Dr. Fritz Schick
2. Berichterstatter:	Prof. Dr. Klaus Scheffler

Abbreviations

Abbreviation	Explanation
2D	two-dimensional
3D	three-dimensional
ADC	apparent diffusion coefficient
CSI	chemical shift imaging (sequence)
CT	computed tomography
FEM	finite element modeling
FID	free induction decay
FoV	field of view
FT	Fourier transform
FWHM	full width at half maximum
MR	magnetic resonance
MRI	magnetic resonance imaging
MRS	magnetic resonance spectroscopy
MRSI	magnetic resonance spectroscopic imaging (sequence)
NMR	nuclear magnetic resonance
PDCF	proton-density collagen-fraction
PDFF	proton-density fat-fraction
ppm	parts per million
RCS	rotating coordinate system
RF	radio frequency
RHR	ratio between height and radius
ROI	region of interest
SNR	signal to noise ratio
STEAM	simulated echo acquisition mode (sequence)
UTE	ultra-short echo time (sequence)
WRC	water-rich confinements

Symbols

Symbol	Explanation
γ	gyromagnetic ratio
δ	chemical shift
θ	angle between cylinder axis and main magnetic field
$\vec{\mu}, \vec{\mu}_i$	magnetic moment (of nuclear spin)
μ_0	permeability constant
μ_r	relative permeability
μ_z	longitudinal component of the magnetic moment (of nuclear spin)
σ	shielding factor
σ_{ref}	shielding factor of a reference (usually tetramethylsilane for ^{1}H)
$\Delta\chi$	magnetic susceptibility relative to a reference
χ_{bone}	magnetic susceptibility of compact bone
χ_{diff}	magnetic susceptibility difference of two certain materials
χ_m	magnetic susceptibility
χ_{marrow}	magnetic susceptibility of bone marrow/fat
χ_{water}	magnetic susceptibility of water
$\vec{\omega}$	angular velocity
$\Delta\omega$	excitation bandwidth
$\omega_{\mathrm{L}}, \vec{\omega}_L$	Larmor frequency
A_1, A_2, A_3	fit parameter for the share of the respective water component
B_0	magnitude of the applied/external magnetic field
$\vec{B}_0$	applied/external magnetic field
$\vec{B}_1$	magnetic field static in the rotating coordinate system; radio frequency field in laboratory system
ΔB	field gradient
$\vec{B}_e$	magnetic field induced by an electron

$\vec{B}_{\mathrm{eff}}$	effective magnetic field
$\vec{B}_{\mathrm{ext}}$	external magnetic field
$\vec{B}_{\mathrm{lor}}$	magnetic field inside Lorentz sphere
$\vec{B}_{\mathrm{mac}}$	macroscopic magnetic field
$\vec{B}_{\mathrm{rcs}}$	magnetic field acting in the rotating coordinate system
c	offset fit parameter
$\frac{\mathrm{d}}{\mathrm{d}t}$	time derivate
D	apparent diffusion coefficient
ΔE	energy difference between adjacent energy levels of the nuclear spin
E_m, E_{m+1}	energy eigenvalues of the nuclear spin
$\hat{\mathrm{e}}_x$	unit vector along x-axis
$\hat{\mathrm{e}}_y$	unit vector along y-axis
$\hat{\mathrm{e}}_z$	unit vector along z-axis
Δf	frequency difference between spherical and cylindrical component (of free water from cortical bone)
$\emptyset\Delta f$	average of the values obtained for the frequency difference between spherical and cylindrical component
$\emptyset f$	average of the frequencies predicted for spherical and cylindrical pores
$\emptyset f_{\mathrm{2c-lor}}$	average of the free water frequency estimated with the two-component Lorentzian model
$\emptyset f_{\mathrm{cylinder}}$	average frequency of the free water component assigned to cylindrical pores
$\emptyset f_{\mathrm{sphere}}$	average frequency of the free water component assigned to spherical pores
f_{cylinder}	frequency extracted from simulations for the cylindrical pores
f_{sphere}	frequency extracted from simulations for the spherical pores
G_{pe}	phase encoding gradient
G_{ro}	readout gradient

G_{ss}	slice selection gradient
$\vec{H}$	external magnetizing field
$\widehat{H}_z$	additional term of the Hamiltonian for a magnetic field along z-direction
$\hbar$	reduced Planck's quantum of motion
I	quantum number of the nuclear spin (nuclear spin angular momentum)
$\|I, m_I\rangle$	eigenvalue function of the nuclear spin
$\hat{I}_z$	z-component of the spin operator
$\vec{I}$	dimensionless quantity for nuclear spin
$\hat{\vec{I}}$	Spin operator
$\vec{J}$	nuclear spin
k_{B}	Boltzmann's constant
$\vec{M}$	macroscopic magnetization vector
M_0	magnetization of macroscopic magnetization vector in thermal equilibrium
m_I	quantum number of the nuclear spin (spin angular momentum direction)
$M_x(t)$	x-component of macroscopic magnetization vector as function of time
$M_y(t)$	y-component of macroscopic magnetization vector as function of time
$M_z(t)$	z-component of macroscopic magnetization vector as function of time
N_-	energetically lower energy state of the nuclear spin
N_+	energetically higher energy state of the nuclear spin
$R_2{}'$	additional relaxation component in gradient echo sequences due to microscopic field inhomogeneities
RHR	ratio between height and radius
s_1, s_2, s_3	fit parameter for the line width of the respective water component

t	time
T	temperature
t_1, t_2, t_3	fit parameter for the chemical shift of the respective water component
T_1	longitudinal relaxation time constant
T_2	transverse relaxation time constant in spin echo sequences
T_2^*	transverse relaxation time constant in gradient echo sequences
$T_{2,i}^*, T_{2,1}^*, T_{2,2}^*$	transverse relaxation time constant of the respective water component
TD	delay time
TE	echo time
$TE_1, TE_2, \ldots$	certain echoes
ΔT	dwell time
T_{min}	shortest echo time
TM	mixing time (STEAM)
TR	repetition time
x	Fit variable
Δz	slice thickness

Content

Zusammenfassung

Diese Arbeit verfolgt das Ziel, das Signalverhalten von Körperbestandteilen mit raschem Signalabfall in der Ganzkörper-Magnetresonanztomographie zu charakterisieren. Das erste Kapitel bietet daher eine Zusammenfassung der physikalischen Grundlagen der Magnetresonanz. Des Weiteren findet sich in diesem Kapitel ein Überblick über verschiedene Einflussfaktoren, welche zu einem charakteristischen Signal bestimmter Bestandteile beitragen, beispielsweise aufgrund deren chemischer Umgebung oder Geometrie. Im Anschluss folgt ein Abschnitt zu den grundlegenden Elementen von Magnetresonanz-tomographiesequenzen, in welchem abschließend auf die Möglichkeit ultrakurzer Echozeiten eingegangen wird. Im darauffolgenden zweiten Kapitel erfolgt die Modellierung eines möglichen Wassersignals im entzündeten Fettgewebe. Dafür wird die charakteristische Geometrie der zwischen Adipozyten liegenden Wassereinschlüsse genutzt, um mittels Simulationen und Phantommessungen Rückschlüsse auf das Relaxationsverhalten und somit die Messbarkeit des Wassersignals zu ziehen. Aus den Ergebnissen kann geschlossen werden, dass für die Detektion dieser schnell relaxierenden Signale kurze Echozeiten notwendig sind. Diese bietet beispielsweise eine im dritten Kapitel eingeführte Methode, welche auf Grundlage von speziellen Bilddatensätzen mit ultrakurzen Echozeiten die Berechnung von Spektren ermöglicht. Basierend auf diesen Spektren erfolgt eine Charakterisierung des Kollagensignals. Mit dem entwickelten Signalmodell gelingt es im Anschluss, Kollagen in wässrigen Lösungen ab einem Massenanteil von 2-4% nachzuweisen. Diese Werte liegen in einem Bereich, welcher beispielsweise für die Einstufung der Fibrosierung im Lebergewebe relevant wäre. Das Verfahren zur Berechnung räumlich aufgelöster Spektren unter Verwendung ultrakurzen Echozeiten findet auch im vierten Kapitel Anwendung, in welchem die Modellierung des aus dem kompakten Knochen stammenden Wassersignals vorgestellt wird. Dabei lassen sich verschiedene Kompartimente unterscheiden. Normalerweise erfolgt eine Trennung von gebundenem und frei in porösen Strukturen vorliegendem Wasser. Dies gelingt typischerweise basierend auf unterschiedlichen Relaxationszeiten der Kompartimente. In diesem Abschnitt wird postuliert, dass sich das freie Wasser aufgrund der Geometrie der formgebenden Strukturen in Signalanteile mit unterschiedlichen Frequenzen unterteilen lässt.

Diese Hypothese wird mithilfe der neuen Methode überprüft. In einem letzten Kapitel werden die Ergebnisse der einzelnen Kapitel zusammenfassend diskutiert.

Summary

The aim of this thesis is to characterize the signal behavior of tissue components with fast signal decay in whole-body magnetic resonance imaging. Therefore, the first chapter contains a summary of the physical basics of magnetic resonance. Furthermore, this chapter provides an overview of various influencing factors that contribute to a characteristic signal of certain components, for example their chemical environment or geometry. This is followed by a section on basic elements of magnetic resonance sequences, which concludes with a description of the possibility of ultra-short echo times. In the following second chapter, the modeling of a possible water signal in inflamed adipose tissue is performed. For this purpose, the characteristic geometry of the water inclusions located between adipocytes is exploited to draw conclusions about the relaxation behavior and, thus, the measurability of the water signal by means of simulations and phantom measurements. It can be concluded that short echo times are necessary for detection of these fast-relaxing components. This is provided, for example, by a newly introduced method in the third chapter, which allows for the calculation of spectra based on specific imaging data sets with ultra-short echo times. Based on this approach, a characterization of the collagen signal is performed. With the resulting signal model, collagen in aqueous solution can be detected starting at a mass fraction of 2-4%. These values are attributable to a range which would be relevant, for example, for the staging of fibrosis in liver tissue. The method of calculating spatially resolved spectra using ultra-short echo times is also applied in the fourth chapter. In this chapter, modeling of the water signal originating from compact bone is performed. Thereby, different compartments can be distinguished. Usually, bound water is separated from free water present in porous structures. This typically results due to the different relaxation times of the compartments. In this section, it is postulated that the free water can be further subdivided into signal components with different frequencies based on the geometry of the shaping structures. This hypothesis is tested using the newly proposed method. In a final section, the results of the individual chapters are discussed in summary.

List of publications and declaration of the framework of the collective work

Elements of this dissertation have been published or submitted for publication as collective work in peer-reviewed journals. In the following an overview of the contributions of the involved authors is provided.

I. Towards detection of inflammation in adipose tissue: Microscopic field simulations to estimate water signal properties

published in Zeitschrift für Medizinische Physik 2021, 31(4):394-403

Anja Fischer	Corresponding and first author, conception and execution of the study, data acquisition, processing, and analysis, writing of the manuscript
Fritz Schick	Supervision of the project, critical discussion of the results, proofreading of the manuscript, study conception

II. Spatially resolved free-induction decay spectroscopy using a 3D ultra-short echo time multi-echo imaging sequence with systematic shifting and compensation of B_0 field drifts

published in Magnetic Resonance in Medicine 2022, 87(5):2099-2110

Anja Fischer	Corresponding and first author, conception and execution of the study, data acquisition, processing, and analysis, writing of the manuscript
Petros Martirosian	Advice and support in MR data acquisition, critical discussion of the results, proofreading of the manuscript
Thomas Benkert	Advice and support in MR data acquisition, critical discussion of the results, proofreading of the manuscript
Fritz Schick	Supervision of the project, critical discussion of the results, proofreading of the manuscript, study conception

III. Frequency shifts of free water signals from compact bone – Simulations and measurements using a UTE-FID sequence

submitted to Magnetic Resonance in Medicine

Anja Fischer	Corresponding and first author, conception and execution of the study, data acquisition, processing, and analysis, writing of the manuscript
Petros Martirosian	Advice and support in MR data acquisition, critical discussion of the results, proofreading of the manuscript
Jürgen Machann	Advice and support in MR data interpretation, critical discussion of the results, proofreading of the manuscript
Bernd Fränkle	Visualization
Fritz Schick	Supervision of the project, critical discussion of the results, proofreading of the manuscript, study conception

Introduction

“The best that most of us can hope to achieve in physics is simply to misunderstand at a deeper level.”

— Wolfgang Ernst Pauli

When Wolfgang Ernst Pauli postulated the existence of a nuclear magnetic moment in 1924 (1), he probably did not imagine this phenomenon to establish the basis for one of the most important imaging modalities in modern medicine almost a century later: In 2020, the number of magnetic resonance (MR) scans performed in Germany per 1 000 citizens amounted to 149.9 and has, thus, more than doubled within 15 years (2). In the meantime, many more discoveries and innovations were required, which culminated in five Nobel Prizes (3; 4). The first one was awarded to Isidor Isaac Rabi "for his resonance method for recording the magnetic properties of atomic nuclei" (5). Therefore, a beam of molecules with a common nuclear spin orientation is selected by an inhomogeneous magnetic field. In addition to a subsequent homogeneous magnetic field a small oscillating field with variable frequency is applied. The resulting beam is again decoupled to access changes in the magnetic moment (6). This effect of magnetic resonance reported for molecular beams was applied to solids and fluids by two research groups independently (7; 8; 9). For their discovery of this phenomenon both, Felix Bloch, and Edward Mills Purcell, were jointly awarded the Nobel Prize in Physics 1952 (10). While the first two Laureates dealt with nuclear physics and the development thereof the research that resulted in the further Nobel Prizes concerned the application of nuclear magnetic resonance (NMR). The first field of application is to be assigned to (bio)chemistry. Since the resonance frequency of the nuclear magnetic spin is characteristic for specific atoms and furthermore their environment, the determination of the resonance frequency allows conclusions to be drawn about the structure and composition of molecules. For contributing to the development of this so-called high resolution NMR spectroscopy and the application to assess the three-dimensional (3D) structure of biological macromolecules the Nobel Prizes in chemistry 1991 and 2002 honored Richard Robert Ernst and Kurt Wüthrich (11; 12). Through the seminal discoveries by Paul Christian Lauterbur and Sir Peter Mansfield this method was transferred into an

imaging method (3). They proved independently that an additional magnetic field gradient allows to obtain information on the spatial distribution of water filled capillaries and layers of synthetic camphor, respectively (13; 14). Furthermore, Lauterbur claimed that different longitudinal relaxation times can be visualized by his so-called “zeugmatography” (13). When these methods were combined with the findings of changes in the relaxation behavior of malignant tumors by Raymond Damadian the way for an application in medical diagnostics was paved (15). In 2003, Lauterbur and Mansfield were jointly rewarded with the Nobel Laureate in Physiology or Medicine after their basic idea became an established imaging method in medicine (3; 4).

Despite a time lead of approximately 10 years of computed tomography (CT) regarding the first clinical installation, magnetic resonance imaging (MRI) has nevertheless established itself due to various advantages (16). First, in contrast to CT, MRI offers an imaging method free of ionizing radiation. Thus, this method is preferred especially for younger patients and allows an arbitrary repetition of the measurement (17). Furthermore, MRI exhibits an improved soft tissue contrast: In CT the grayscale of the images is defined in terms of Hounsfield-Units, which depend on the linear attenuation coefficient of the respective tissue (18). Thus, the image contrast solely depends on a physical parameter which displays only slight variations in soft tissue. By contrast, the differences of the longitudinal relaxation behavior mentioned by Lauterbur represent only one of many influencing factors in MRI (13; 19). In addition to the longitudinal relaxation behavior (referred to by the time constant T_1), the so-called transverse relaxation characteristics (represented by T_2 or T_2^* depending on the MR sequence) and the density of signal-producing nuclei form the basic contrasts in MRI. Since for medical diagnostics almost solely ^1H nuclei are considered, the latter contrast is mostly referred to as proton density. To obtain images with a defined contrast (i.e., T_1-, T_2- or proton density-weighting) the timing of the field gradients and radio frequency (RF) pulses is relevant. Therefore, two time constants in the applied sequence are of particular importance: echo time (TE) and repetition time (TR). The echo time describes the time between RF excitation and readout of the signal, whereas the repetition time is defined as the time that elapses between consecutive excitation of the same sample region. T_1-weighted tissue contrast is obtained for short TE and TR. This contrast is in

particular relevant when acquiring anatomical images (19). For longer TR, images are more dependent on the proton density (i.e., long TR and short TE), whereas long TR and long TE result in a T_2-weighted contrast. The latter is beneficial for the detection of pathological changes as present for edema and tumors which are characterized by markedly longer T_2 times compared to healthy (lean) tissue (19). Nevertheless, a sequence never solely depends upon one parameter and proton density for example also influences T_1- and T_2-wheighted images (20; 21).

A further influencing factor which is in particular important for magnetic resonance spectroscopy (MRS) is the chemical shift. Depending on the environment, the magnetic flux density at the location of the nucleus is altered and, thus, the resonance frequency allows to draw conclusions about the chemical structures. Furthermore, this difference in frequency is also exploited for imaging methods: Signals with distinct but different precession frequencies are observable as changing superposition states over time. The signal contribution of the individual frequency component can then be reconstructed acquiring so-called gradient echo images with different echo times. This principle was first applied by William Thomas Dixon to calculate fat and water images based on an in-phase and an opposed-phase image (22). Today, the so-called Dixon method has a wide range of applications and is used for fat suppression as well as for quantification of fat content or different fat compartments (23). However, chemical shift is also a source of image artifacts. As mentioned before, Lauterbur and Mansfield exploited magnetic field gradients to obtain spatial information (13; 14). As a consequence of the application of the gradient, the resonance frequency becomes location dependent and, thus, a reconstruction of the spatial origin of the signal based on Fourier transform (FT) is feasible. Yet, presence of components with different chemical shift results in an incorrect spatial assignment of the signals. The best-known consequence thereof is the fat-water-shift in Cartesian sampled images which is evident as a slight misalignment of fat containing tissues (24).

Alterations of the magnetic field might also occur on scales which exceed the molecular dimensions due to the underlying materials and interfaces thereof. The magnetic flux density within a distinct material depends on its magnetic susceptibility. Thereby, materials with an increased magnetic field are distinguished from the so-called diamagnetic materials with decreased magnetic

flux density. Almost all tissues in living organisms are attributable to the latter. Nevertheless, slight variations between different tissues are evident, whereof bulk magnetic susceptibility effects might occur. Thus, depending on the geometry of the materials with different susceptibilities, the magnetic field is altered. Therefore, different geometries of a distinct material might result in different magnetic resonance frequencies. In 1993, this effect was reported for the methylene signal in skeletal muscles, where two signal components are observable for parallel orientation of the muscle to the external magnetic field (25). As a consequence, spherical lipid droplets referred to as intramyocellular lipids are distinguishable from lipids stored in cylindrical structures between the muscle fibers (extramyocellular lipids). In addition to frequency shifts, susceptibility differences also cause field inhomogeneities. This is for example the case in the lung parenchyma and results in a significant shortening of the transverse relaxation time (26). Therefore, the lung parenchyma is not accessable with standard imaging sequences since the MR signal has already vanished until the echo is read out. Thus, a necessity for realization of sequences capable of minimizing TE arose which was finally met with the invention of ultra-short echo time (UTE) MRI with TEs of less than 100 µs (27; 28). While this method was initially intended for the lung it also provides benefits for other tissues or tissue components with short relaxation times as for example tendons or bones as well as macromolecules such as collagen which is present in fibrotic tissue (29; 30; 31). In addition to an ultra-short relaxation time, collagen also exhibits frequency contributions that deviate from the water signal (31). Different frequency distributions are easiest to differentiate with MRS. However, available spatially selective MRS methods require TEs of a few milliseconds. Thus, in Part II of this thesis a method is developed that allows for the calculation of MR spectra based on UTE images. Furthermore, this thesis aims to characterize different chemical body components regarding the effects previously described.

Objective

It is the aim of this work to predict and characterize the MR signal behavior of body components with fast signal decay. These also include chronic inflammation and fibrosis as important elements of pathological tissue changes, which are often difficult to diagnose (except by biopsy). To establish new diagnostic methods for the detection of early changes of a disease it is crucial to possess a basic understanding of the consequences on the MR signal resulting from alterations in the structure of respective tissues. As mentioned before, the MR signal depends on multiple different factors as for example relaxation behavior, chemical shift effects, magnetic susceptibility, and geometry. The present thesis is composed of three parts with each part covering the characterization of an MR signal of a different body component.

- Part I: This part focusses on adipose tissue, to be more precise: on the water component of inflamed adipose tissue. It is assumed that water-rich immune cells as well as free fluids accumulate in the extracellular spaces between adipocytes. Therefore, characteristic water inclusions develop between the approximately spherical adipocytes. The study aims to determine the magnetic field distribution in these inclusions by simulations and phantom measurements to draw conclusions about the relaxation behavior of a potential water component in inflamed adipose tissue.
- Part II: The objective of this part is to establish a new method which calculates spatially selective MR spectra based on UTE images. This method aims to assess the different frequency components of fast relaxing components as for example collagen as present in fibrotic tissue. Furthermore, the MR signal pattern of a collagen aqueous solution is characterized. Based on this pattern an estimation of the proton-density collagen-fraction (PDCF) in the style of the Dixon method is performed.
- Part III: This part has the aim to characterize the water signal originating from cortical bone. The water signal in cortical bone originates from porous structures (free water) and from bound water. While a differentiation of these two water components and their significance on bone structure and stability has been widely reported, the present approach aims on a further

characterization of the free water signal. This is postulated to originate from cylindrical and spherical porous structures which due to the susceptibility difference of compact bone and water result in two merging resonance lines. Dependent on the orientation of the bone in the magnetic field predictions on the resonance frequency of the two compartments are extracted from finite element modeling (FEM) and analytical simulations. A verification of this model is performed based on the method newly introduced in Part II.

1. Background

The objective of this chapter is to provide an understanding of the basic physical principles underlying MRI and MRS. Therefore, at first the nuclear spin and its interactions in a magnetic field are considered before moving on to the methods (including the UTE-sequence) applied in the subsequent chapters.

Nuclear Spin

The nuclear spin is a feature of the nucleus and consists of the angular momentum and spins of its components, namely protons and neutrons. Since these components cancel each other in the case of an even number of both, neutrons, and protons, not all nuclei are accessible via magnetic resonance (32). However, the most abundant element in the human body, hydrogen, exhibits nuclei consisting of a single proton only, and is, thus, the element which is almost exclusively considered for MRI in humans (17; 33). For this reason, the following paragraphs solely consider ^{1}H-nuclei.

For better illustration, the nuclear spin is sometimes described as the angular momentum of the nucleus. Simultaneously, the nucleus consists of charged particles. In a classical understanding, the combination of these two features necessarily results in a magnetic moment. Correspondingly, the nuclear spin $\vec{J}$ is associated with a magnetic moment according to

$$\vec{\mu} = \gamma \vec{J} = \gamma \hbar \vec{I} \qquad 1$$

with the gyromagnetic ratio γ as a nucleus-specific proportionality constant (17; 19; 34). Subsequently, the dimensionless quantity $\vec{I}$ is used, which results from the nuclear spin $\vec{J}$ by means of the reduced Planck's quantum of action $\hbar$.

When considering the quantum mechanical nuclear spin, it is fundamental that it can only take certain states. Thereby, the number of these states is dictated by the quantum number I via the relation $2I + 1$ (32; 34). Thus, for hydrogen with $I = {}^{1}/_{2}$ two of these so-called eigenstates result. These eigenstates are degenerate, which means that they exhibit the same energy. However, this changes when an external magnetic field is applied:

In an external magnetic field $\vec{B}_0 = B_0\hat{e}_z$, an additional term is added to the Hamiltonian

$$\hat{H}_z = -\vec{\mu} \cdot \vec{B}_0 = -\gamma\hbar\hat{\vec{I}} \cdot \vec{B}_0 = -\gamma\hbar\hat{I}_z \cdot B_0 \qquad 2$$

with the spin operator $\hat{\vec{I}}$ and its z-component $\hat{I}_z$ (34; 17). These relate to the eigenvalue function $|I, m_I\rangle$ by the eigenvalue equations

$$\hat{\vec{I}}^2|I, m_I\rangle = I(I+1)|I, m_I\rangle \text{ and } \hat{I}_z|I, m_I\rangle = m_I|I, m_I\rangle \qquad 3$$

with the quantum numbers I and m_I. For a certain nucleus with fixed I, m_I can take $2I+1$ values with integer spacing between $-I$ and I. Thus, for hydrogen the possible values for m_I are limited to $-{}^1/_2$ and ${}^1/_2$ (17). When inserting the second eigenvalue equation into the additional term of the Hamiltonian

$$\hat{H}_z|I, m_I\rangle = -\gamma\hbar\hat{I}_z B_0|I, m_I\rangle = -\gamma\hbar m_I B_0|I, m_I\rangle \qquad 4$$

conclusions about the energy eigenvalues E_m can be drawn

$$E_m = -\gamma\hbar m_I B_0 \text{ (17).} \qquad 5$$

Consequently, the degeneracy of the eigenstates in the external magnetic field is cancelled according to Zeeman splitting and the energy difference between adjacent energy levels can be calculated by

$$\Delta E = E_m - E_{m+1} = -\gamma\hbar m_I B_0 + \gamma\hbar(m_I + 1)B_0 = \gamma\hbar B_0 = \hbar\omega_{\mathrm{L}} \text{ (17).} \qquad 6$$

Accordingly, the energy difference grows proportionally to the magnetic flux density which - by the relation $\omega_{\mathrm{L}} = \gamma B_0$ - can be transformed into a dependency upon the Larmor frequency ω_{L} (35; 36; 19). The latter describes the precession frequency of the nuclear spin in a certain external magnetic field. Furthermore, transitions between adjacent energy levels take place under emission or absorption of an energy quantum, a so-called photon, whose electromagnetic frequency coincides with the Larmor frequency (36). Two energy levels are accessible for hydrogen nuclei which are referred to with N_+ and N_- for the energetically higher and lower state, respectively. The ratio between these two states is given by the Boltzmann distribution

$$\frac{N_+}{N_-} = \exp\left(-\frac{\Delta E}{k_B T}\right) \qquad 7$$

and in addition to the energy difference depends upon the absolute temperature T and the Boltzmann's constant $k_B \approx 1.381 \cdot 10^{-23}$ JK^{-1} (19; 32). Therefore, with a rising energy gap, an increasing surplus of the energetically more favorable spin state builds up. This surplus is accessible during MR experiments as the so-called macroscopic magnetization which is subject to the laws of classical physics (37).

Macroscopic Magnetization and RF Pulses

The macroscopic magnetization vector $\vec{M}$ is calculated according to the superposition principle as the sum of the magnetic moments $\vec{\mu}_i$ of the nuclear spins (32). However, only those ^{1}H-nuclei are considered which contribute to the signal of a particular volume segment and exhibit a certain common environment, and, thus, the same restrictions and properties as for example a shared Larmor frequency. Nuclei with differing features are considered by further magnetization vectors which in turn superimpose themselves. The nuclear spin of hydrogen nuclei is restricted to two discrete eigenstates, and this also holds for the magnetic moment which can take two opposing orientations (17; 32). However, these orientations are not aligned strictly parallel or antiparallel to the external magnetic field but are rather tilted by a certain angle with respect to the magnetic field. Thus, the magnetic moment possesses a transverse component (perpendicular to the magnetic field and therefore in the x-y-plane) which causes a precession around the axis of the magnetic field as depicted in Figure 1a (32).

The gyromagnetic ratio dictates the frequency of this precession for a specified magnetic field. For hydrogen nuclei the gyromagnetic ratio γ amounts to 42.577 MHzT^{-1}, wherefore the energetically beneficial eigenstate N_- is present for the longitudinal component of the magnetic moment μ_z aligned parallel to the magnetic field (17). For this reason, this state dominates in thermal equilibrium according to Equation 7 whereby the excess increases with decreasing temperature T. Furthermore, the magnetic moments are not precessing in resonance, wherefore the transverse component is canceled to zero when considering the totality of spins contributing to the macroscopic magnetization vector (37). Thus, a net magnetization aligned parallel to the main magnetic field

results (32). The formation of the macroscopic magnetization is schematized in Figure 1b. For a sufficient number of spins, and under the assumption of a lacking interaction between them, the macroscopic magnetization vector which represents the average of the ensemble of magnetic moments also represents the expectation value of the individual magnetic moment. Therefore, in contrast to the magnetic moments themselves, the macroscopic magnetization vector is not restricted to discrete values but can change continuously (37).

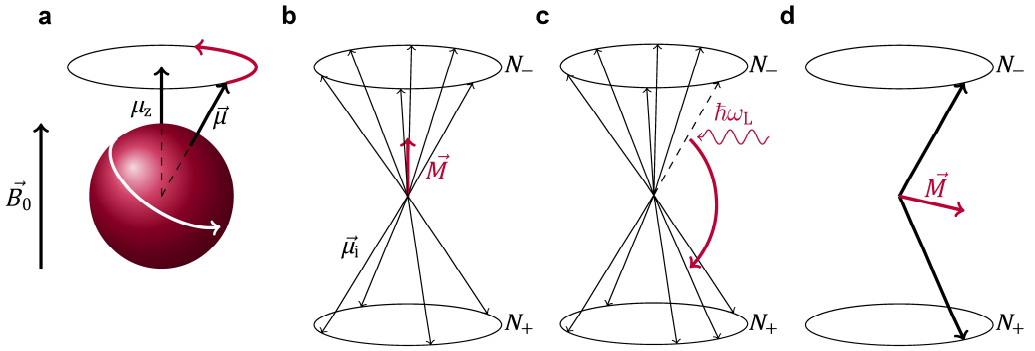

Figure 1.a. The nuclear spin is associated with a magnetic moment $\vec{\mu}$. In an external magnetic field $\vec{B}_0$ the transverse component of the magnetic moment causes a precession thereof around the axis of the magnetic field. Thus, the time average of the magnetic moment is equivalent to its longitudinal component μ_z. Adapted from (32). b. The macroscopic magnetization vector $\vec{M}$ is obtained by superimposing the magnetic moments $\vec{\mu}_i$ of an ensemble of spins. In the thermal equilibrium a surplus of the energetically beneficial state results in a macroscopic magnetization parallel to the main magnetic field. Adapted from (32). c. Transitions to the energetically higher eigenstate can be induced by an RF pulse with Larmor frequency. Thus, the longitudinal magnetization is reduced or even flipped. d. In the equilibrium the transverse components of the individual magnetic moments are evenly distributed in all directions of the x-y-plane. The RF pulse enacts a resonant force on the magnetic moments which increasingly resonate with a common phase. As a result, a net transverse macroscopic magnetization arises. Adapted from (32).

The measurement of the MR signal is based on induction. Therefore, a change of the magnetic flux density in the area surrounded by a receiving coil is required. The magnetic flux is provided by the macroscopic magnetization vector (37). However, in the current state of equilibrium the magnetization vector and, thus, also the magnetic flux density are static. For this reason, a transverse magnetization component in the x-y-plane perpendicular to the external magnetic field is required (32). Due to the external magnetic field, a torque acts on this transverse component

which will therefore precess around the z-axis in accordance with the underlying magnetic moments:

$$\frac{\mathrm{d}\vec{M}}{\mathrm{d}t} = \gamma\vec{M} \times \vec{B}_0 \,. \qquad 8$$

This precession of the macroscopic magnetization is accessible by a receive coil (17; 35; 32; 19).

To understand how it is possible to rotate the magnetization vector into the transverse plane, it is beneficial to switch to a rotating coordinate system (RCS). For a coordinate system which rotates with angular velocity $\vec{\omega}$ around the external magnetic field (along z-axis) Equation 8 must be modified to

$$\left(\frac{\mathrm{d}\vec{M}}{\mathrm{d}t}\right)_{\mathrm{RCS}} = \gamma\vec{M} \times \vec{B}_{\mathrm{RCS}} = \gamma\vec{M} \times \left(\vec{B}_0 - \frac{\vec{\omega}}{\gamma}\right) \qquad 9$$

with the magnetic field $\vec{B}_{\mathrm{RCS}}$ acting in the RCS (19). For an angular velocity in accordance with the Larmor frequency this magnetic field is reduced to

$$\vec{B}_{\mathrm{RCS}} = \vec{B}_0 - \frac{\vec{\omega}_{\mathrm{L}}}{\gamma} = \frac{\vec{\omega}_{\mathrm{L}}}{\gamma} - \frac{\vec{\omega}_{\mathrm{L}}}{\gamma} = 0 \qquad 10$$

and therefore, no torque is acting on the stationary macroscopic magnetization (19; 17). An additional in the RCS stationary magnetic field $\vec{B}_1$ results in a precession of the magnetization vector around the axis of $\vec{B}_1$ (19; 32). Thereby it is possible, to produce a transverse magnetization component. The so-called flip-angle by which the macroscopic magnetization vector is tilted with respect to the z-axis is determined by the magnetic flux density of $\vec{B}_1$ and its duration (19; 17).

In the initial coordinate system, the supplementary magnetic field is rotating with the Larmor frequency and is for this reason - and due to its limited duration - referred to as RF pulse (32). The fulfillment of the resonance condition is thereby mandatory since the magnetic flux density of $\vec{B}_1$ is outnumbered by that of the static magnetic field $\vec{B}_0$ (19). The importance of the resonance condition becomes also evident when considering the effects of the RF pulse on the level of the magnetic moments. As derived in the previous chapter in Equation 6, the energy difference between the eigenstates amounts to $\hbar\omega_{\mathrm{L}}$. This energy difference must be overcome in order to induce the excitation of a nuclear spin. Since this condition is

exactly fulfilled by the RF pulse with Larmor frequency, transitions between the energy levels as depicted in Figure 1c are induced (19). As a consequence, the number of nuclear spins in the energetically higher state N_+ is increased at the expense of N_-. Thus, the longitudinal magnetization component is reduced and might even be flipped to anti-parallel orientation to the external magnetic field. Nevertheless, this effect is not resulting in the required transverse magnetization component in the x-y-plane. For the creation of the transverse magnetization component a second effect on the level of the magnetic moments is relevant. The RF pulse exerts a resonant force on the single magnetic moments (37). Thus, the precession of the magnetic moments becomes increasingly resonant with more and more of them precessing in phase. While their transverse component was initially distributed in all directions of the x-y-plane evenly, a predominant direction forms during the RF pulse. Finally, the transverse components no more cancel each other but add up and form a transverse magnetization as schematized in Figure 1d (37).

Relaxation and the Bloch Equations

Every thermodynamic system strives for its state of equilibrium. In the case of the spin ensemble and the macroscopic magnetization two effects cause a return to the initial equilibrium state after excitation with an RF pulse, which are summarized under the term relaxation. Both effects concern an interaction which is coupled with an exchange of energy, that allows a nucleus to return to its energetically favorable spin state. In the first scenario, the so-called spin-lattice-relaxation, the surplus of energy is delivered to the environment, whereas in the case of spin-spin-relaxation an exchange between two nuclear spin systems takes place (37; 35). Both relaxation effects are summarized in Figure 2 and their consequences are considered in more detail in the following.

When considering the relaxation process on the macroscopic level of the magnetization vector, two transformations are necessary to restore the initial condition: The transverse component must be diminished while the longitudinal component parallel to the external magnetic field must be restored. The transverse component was established through the increasing coherence of the precession of the magnetic moments (37). Therefore, small deviations in the magnetic field and,

thus, the Larmor frequency result in a decreasing transverse magnetization (35). Furthermore, each transition between the eigenstates is associated with a phase change. For this reason, both previously described interactions (spin-spin-relaxation and spin-lattice-relaxation) result in a dephasing of the spin ensemble. This reduction of the transverse magnetization, the so-called transverse relaxation, is described with the time constant T_2 (35).

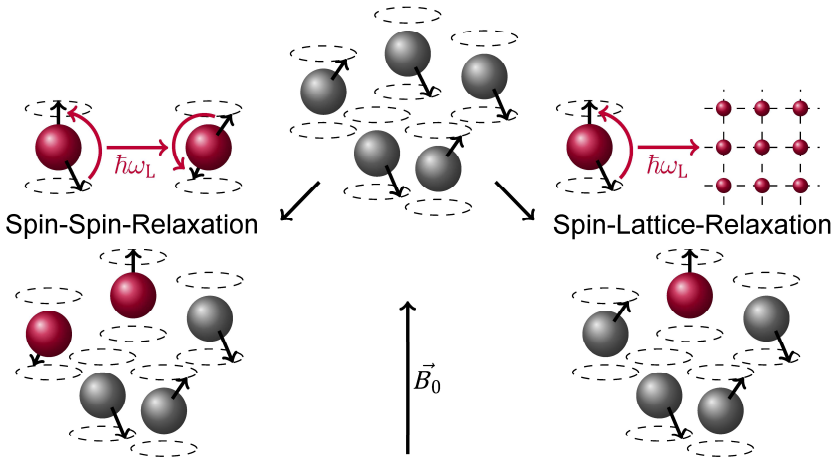

Figure 2. Overview of the two relaxation effects which cause an excited ensemble of spins as depicted in the top to return to its state of thermal equilibrium. In the case of spin-lattice-relaxation (on the right) the energy released during the transition of a nuclear spin is released to the environment. Thus, the initial surplus of spins in the energetically beneficial state is becoming restored and the longitudinal magnetization component builds up again. Furthermore, the coherence of the phase of the spins is lost during the interaction, wherefore the transverse magnetization decreases. While the longitudinal component remains unaffected by the spin-spin-relaxation (on the left) both spins taking part in the exchange of energy lose their phase relation, wherefore this effect further increases the dephasing of the magnetic moments and, thus, the decrease of the transverse magnetization component.

To restore the longitudinal magnetization along the direction of the external magnetic field, it is necessary to recover the initial relation between the eigenstates according to Equation 7. Since the spin-lattice-relaxation is the only process during which energy is released from the spin ensemble and the absolute number of nuclear spins in a certain state is altered, this is the only process that results in a relaxation of the longitudinal magnetization component (37; 35; 19). Given that only the spin-lattice-relaxation contributes to the longitudinal relaxation, this relaxation process is slower. Thus, the longitudinal relaxation time constant T_1 exceeds the transverse relaxation time T_2 for every tissue (37).

Based on the two relaxation processes acting on the macroscopic magnetization vector the differential equations

$$\frac{\mathrm{d}M_x(t)}{\mathrm{d}t} = -\frac{M_x(t)}{T_2} \tag{11}$$

$$\frac{\mathrm{d}M_y(t)}{\mathrm{d}t} = -\frac{M_y(t)}{T_2} \tag{12}$$

$$\frac{\mathrm{d}M_z(t)}{\mathrm{d}t} = -\frac{M_z(t) - M_0}{T_1} \tag{13}$$

with the magnitude of the macroscopic magnetization M_0 in thermal equilibrium along the z-axis can be derived (32). Furthermore, the influence of the external magnetic field according to Equation 8 must be considered and added to the equations (17). Subsequently, to solve the cross product $\vec{B}_0 = B_0\hat{e}_z$ and $\vec{M}(t) = M_x(t)\hat{e}_x + M_y(t)\hat{e}_y + M_z(t)\hat{e}_z$ are inserted and γB_0 is replaced by the Larmor frequency ω_L (35; 19):

$$\frac{\mathrm{d}M_x(t)}{\mathrm{d}t} = \gamma\left(\vec{M}(t) \times \vec{B}_0\right)_x - \frac{M_x(t)}{T_2} = \gamma M_y(t)B_0 - \frac{M_x(t)}{T_2} = \omega_\mathrm{L}M_y(t) - \frac{M_x(t)}{T_2} \tag{14}$$

$$\begin{aligned}\frac{\mathrm{d}M_y(t)}{\mathrm{d}t} &= \gamma\left(\vec{M}(t) \times \vec{B}_0\right)_y - \frac{M_y(t)}{T_2} = -\gamma M_x(t)B_0 - \frac{M_y(t)}{T_2} \\ &= -\omega_\mathrm{L}M_x(t) - \frac{M_y(t)}{T_2}\end{aligned} \tag{15}$$

$$\frac{\mathrm{d}M_z(t)}{\mathrm{d}t} = \gamma\left(\vec{M}(t) \times \vec{B}_0\right)_z - \frac{M_z(t) - M_0}{T_1} = -\frac{M_z(t) - M_0}{T_1} \tag{16}$$

To solve the differential equations a starting condition is set. Therefore, it is assumed, that the entire magnetization is initially flipped towards the x-direction. Thus, the differential equations are solved by

$$M_x(t) = M_0\cos(\omega_\mathrm{L}t)\exp\left(-\frac{t}{T_2}\right) \tag{17}$$

$$M_y(t) = -M_0\sin(\omega_\mathrm{L}t)\exp\left(-\frac{t}{T_2}\right) \tag{18}$$

$$M_z(t) = M_0\left(1 - \exp\left(-\frac{t}{T_1}\right)\right) \tag{19}$$

with the amount of the longitudinal magnetization in thermal equilibrium M_0 and the starting condition $\vec{M}(t=0) = M_0\hat{e}_x$ (35; 19). RF pulses which produce such a starting condition are referred to as 90°-pulses, since they flip the magnetization

vector by 90° (19). The corresponding trajectory of the tip of the magnetization vector is plotted in Figure 3.

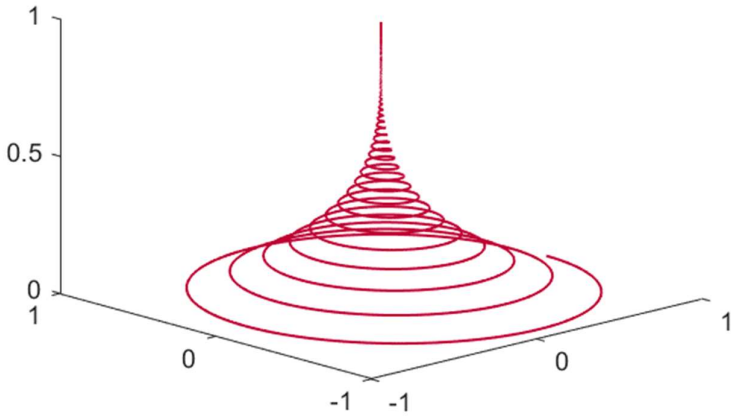

Figure 3. Trajectory of the tip of the macroscopic magnetization during the relaxation process after excitation with a 90°-pulse in the laboratory frame. T_2 was set to one quarter of T_1. Adapted from (35).

The previously described differential equations were first set up and solved by Felix Bloch in 1946 (8) wherefore they are also referred to as the Bloch equations. These equations predict that the magnetization vector performs a spiraling precession around an external magnetic field while the transverse component diminishes exponentially with time constant T_2 and the initial longitudinal magnetization is reestablished with time constant T_1 (35; 19).

Chemical Shift

The previous equations assume an exponential behavior for both, the transverse, and the longitudinal magnetization component. However, this is only the case for a common resonance frequency. This requirement is fulfilled since only magnetic moments from a single spin ensemble are considered which by condition possess the same characteristics and restrictions. This already indicates that this is not the case for the entirety of nuclear spins in a tissue sample. The Larmor frequency of the magnetic moment of a certain atomic nucleus is directly coupled to the magnetic flux density by the gyromagnetic ratio. Previously, this magnetic flux density was attributed to an externally applied magnetic field. Nevertheless, not the field strength of this applied field is relevant for the Larmor frequency but the field experienced at the location of the nucleus. Therefore, two influencing factors must

be accounted for (the second one, the bulk susceptibility shift, is considered in the next chapter). First, the direct chemical environment of the nucleus is considered which causes a frequency shift which is characteristic for the respective environment, the so-called chemical shift. This shift is caused by the electrons in the direct environment of the respective nucleus. Due to their charge and the external magnetic field, these electrons experience a Lorentz force which causes a certain movement (34). In the case of electrons in the s orbital or the spherical p orbitals this movement induces a magnetic field $\vec{B}_e$ which counteracts the external magnetic field $\vec{B}_0$ as depicted in Figure 4 (38).

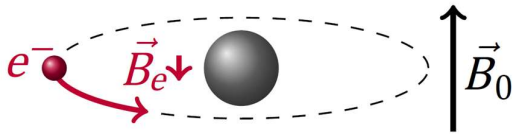

Figure 4. The circulation of the electron in the s orbital or the spherical p orbitals induced by the Lorentz force causes a magnetic field $\vec{B}_e$ counteracting the external magnetic field $\vec{B}_0$ and, thus, exerts a shielding effect at the location of the nucleus.

The Lorentz force is proportional to the external magnetic field wherefore the flux density of the additional magnetic field is also depending on the magnetic flux density of $\vec{B}_0$ (34). In general, the electrons exert a shielding effect which is characterized by the shielding factor σ. Based on this factor the effective magnetic field $\vec{B}_{\mathrm{eff}}$ at the location of the nucleus and, thus, the actual characteristic Larmor frequency

$$\vec{\omega}_{\mathrm{L}} = \gamma\vec{B}_{\mathrm{eff}} = \gamma(1-\sigma)\vec{B}_0 = \gamma\vec{B}_0 - \gamma\sigma\vec{B}_0 \qquad 20$$

can be derived (38; 33). Usually, a reference is chosen, and the chemical shift is given in relation to this reference in parts per million (ppm). The chemical shift is defined as

$$\delta = (\sigma_{\mathrm{ref}} - \sigma)10^6 \qquad 21$$

with a reference with comparatively high shielding factor σ_{ref}. As a consequence, the chemical shift behaves inversely to the strength of the shielding (39). In the case of hydrogen, tetramethylsilane serves as reference. This compound is characterized by the fact that it exhibits only one resonance line at low frequency, wherefore it possesses one of the highest shielding factors in ^{1}H-spectroscopy and

is assigned to a value of 0 ppm (40). For water and methylene, resonance lines at 4.7 ppm and 1.3 ppm result. These values are independent of B_0 and often serve as frequency references in human tissue, where tetramethylsilane is not present.

Susceptibility and Lorentz Sphere

In addition to the chemical shift, the magnetic flux density and, thus, the Larmor frequency is influenced by the magnetic properties of the respective tissue or material:

In the case of magnetic resonance imagers an external magnetizing field $\vec{H}$ is mostly produced by an electric current trapped in a superconducting coil (17). The magnetic field strength thereby depends on the current and the geometry of the coil. This magnetizing field causes a reaction in materials and tissues exposed to it. On the one hand, existing magnetic moments as for example those attributable to the spin of unpaired elementary particles align in a magnetic field, on the other hand, magnetic moments are induced in terms of currents due to Lorentz force (41; 34; 33). Both effects cause the formation of an additional magnetic field in the material which is referred to as magnetization and can be calculated for diamagnetic and paramagnetic, linear materials by multiplying the external magnetizing field with the magnetic susceptibility (41; 33; 35). The magnetic susceptibility χ_m is a dimensionless material specific parameter which is characteristic for the magnetic properties. Depending on the structure of the atoms and their compounds in the respective material, the additional field caused by magnetization can either amplify the external magnetic field as present in paramagnetic and ferromagnetic materials ($\chi_m > 0$) or counteract it ($\chi_m < 0$) (41; 34). The latter is the case for almost all organic tissues, which are therefore so-called diamagnetic materials (33). Figure 5a schematizes the magnetizing field and the resulting magnetization in a diamagnetic material. The magnetic flux density which is relevant for the effects in magnetic resonance tomography results, thus, from the superposition of both these magnetic fields

$$\vec{B} = \mu_0\left(\vec{H} + \chi_m\vec{H}\right) = \mu_0(1 + \chi_m)\vec{H} \qquad 22$$

with the permeability constant μ_0 which amounts to $4\pi \cdot 10^{-7}$ Vs(Am)$^{-1}$ (41; 34; 33). Furthermore, $(1 + \chi_m)$ can be replaced by the material specific relative

permeability μ_r which represents the second dimensionless parameter which characterizes the magnetic properties of a specific material or tissue (41).

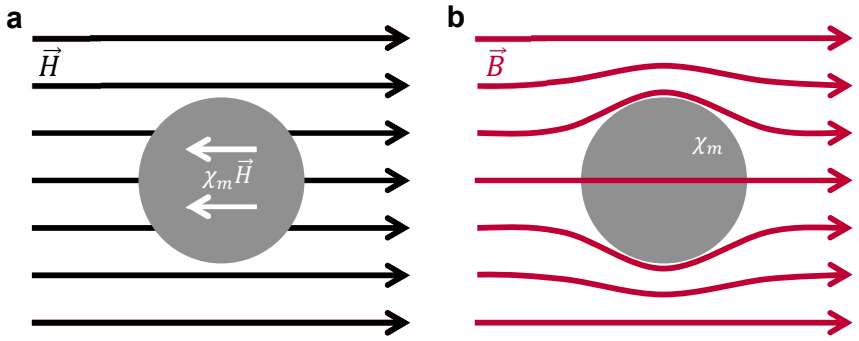

Figure 5. a. Schematic illustration of the magnetizing field $\vec{H}$ and the induced magnetization in a diamagnetic object. b. The magnetic field is partially displaced to the outside by the diamagnetic probe. Thus, a distortion of the magnetic field results which is strongly exaggerated in the illustration. Adapted from (34).

The magnetization is the direct result of the magnetic moments of the tissue under consideration and represents the superposition of these magnetic moments for a restricted volume element. However, the effect of the magnetization is not restricted to the volume of the tissue itself but can also impact the magnetic field of its environment (33). Thus, the magnetic field is pulled inside objects with para- or ferromagnetic characteristics whereas it is distorted to the outside for diamagnetic objects as schematized in Figure 5b (34). As a consequence, magnetic flux density inhomogeneities arise which are characterized by areas with higher magnetic flux density (top and bottom in Figure 5b) and others with lower magnetic flux density (left and right in Figure 5b). These basic considerations are confirmed by the field map in Figure 6 obtained from the analytical model for a diamagnetic sphere (42).

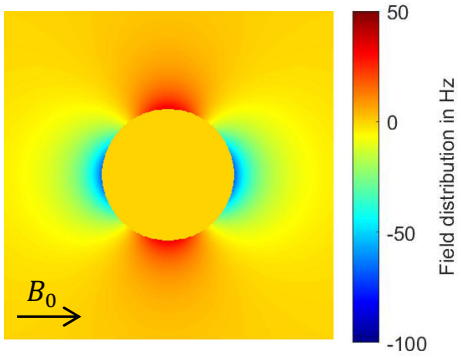

Figure 6. Field map derived from the analytical model of a diamagnetic sphere of relative permeability $-8 \cdot 10^{-7}$ in an external magnetic field B_0 of 3 T. Due to the relation between frequency and magnetic flux density, the field map is displayed in terms of the unit Hertz

In addition to the magnetic properties of the object, the field perturbation is influenced by its shape and volume (33). Thus, based on certain boundary conditions according to the macroscopic Maxwell equations which are defined in more detail in (35), the distribution of the magnetic field $\vec{B}$ inside and outside of continuous compartments with sharp edges can be determined. While these mathematical problems can be solved analytically for certain geometries such as a sphere or a cylinder of infinite length, more complex geometries require a numerical simulation as for example provided by FEM (42). The solution of this basic mathematical problem assumes continuous compartments and provides information on the distribution of the resulting macroscopic magnetic field $\vec{B}_{\mathrm{mac}}$. However, the individual magnetic moments are not representing a continuous magnetization on a microscopic scale wherefore the actual granularity rises the need for an additional correction (35). This so-called Lorentz sphere correction is necessary since the magnetic flux density experienced by the nucleus rather than the macroscopic magnetic field is relevant for magnetic resonance experiments. Therefore, a notional sphere surrounding a spin is considered in which the effective susceptibility partly vanishes due to induced currents. The radius of the sphere is thereby much larger than the intermolecular distance (35). For this reason, the sphere exposes the effects of a locally uniform macroscopic continuum to its environment (43). Furthermore, the effects caused by the adjacent electrons which are considered by the chemical shift and are characteristic for a specific chemical environment are neglected in the following derivation which solely considers the frequency shift referred to as bulk magnetic susceptibility shift (43). The additional field inside the Lorentz sphere $\vec{B}_{\mathrm{lor}}$ represents the difference of the field caused by the considered molecules and the continuous approximation attributable to the magnetization. The molecular fields can be assumed to vanish as verified in (35). From the analytical solution of the magnetization and the deviation of the magnetic field distribution inside a sphere, which can be found in (35),

$$\vec{B}_{\mathrm{lor}} = -\frac{2}{3}\mu_0\vec{M} \qquad 23$$

results for the additional field inside the Lorentz sphere with the macroscopic magnetization $\vec{M}$ of the background derived under the assumption of a continuous

medium. By applying Equation 22 and the correlation between the external magnetizing field and the magnetization,

$$\vec{B}_{\mathrm{lor}} = -\frac{2}{3}\frac{\chi_m}{(1+\chi_m)}\vec{B}_{\mathrm{mac}} \qquad 24$$

can be derived which represents the additional correction to the macroscopic magnetic field to receive the external magnetic field relevant for magnetic resonance:

$$\vec{B}_{\mathrm{ext}} = \left(1 - \frac{2}{3}\frac{\chi_m}{(1+\chi_m)}\right)\vec{B}_{\mathrm{mac}}\,. \qquad 25$$

Thus, the basics for the determination of the external magnetic field distribution for a known geometry and susceptibility are set. Apart from the deviations on the scale of atoms, this distribution and its inhomogeneities are independent of the size scaling of the respective geometry. This allows the characteristics of small structures to be reproduced on a larger scale for phantom measurements to acquire magnetic field maps. However, different size scales impact MR images or spectra differently. On that account, it is important whether the inhomogeneities arise on a scale level below the resolution of the respective acquisition determinants or above (35). Thereby, inhomogeneities below the level of resolution are further divided into micro- and mesoscopic. The former refer to inhomogeneities which arise on the scale level of atomic and molecular structures, whereas the latter designate field inhomogeneities on a larger size scale which nonetheless is still below that of the voxel size (44). Microscopic field inhomogeneities result in a shortening of the transverse relaxation time which is accounted for in gradient echo sequences by the additional relaxation component R_2' (35; 45). However, due to diffusion a shortening of the echo time is also verifiable for spin echo sequences (46). For the acquisition of spectra, field inhomogeneities inside the considered voxel additionally result in a broadening of the spectral lines and, thus, complicate different applications as for example the saturation of selected frequency components (45). Nevertheless, mesoscopic field perturbations can be exploited for functional MRI or to extract information on the tissue structure, whereas the effects of macroscopic field inhomogeneities such as image distortion or echo shifting are undesirable (45; 44; 35). For this reason, shim procedures have been developed to reduce macroscopic inhomogeneities.

MR Sequences and k-Space

The impact of the magnetic field inhomogeneities on the signal behavior also strongly depends on the underlying MR sequence. Thus, a differentiation of gradient echo and spin echo sequences is crucial. As mentioned before, in addition to RF pulses for the excitation of the MR signal, field gradients are mandatory to acquire spatially resolved information. Gradients in MRI denote an additional magnetic field (parallel to the main magnetic field) which linearly increases in magnetic flux density with a certain slope along a specific direction. Therefore, these gradients cause a location dependent resonance frequency (47; 48). Thus, based on the frequency the signal is attributable to a certain location. The reconstruction of the spatial signal distribution from the superimposed frequency components is mostly realized by FT (17). Initially, the induced signal decreases due to the additional dephasing caused by the field gradient. However, this effect is reversible by the application of an inverse field gradient. Spins which were formerly precessing with higher frequency are then exhibiting a reduced Larmor frequency. Therefore, the spins are increasingly regaining their coherence. This effect culminates in the formation of a so-called gradient echo and a detectable signal and builds the basis underlying the acquisition of all MR sequences (49; 47). Nevertheless, dephasing due to field inhomogeneities and therefore signal losses remain. Albeit this additional dephasing is reversible by a second RF pulse which, according to its effect, is referred to as refocusing pulse. This is mostly a 180°-pulse which mirrors the transverse magnetization in the transverse plane. As a result, magnetic moments with lower frequency are ahead in phase and vice versa. If the pulse is applied TE/2 after the excitation a spin echo forms at TE when all magnetic moments are rephased. Gradients which are applied posterior to the refocusing pulse exert the inverse effect, wherefore a gradient echo is produced by the same gradient before and after the refocusing pulse in spin echo sequences. In general, spin echo sequences result in longer TEs, wherefore gradient echo sequences are especially preferred for fast relaxing signal components. However, the latter are sensitive to the additional relaxation component R_2' (35; 45).

Another feature which allows the differentiation of MR sequences is the sampling of the k-space. The k-space stands for the raw data space, in which the acquired MR data is first stored according to a certain pattern and which later is transformed

into an MR image. Thereby, each point represents a complex MR signal recorded at a specific time point (47). Accordingly in addition to the magnitude of the induced signal its phase is recorded. In basic two-dimensional (2D) sequences, a single slice is excited by the excitation pulse. For this purpose, a field gradient is applied during the excitation pulse orthogonal to the desired slice orientation. Therefore, the magnetic flux density linearly increases along one direction, wherefore parallel planes of constant magnetic flux density result. These planes exhibit a unique Larmor frequency which differs from the resonance frequency in other slices. For this reason, the resonance condition of the excitation pulse is only met by the ^{1}H atoms of a particular plane. At this point it is important to consider, that an excitation pulse covers a range of frequencies $\Delta\omega$ which is defined by the so-called excitation bandwidth rather than a single one. As a result, a plane of finite thickness is excited, where the thickness Δz is conditioned by the slope of the slice selection gradient G_{ss}. The correlation between the bandwidth and the slice thickness is described by

$$\Delta z = \frac{\Delta\omega}{\gamma G_{\mathrm{ss}}} \qquad 26$$

and depicted in Figure 7 (36; 35).

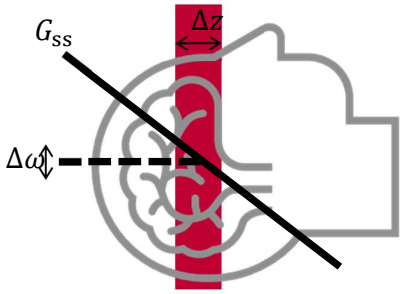

Figure 7. The bandwidth of the excitation pulse $\Delta\omega$ and the slope of the slice selection gradient G_{ss} determine the thickness Δz of the selected slice. Adapted from (36).

Since the MR signal now solely originates from one slice, two dimensions remain which require encoding. The gradient G_{ro} which is present during the readout and responsible for the gradient echo causes an along the so-called frequency encoding direchtion linearly increasing Larmor frequency as depicted in Figure 8. Thus, based on the frequency, conclusions about the location along this direction are possible. The acquired data points during one readout are assigned to one line

in k-space. The central point along this line is usually recorded at the maximum amplitude of the echo.

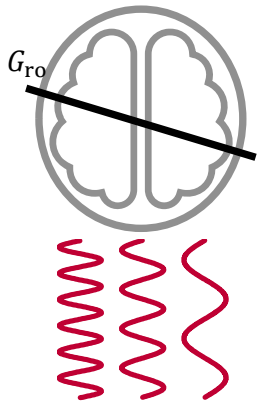

Figure 8. The readout gradient G_{ro} generates a linearly increasing Larmor frequency along the direction in which it is applied. The during one readout acquired data points fill one line in k-space. Adapted from (36).

For spatial encoding in the third dimension, another gradient is necessary which is referred to as phase encoding gradient G_{pe}. This additional gradient is applied between excitation and readout. For its duration, the magnetic moments are precessing with a linearly increasing frequency along the phase encoding direction wherefore a location dependent phase is generated as schematized in Figure 9. Different slopes of the phase encoding gradient encode different lines in k-space. The central line is thereby recorded without phase encoding gradient. Away from the center, an additional phase difference of 360° is generated between the two outermost areas of the phase encoding range from line to line.

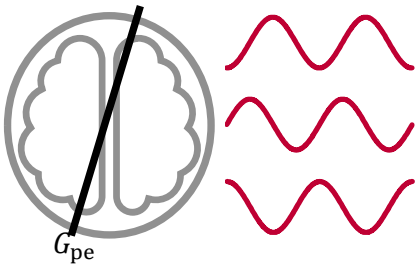

Figure 9. The phase encoding gradient G_{pe} is applied during excitation and readout and generates an along its direction linearly increasing additional phase. Adapted from (36).

The described approach usually samples the k-space line by line either from top to bottom or in the opposite direction in a Cartesian manner which represents the

traditional and most unsophisticated technique (36). Furthermore, the recording time is comparably high without further modifications since every line of every slice is acquired individually. The easiest modification which results in a shortening of the recording time for sequences with long repetition times between subsequent excitations is to acquire data from further slices during this period (47; 17). Thus, additional slices can be recorded without prolonging the acquisition time. This principle can also be exploited to capture images at different echo times. For this purpose, after the initial echo with the minimal echo time further echoes enable the acquisition of k-space lines which are attributable to additional k-space matrices of longer echo times (17). Another opportunity of acceleration is provided by recording multiple lines of the same k-space matrix after a single excitation. Therefore, multiple spin echoes can be created by additional 180°-pulses. Alternatively, multiple gradient echoes with alternating readout gradients are generated after one initial excitation pulse and therefore multiple lines in k-space recorded. These readout gradients are intermitted by a phase encoding gradient of low magnitude, the so-called blip, to move the k-space trajectory to the next line in k-space (17; 35). This technique even allows to fill the entire k-space within one cycle of excitation and readout. However, this sequence results in a comparably high echo time of usually 20-60 ms since the center of k-space is sampled in the middle of the readout train (17). This problem can be addressed by radial or spiral k-space trajectories. These start in the center of k-space as depicted for the latter in Figure 10 (in comparison to the Cartesian sampling), wherefore shorter echo times are achieved since the echo time is defined as the duration between the middle of the excitation pulse and the readout of the k-space center (17; 35).

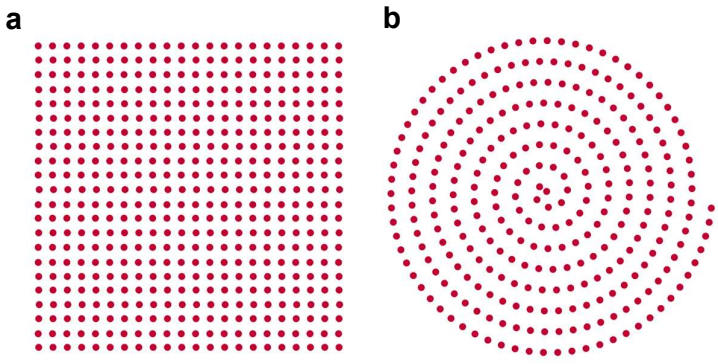

*Figure 10. Comparison of a Cartesian sampled 2D k-space (**a**) and the distribution of the acquired data points for a spiral k-space trajectory (**b**).*

However, this technique is associated with other challenges compared to the Cartesian sampling. First, the spiral trajectory requires varying gradients for both gradient directions in the plane of the spiral. The oscillating gradients exert more stress on the gradient system and, thus, cause heating of the gradient system and the passive shim irons which culminates in magnetic field inhomogeneities (50). Second, to transfer the k-space into images via FT, a continuous raw data set of constant density is necessary. For this reason, prior regridding of k-space and furthermore mostly multiple trajectories are required to achieve a sufficient in-plane resolution which prolongs measurement time (36; 51).

Previously only 2D sequences were considered which acquire multiple slices by subsequent, selective excitation. This excitation limits the minimum slice thickness to approximately 2-4 mm, wherefore isotropic voxel sizes are difficult to obtain (47). Furthermore, slice profile imperfections must be expected (47; 52). To receive isotropic voxel sizes, 3D sequences are advantageous. In 3D sequences a thick slice or even the entire volume of the object of interest is excited at once (17). Differentiation of multiple slices is then achieved by additional phase encoding in the third direction which is also referred to as partition encoding (35). Therefore, gaps between the slices or different orientations thereof are avoided, and the resulting raw data fills a 3D k-space (47; 17). Image data is reconstructed via a 3D FT, wherefore in the case of an isotropic voxel size a subsequent change of the image plane is feasible (17).

Many tissues in the human body possess fast relaxing components and are, thus, not accessible with standard MRI sequences. However, by combining the previously mentioned techniques, it is possible to shorten the echo time by a factor of approximately 10 to 20 and, thus, create a sequence which is sensitive to fast relaxing signal components (53). Since the echo time is defined as the duration between excitation and readout of the central data points in k-space the most important modification for acceleration is to choose k-space trajectories which start in the center of k-space (17; 35). Further acceleration is generated by omitting preparation gradients previous to the readout. These are for example necessary to rephase the dephasing caused by the slice-selection gradient or for non-center-out k-space trajectories. Thus, shorter echo times also result for non-selective excitation pulses accompanied by additional phase encoding in the third dimension

since at least for the central slice in the 3D k-space no gradients between excitation and readout are required (51). Combining spiral sampling and phase encoding in slice encoding direction results in a sampling of k-space by a stack of spiral trajectories as schematized in Figure 11 (51).

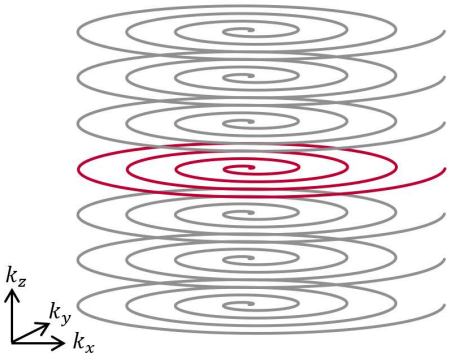

Figure 11. Schematic illustration of a 3D k-space sampled by a stack of spiral trajectories. The central slice (red) is thereby sampled without rephasing gradients between excitation and readout. This technique of k-space sampling is described in more detail in (51).

If multiple echo times are required, acceleration of the total measurement time can be generated by recording multiple echoes with different echo times after one excitation. The sequence described by the sequence plot depicted in Figure 12 acquires six equidistant echoes (TE_1 – TE_6) after an initial excitation with a rectangular pulse. Rectangular pulses are attributed to the hard pulses, which allow immediate data sampling and exhibit the shortest duration for a certain flip angle (51).

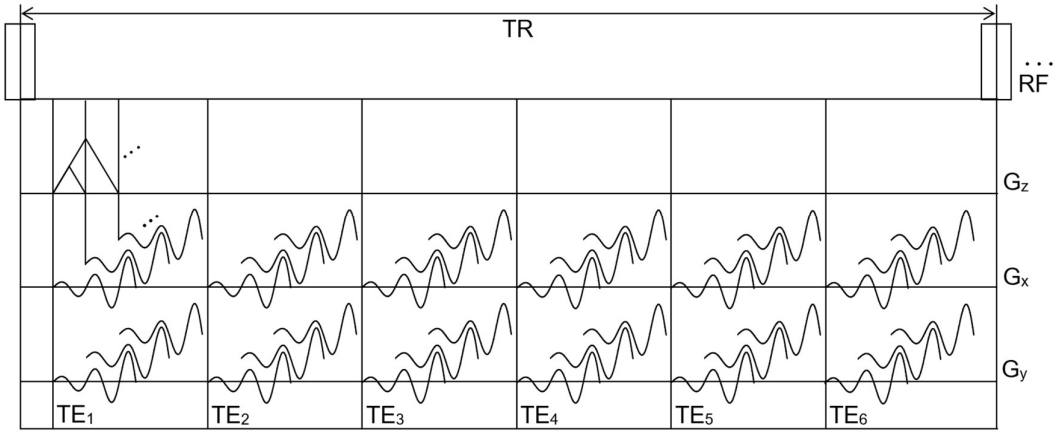

Figure 12. Sequence plot of a so-called UTE sequence which acquires 3D k-space with a stack of spiral trajectories. After an initial excitation with a rectangular RF pulse six equidistant echoes are acquired. To obtain a sufficient in-plane resolution multiple spiral trajectories are required.

Due to its ultra-short echo time of approximately 0.008 to 0.5 ms the previously described sequence is referred to as UTE and accesses structures with transverse relaxation times of down to 0.001 to 0.1 ms (53; 54). Based on a prototypical 3D stack of spiral trajectories UTE sequence, a method was developed in Part II which allows to calculate spatially selective spectra with minimal echo time.

2. Part I: Towards detection of inflammation in adipose tissue: Microscopic field simulations to estimate water signal properties

Anja Fischer[1], Fritz Schick[1]

[1] Section on Experimental Radiology, University of Tübingen, Germany

published in

Zeitschrift für Medizinische Physik 2021, 31(4): 394-402 (55)

Abstract

Inflammation of adipose tissue, particularly visceral adipose tissue, is assumed to be a causal factor for the development of type 2 diabetes, non-alcoholic fatty liver disease, and cardiovascular diseases. Invasive biopsy is currently mandatory for assessment and grading of adipose tissue inflammation. Magnetic resonance detection of the increased water content of inflamed adipose tissue is considered to be a non-invasive alternative. Additional water is mainly originating from macrophages clustering in small regions between adipocytes. This article addresses the characteristics of water signals from areas between adipocytes in terms of line width, line shape, and relaxation properties. Since water and lipids inside adipose tissue have different magnetic susceptibilities, microscopic field inhomogeneities arise depending on the geometry and orientation of the water containing confinements. Relatively pronounced microscopic field inhomogeneities in the water compartments cause a broad spectral distribution of water signals. As a consequence, the water signal of adipose tissue shows special characteristics different to common parenchyma tissues, in which cell content and intercellular space consist of water. The broad and non-Lorentzian field distribution of signals emanating from the water compartments in adipose tissue results in a fast non-exponential signal decay. Therefore, short echo times are recommended for sensitive gradient echo based imaging. A non-exponential irregular signal decay potentially leads to problems in fat/water separation using Dixon techniques. Marked microscopic field inhomogeneities in combination with diffusion related displacement of water molecules cause irreversible dephasing and therefore accelerated signal decay even for spin echo sequences. A volume localized spectrum of porcine fat recorded at 3 T by a STEAM sequence with an echo time of 5.4 ms shows a broad water signal with a line width of 70 Hz ± 4 Hz, in contrast to the CH_2-peak of lipids in the same spectrum with a line width of only 14.7 Hz ± 0.7 Hz. This finding is qualitatively consistent with the results of FEM (finite element modeling) of the magnetic field in geometric models and experiments in phantoms with oil filled balloons surrounded by water

Keywords: Magnetic Resonance Imaging, Susceptibility variations, Field map estimation, Obesity, Inflammation, Adipose tissue

Introduction

According to the World Health Organization the number of overweight subjects increased constantly during the past two decades (56). Obesity is a well-known risk factor for several serious widespread diseases. Current studies on the relationship between obesity and these diseases indicate that inflammation of adipose tissue, in particular visceral adipose tissue, is an important trigger for the development of type 2 diabetes (57), non-alcoholic fatty liver disease (58), atherosclerosis (59) and cardiovascular disease (60). Although assessment of inflammatory changes in adipose tissue is of great interest for early detection and prevention of these diseases, no reliable non-invasive diagnostic method is currently available. Examination of fatty tissue inflammation requires invasive tissue biopsy and subsequent histological analysis. Results are only valid for a small tissue area and not necessarily representative for the entire inflammation status. Availability of a non-invasive technique as MRI for detection of an increased amount of water in inflamed fatty tissue would be highly desirable. Inflammation of adipose tissue is closely linked to a gain in fat mass due to overnutrition. As shown by Spalding et al. (61) the mass gain in obese adults is based on increasing adipose cell volume while adipose cell number stays unchanged. The enlargement of adipocytes leads to poorer oxygenation which in turn causes oxidative stress and a proinflammatory response of adipose tissue (62). An increasing number of proinflammatory macrophages migrate into the adipose tissue and form characteristic aggregates (63). Figure 13 illustrates those water containing aggregates and compares histological findings in normal (a) and inflamed (b) adipose tissue (64). Cinti et al. (65) reported that more than 90% of all macrophages in obese individuals accumulate around dead adipocytes the number of which correlates positively with adipocyte size. The same group discovered that these aggregates of hydrous cells (so-called crown-like structures) are more widespread in visceral adipose tissue (even though adipocytes are known to be smaller there) compared to subcutaneous adipose tissue in humans (66). Clustering of macrophages between much larger adipocytes forms more or less characteristic geometries of water-rich confinements (WRC) in adipose tissue as shown in Figure 13b. The different magnetic susceptibilities of water and fat lead to distinct microscopic inhomogeneities of the magnetic field. These field inhomogeneities and potential

water diffusion inside the WRC may affect the sensitivity of various MR sequence types to the water signal fraction of adipose tissue. The main goal of this study is to assess the properties of water signals originating from WRC in terms of frequency distribution and relaxation characteristics. Simulations and phantom measurements were performed to estimate the properties of the water signal and their influence on the detectability of water by common spectroscopy and imaging sequences.

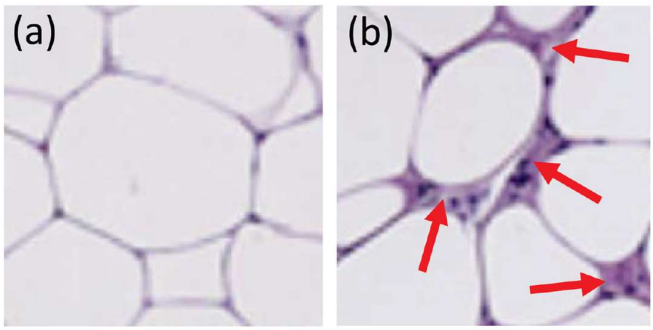

Figure 13. Details of histological findings according to Park et al. (64) of normal (a) and inflamed (b) adipose tissue. The "crown-like" water containing structures in-between the white adipocytes are indicated by red arrows.

Methods

Simulations and phantom measurements were conducted to estimate the field distribution within WRC between adipocytes. Resulting data provided a basis for the following calculation of the signal decay after RF excitation. The simulations were compared to spectroscopic examinations of porcine fat *in vitro*.

Simulations of field distributions in water cones

FEM (Finite element modeling) of the static magnetic field distributions was carried out using a conjugate gradient solver implemented in COMSOL Multiphysics® 4.3b. Results were further evaluated by MATLAB® R2020a for simulation of the signal decay. WRC are 3D objects characterized by sharp edges, curved surfaces and spikes. The simplest geometry that combines these three features is a cone. Therefore, water cones (χ_m = −9 · 10^{-6}) (67) with different ratios between height and radius (RHR = 0.2, 0.5, 1, 2) in a fat environment (χ_m = −8.2 · 10^{-6}) (68) were chosen to mimic WRC in a simplified way. Furthermore, changes of the cone orientation with respect to the static magnetic field (0°, 15°, 35°, 45°, 55°, 75°, 90°)

were studied. Consideration of angles between 0° and 90° was sufficient, since larger angles up to 180° show symmetric behavior. An angle of 55° (so-called magic angle) was studied because this angle is known to result in the smallest field distribution for elongated objects. The mesh of finite elements was set extra fine for the area of the cone (~100 000 elements) and its direct environment, while a coarse mesh was found sufficient for the surroundings of the object of interest (spherical shell). This results in a total of approximately 200 000 elements in the simulations. The COMSOL simulations were based on Maxwell's equations and allowed to assess the macroscopic field distribution $\vec{B}_{\mathrm{mac}}$ based on bulk magnetic susceptibility shifts. To obtain the external magnetic field $\vec{B}_{\mathrm{ext}}$ which is relevant for magnetic resonance, a Lorentz sphere correction is required. According to Durrant et al. (43) this correction can be estimated by

$$\vec{B}_{\mathrm{ext}} = \left(1 - \frac{2}{3}\frac{\chi_m}{(1+\chi_m)}\right)\vec{B}_{\mathrm{mac}} \qquad 27$$

with the magnetic susceptibility χ_m of the material. Since only relative differences in susceptibility are relevant for the generation of microscopic field inhomogeneities the difference in susceptibility between fat and water ($\chi_m = -8 \cdot 10^{-7}$) was applied for simulation of the magnetic field inside the cones. For calculation of the signal decay of a cone the single spatial elements representing the cone were first treated individually. Complex signal contributions from all spatial elements within the cone were added up in order to simulate the signal decay of the entire cone.

Phantom measurements

Phantom measurements were performed with a model geometrically representing fatty tissue with an approximately 1 000-fold magnification. Since the field distribution is independent of scaling for a given geometric arrangement of susceptibilities, this allows assessment of the field distribution with a relatively high spatial resolution. Eight balloons were filled with 100 ml rape oil, placed in a plastic box and surrounded by distilled water. This phantom was placed in the scanning room 20 h before the measurement to adapt to room temperature (22.5°C). A multi gradient echo sequence was applied on a 3T whole-body MR unit (Siemens MAGNETOM Prisma). A Head/Neck-Coil with 20 channels served for signal acquisition. Two different echo times (2.46 ms and 4.92 ms) were recorded for

measuring the static magnetic field distribution. The background field was subtracted deploying a third grade 2D weighted polynomial fit. Magnitude images allowed clear differentiation between the balloons and water containing regions and were therefore applied for spatial segmentation of the latter compartments. Signal frequencies of all spatial subregions in the water compartments of the phantom were derived from the measured magnetic field distribution, and the temporal course of the overall signal of water situated in the regions between oil balloons was calculated.

Spectroscopy of porcine adipose tissue *in vitro*

Porcine adipose tissue has a similar structure to human adipose tissue, and it is easily accessible. Therefore, it was chosen as an *in vitro* sample for measuring water signal characteristics. It should be noted that, unlike in humans, Faris et al. (69) found the highest macrophage number in pigs in subcutaneous adipose tissue. A STEAM sequence for localized ^{1}H spectroscopy was applied with eleven echo times ranging from TE_1 = 5.4 ms to TE_{11} = 25 ms. The porcine fat was warmed up to a temperature of 40°C in order to get the fat in a liquid state and to better approximate the situation *in vivo*. Line width of the water signal was assessed and compared to the field distributions resulting from the FEM simulations of cones and the oil balloon phantom. In addition, spectra of lard (porcine fat with very low water content) were recorded using the same sequence and measurement parameters. This allowed better insight in the signal contributions from glycerin and water which tend to overlap.

Results

Magnetic field distributions resulting from the FEM simulations of cones, from measurements of the oil balloon phantom, and from spectroscopy of porcine fat were analyzed and compared.

Simulations of field distributions in water cones

Examples of field maps of cones positioned in a static magnetic field of 3 T are shown in Figure 14 for four different orientations (0°, 35°, 55°, 90°) to the static magnetic field and four different RHRs. The color maps in the figure show a slice through the cone axis. Both, orientation and shape of the cones clearly influence

the field distribution and the main direction of the field gradient inside the cones. The field distributions of the entire volume of the cones were calculated for all combinations of cone orientations to the static magnetic field and RHRs. Images of slices through the cone axes are displayed in Figure 15. Field inhomogeneities are given as Larmor frequency deviations in this figure. The partly highly asymmetrical shapes of resulting distributions of water frequencies should be noted. For further evaluation, histograms with a bin width of 1 Hz of the field distributions inside the cones were evaluated and exploited to determine the full width at half maximum (FWHM).

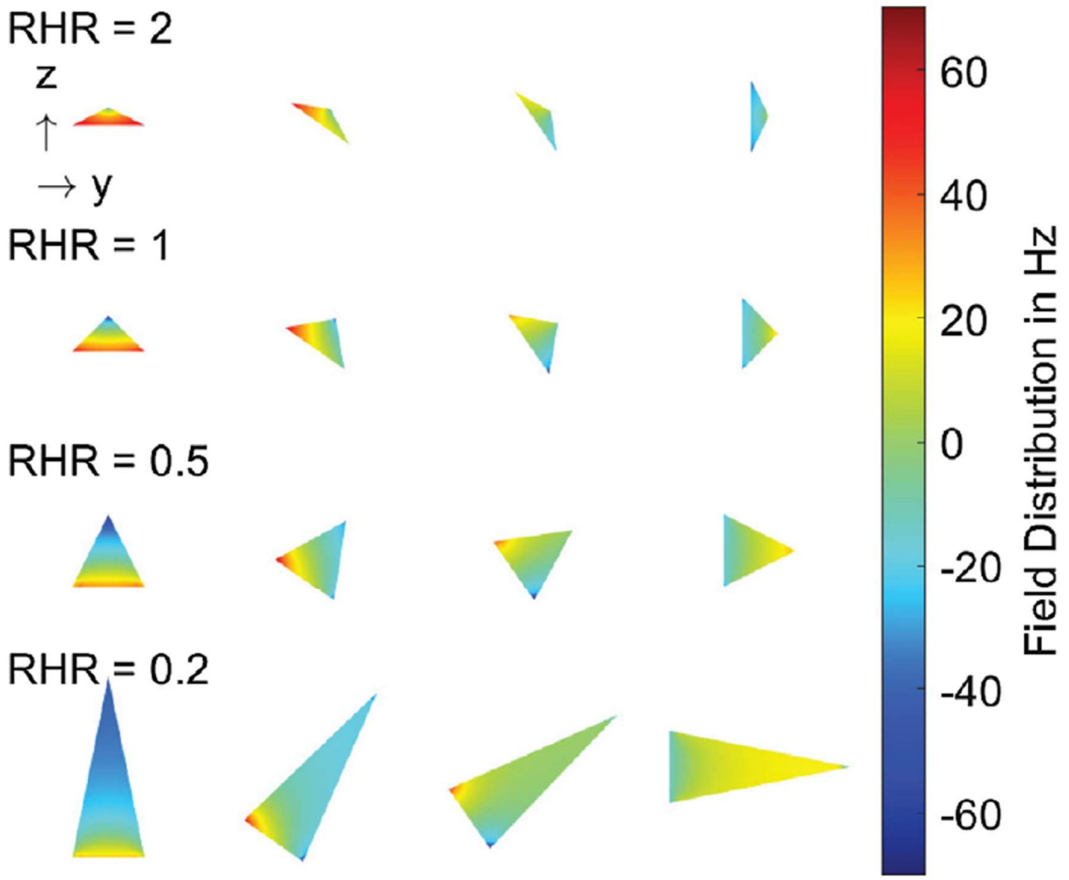

Figure 14. Simulated field maps in Hertz from water filled cones surrounded by fat in a z-y-plane through the cone axis for different RHRs and orientations towards a static magnetic field with a magnetic flux density of 3 T along z-direction.

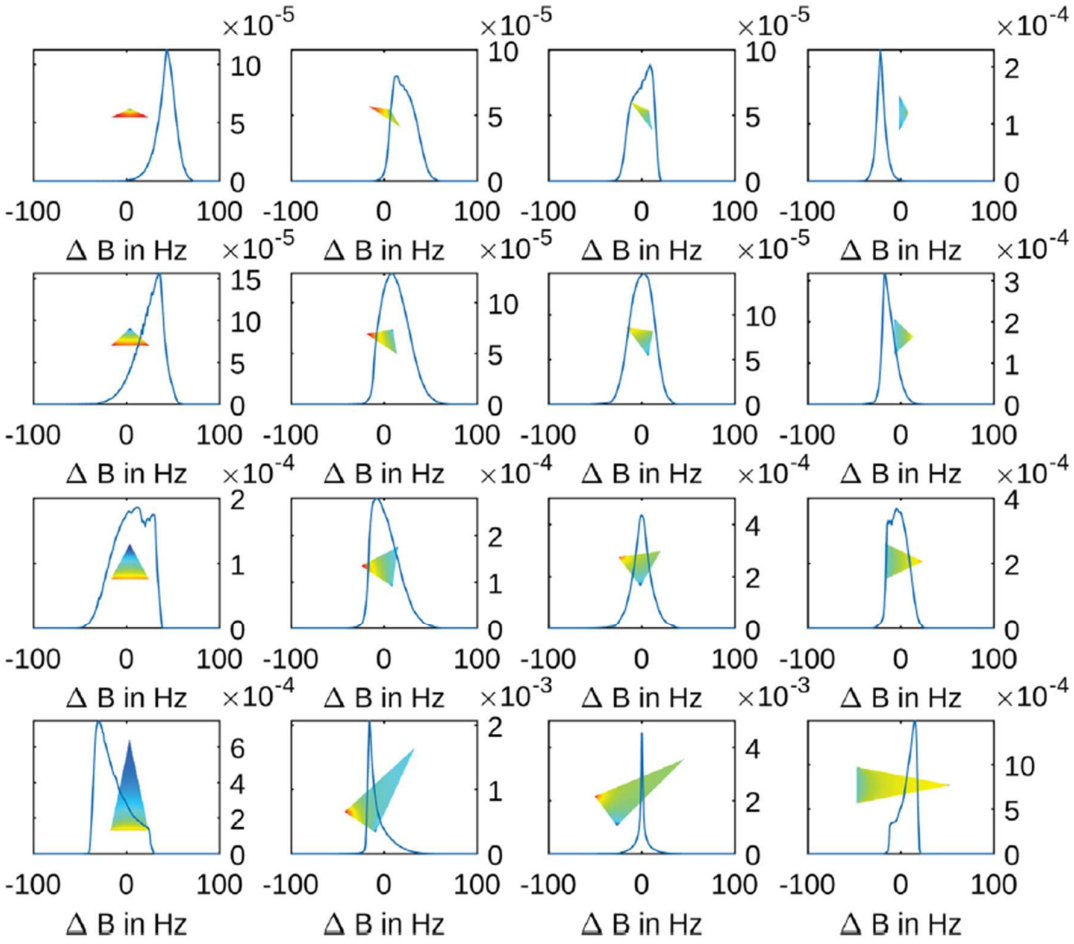

Figure 15. Normalized field distributions for four different RHRs from top to bottom (2, 1, 0.2, 0.5) and four different orientations of the cone axis towards the main magnetic field from left to right (0°, 35°, 55°, 90°). The distributions are plotted against the field deviation ΔB in Hertz. The corresponding field maps are depicted in the background of each plot.

Figure 16a shows the FWHM values plotted against the angle of the cone axis for all four RHR shape parameters. As expected, the lowest FWHM value results from the combination of 55° and the most elongated cones (RHR = 0.2). Flat cones (RHR = 1 and RHR = 2) show the lowest FWHM for an orientation of the cone axis perpendicular to the static magnetic field. Elongated cones lead to the largest FWHM for an orientation parallel to the magnetic field, whereas the flat cones maximize FWHM for 45° between cone axis and static magnetic field. The dependence on the orientation is therefore strongly related to the RHR and shows an opposite behavior when comparing oblong and flat cones. Figure 16b presents the dependence of the mean value of ΔB on the orientation of the cone axis to the static magnetic field for different RHR values. For the two flat cones with RHR of 1

and 2 a growing angle to the static magnetic field results in a decreasing ΔB, whereas the opposite behavior is shown for RHR = 0.2. ΔB values with RHR = 0.5 were relatively low and stable for different orientations to the outer magnetic field. ΔB curves for cones with different shape (RHR values) are crossing at an angle of 55° between cone axis and static magnetic field. The largest difference in ΔB values (and therefore in mean Larmor frequencies) between cones with different RHR occurs for the case with cone axes oriented parallel to static magnetic field. The courses of signal decay of the entire cones with different RHR values are depicted in Figure 16c.

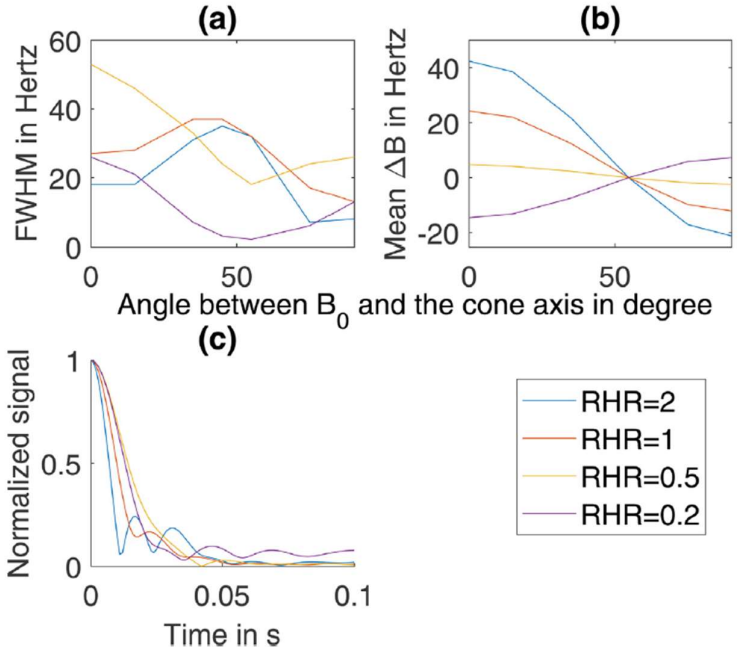

Figure 16. FWHM (a) and mean (b) of the simulated field maps inside water filled cones surrounded by fat depending on the orientation in a static magnetic field of 3 T and normalized signal decay over time (c) calculated from the field maps obtained with seven different unweighted orientations towards the main magnetic field for four different RHRs.

Complex signal contributions of the seven different orientations were summed up for formation of the total signal magnitude. Total signal magnitudes were normalized to a value of 1 at the starting time. None of signal decay curves shows a mono-exponential characteristics which would be necessary to calculate a reliable relaxation time T_2^* for the cones with different RHR. Nevertheless, the signal intensities were fitted to a mono-exponential function in order to obtain a rough estimation of the signal decay time (according to T_2^*) in gradient echo

measurements. Consistent with the signal curves, cones with RHR = 0.5 provided the longest signal decay time (17.1 ms ± 1.0 ms). The shortest signal decay time of 10.1 ms ± 1.0 ms resulted for the flattest cone (RHR = 2). The other cone shapes (RHR of 1 and 0.2) led to decay times of 12.7 ms ± 0.8 ms and 15.8 ms ± 1.3 ms, respectively. For estimation of the line width and shape of water signals, the field distributions from cones with four different RHRs at seven different orientations were added. The field distributions originating from the different RHRs were normalized prior to summation. The result of the summation is depicted in Figure 17 along with a fitted Gaussian curve. The fitted Gaussian distribution shows an FWHM of 42.1 Hz ± 1.3 Hz.

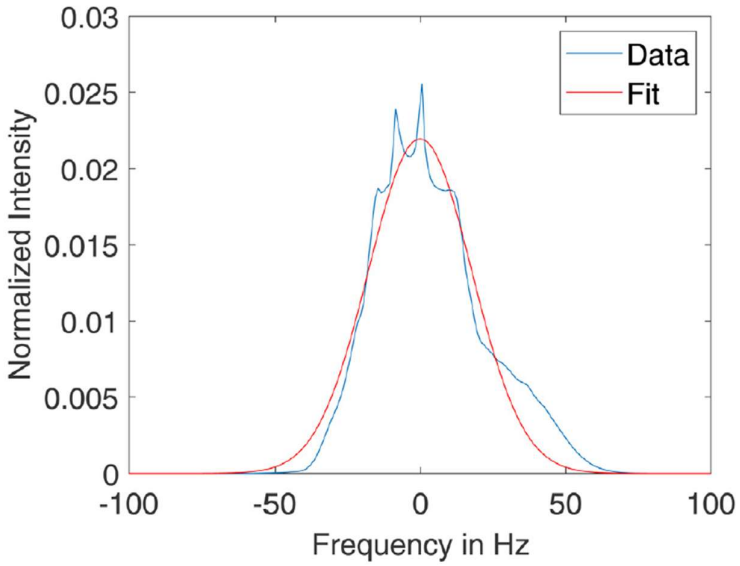

Figure 17. Field distribution obtained from simulated field maps within water filled cones surrounded by fat using seven different orientations of the cone axis towards the static magnetic field (3 T) and four RHRs. Furthermore, the fitted Gaussian distribution is depicted.

Phantom measurements

The oil balloon phantom was examined for visualization of magnetic field inhomogeneities in the water compartments surrounding the balloons. The measured field distribution, the 2D polynomial fit applied for correction of extended field gradients in the background, and the resulting corrected field distribution are depicted in Figure 18. Only water filled regions between the oil balloons are of interest for estimating the water signal decay. Magnitude gradient echo images (not

shown in the figure) were utilized for segmentation of the picture elements representing water area in the 3D image data set.

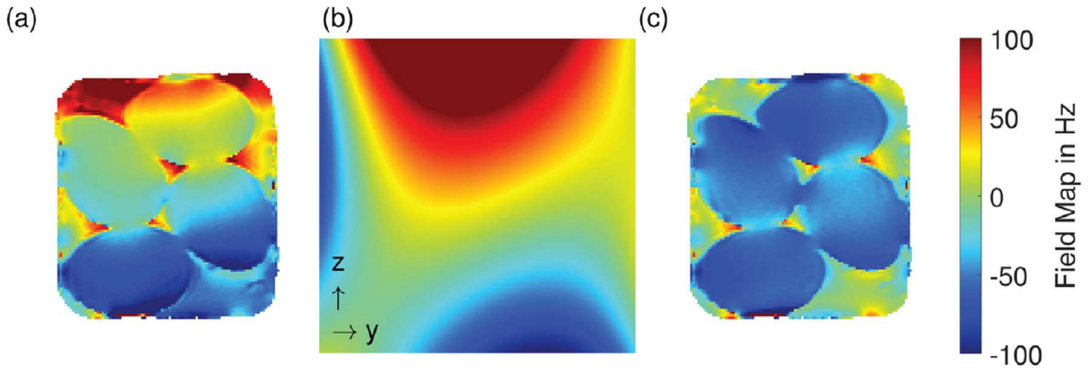

Figure 18. The field distribution of a phantom consisting of oil filled balloons surrounded by distilled water in (a) shows an impact of the background field, which was corrected using the 2D polynomial fit (b) to obtain the corrected field distribution (c). All images show the deviation in Hertz.

Four B_0-maps of water regions in slices with different orientations and positions are depicted in Figure 19.

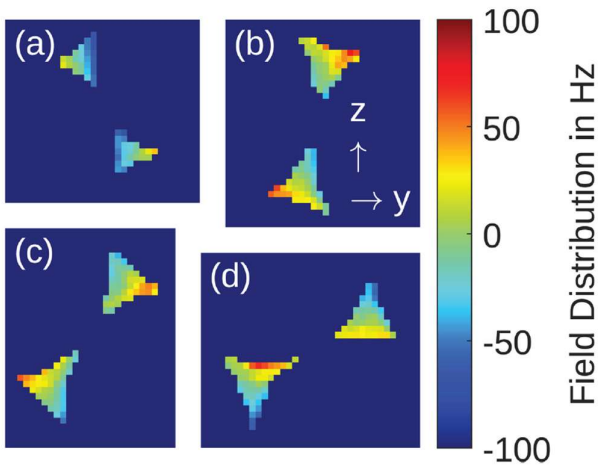

Figure 19. Field maps resulting of the water inclusions obtained from four phantom measurements ((a) slice 1, (b) slice 2, (c) slice 2 clockwise rotated by 30°, (d) slice 2 clockwise rotated by 50°). Only the deviation in Hertz within the water compartments is depicted.

These four B_0-maps were analyzed: An overarching field distribution shown in Figure 20 was calculated by summing up the normalized frequency distributions of the four areas with a bin width of 5 Hz. The FWHM of the overarching distribution was measured for a fitted Gaussian distribution which is also depicted in the figure. The FWHM of the Gaussian distribution amounts to 60 Hz ± 7 Hz which is

somewhat higher than in the field distribution simulations with the cones. The overarching field map of the hydrous areas in the balloon phantom was taken as the basis for computing the signal decay (calculated as superposition of all signal components with different frequencies). This behavior must be expected for fatty tissue, since many water containing areas occur within one picture element.

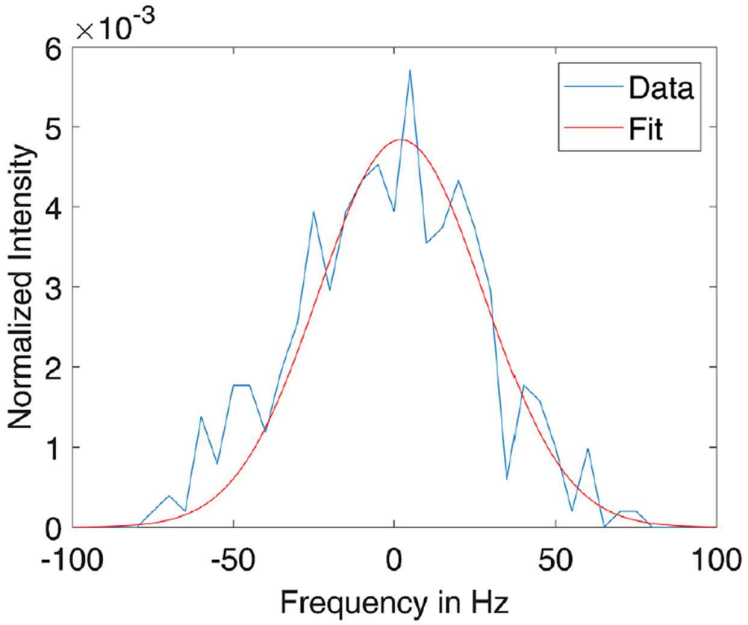

Figure 20. Field distribution within water compartments enclosed by fat balloons from combination of four different measurements and corresponding fit based on a Gaussian distribution.

Figure 21 depicts the resulting signal development. As practiced for the signal development in the simulations of the cones, the signal decay time was estimated by fitting to a mono-exponential function. This method results in a signal decay time of 8.3 ms ± 0.9 ms. In a static regime, signal dephasing effects caused by field inhomogeneities have no influence on the signal yield when using spin echo based sequences. But small water molecules show high apparent diffusion coefficients and are expected to rapidly change their position inside the small water compartments between adipose cells. Thus, an accelerated signal decay must be considered even for spin echo sequences, since rephasing of transverse magnetization is disturbed by rapid displacements of molecules in a microscopically inhomogeneous magnetic field. We can assume a typical extension of a water compartment of approximately 50 µm and a maximum field gradient of approximately $\Delta B = 1.7\ \text{Hz}\ \mu\text{m}^{-1}$. According to Schenck (67) the

apparent diffusion coefficient (ADC) value of water in parenchyma tissue is approximately $D = 1.2 \cdot 10^{-5}$ cm^2 s^{-1}. For estimation of potential effects of water diffusion in the inhomogeneous field simplified calculations of the signal reduction along one dimension were performed for single spin echo experiments. It turned out that for echo times less than 10 ms signal reduction is less than 1% and therefore negligible. In contrast, for TE = 50 ms a signal reduction of up to 66% occurs. Short echo times are therefore preferable for both, spin echo and gradient echo sequences.

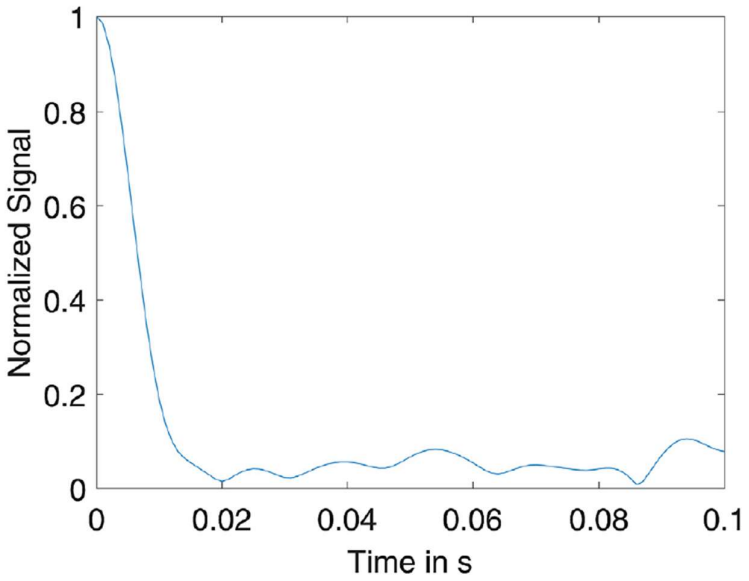

Figure 21. Signal decay resulting from the field distribution within water compartments enclosed by fat balloons using the field maps obtained from four different measurements.

Spectroscopy of porcine adipose tissue *in vitro*

A ^{1}H spectrum of porcine adipose tissue was recorded using a STEAM sequence with TE = 5.4 ms. The spectrum presented in Figure 22 shows a broad signal at approximately 4.5 ppm. Compared to the CH_2 line of fat (methylene protons of the fatty acids) at 1.3 ppm with FWHM = 14.7 Hz ± 0.7 Hz) the fitted line at 4.5 ppm appears clearly broader. A Gaussian line with FWHM = 87 Hz ± 5 Hz was fitted to the signal as depicted in the cutout of the figure. Comparable spectra from lard showed that the broad fitted line in the spectrum in Figure 22 stems from water and from protons of the glycerin backbone of triglycerides (the main type of lipids in the fat vacuoles of adipocytes): A spectrum from lard was recorded showing very similar composition as unprocessed porcine fat tissue, but nearly lacking water

content. By subtraction of the lard spectrum from the spectrum of unprocessed porcine fat the main portion of the broad signal remains and shows a FWHM of 70 Hz ± 4 Hz. This procedure was repeated for ten further echo times (7 ms, 9 ms,11 ms, 13 ms, 15 ms, 17 ms, 19 ms, 21 ms, 23 ms and 25 ms). Mono-exponential fitting of the areas under the fitted Gaussian distributions lead to a relaxation time of the water signal of T_2 = 14.7 ms ± 1.1 ms.

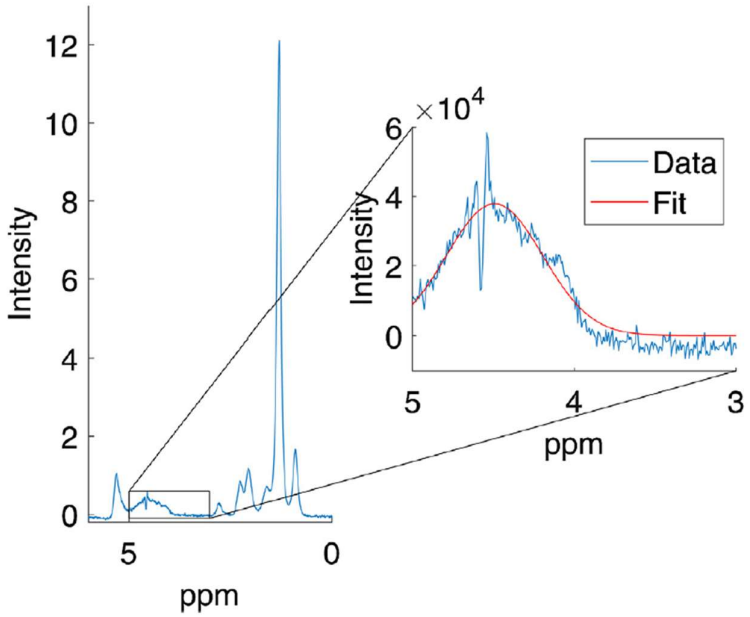

Figure 22. Spectrum obtained from porcine fat using a STEAM sequence with TE = 5.4 ms. A broad peak occurs at 4.5 ppm and is fitted using a Gaussian distribution as depicted in the zoomed cutout.

T_2^* estimation

Spectroscopic examinations of porcine adipose tissue (and lard) led to a T_2 value of 14.7 ms ± 1.1 ms. T_2' values of water in adipose tissue from the finite elements simulations of cones ranged from 10.1 ms ± 1.0 ms to 17.1 ms ± 1.0 ms, dependent on the shape parameter RHR. A T_2' value of 8.3 ms ± 0.9 ms was derived from the phantom measurements with the oil filled balloons. All simulations and experiments were based on conditions present at 3 T. Combining these relaxation times a T_2^* between 5 ms and 8 ms results.

Discussion

The simulations and phantom measurements revealed that water signals of adipose tissue tend to show a relatively broad frequency distribution (with FWHM

up to 70 Hz at 3 T). The width and shape of water lines must be expected to be much broader and more irregular than the lines of lipid signals from the same specimen. In addition, strong microscopic field gradients inside the WRC can lead to rapid signal dephasing caused by diffusion of the small water molecules which is not compensated by spin echo techniques with moderate echo times. The results presented here are more qualitative than quantitative because assumptions made for the simulations and phantom measurements do not exactly meet the conditions in real human adipose tissue. One limitation of this study is the use of porcine subcutaneous adipose tissue with unknown state of inflammation. According to Vieira-Potter et al. (70) no inflammatory markers are detectable in adipose tissue of obese pigs compared to lean controls. In particular, the number of macrophages in subcutaneous adipose tissue was shown to be similar for both types of pigs. Faris et al. (69) reported no diet induced changes in adipose tissue of pigs. When comparing omental, visceral and subcutaneous adipose porcine tissue the highest content of macrophages was found in subcutaneous tissue. As a consequence, WRC in the porcine fat tissue sample presented in this work are probably not related to an inflammatory status of the pig. The features of adipose tissue in swine do not apply to humans who show high numbers of macrophages in inflamed visceral adipose tissue, but not in subcutaneous compartments. Possible influences of blood perfusion on the measured water signals are neglected in the present study. *In vivo* studies in inflamed adipose tissue are necessary for better insight into this issue. The geometry of WRC was mimicked by water filled cones with different RHRs and different orientations to the static magnetic field. A uniform water-like behavior of the content of the cones was assumed, and the susceptibility difference to the surroundings corresponded to that between fat and water. Additional effects should be considered under *in vivo* conditions: For example, iron uptake in macrophages could lead to even more pronounced magnetic field disturbances and faster decay of the water signal. The choice of different cone geometries and orientations does also not exactly meet the situation in reality, where WRC take quite different shapes. Due to the diversity of WRC, a single geometrical form (even with variations) cannot be fully representative of the entirety of all WRC. For the simulations it was necessary to choose a geometry that unifies the most important characteristics of the WRC which are sharp edges, curved surfaces and spikes. The cones combine these characteristics in a simple and

reproducible manner. Effects of the orientation of the WRC to the outer magnetic field and shape dependent effects were simulated by calculations with seven different orientations from 0° to 90° and four different RHR values. Nevertheless, the discontinuity of orientation and shape parameters led to some peak structures in the calculated field distributions which must be attributed to individual cones. Smoothing of the field distribution would be expected if additional angles and RHRs were added to the simulation. However, the chosen combinations at least allow for a qualitative estimation of the line width, line shape and effects in measurements with variable echo time. The phantom with the oil filled balloons surrounded by water was applied for field mapping. Intensities of lipid signal components of the oil in the balloons were similar but not equal to those of fat in porcine or human adipose tissue. Therefore, minor phase deviations occurred in phase mapping under so-called in-phase conditions (echo times which usually lead to maximum alignment of transverse magnetization of water and the sum of lipid signals). However, the results reported on water signals are not affected from these deviations. Both, simulations and experiments resulted in T_2^* relaxation times of water ranging from 5 ms to 8 ms at 3 T. This indicates that gradient echo measurements of water signals originating from clustering macrophages in adipose tissue are probably feasible, but relatively short echo times have to be used. Simulations and measurements predict a broad non-Lorentzian frequency distribution for the water signal resulting in a fast non-exponential signal decay for gradient echo imaging. Negative effects for water detection with modern multi-echo Dixon sequences must also be taken into account, since these techniques are based on the assumption of exponentially decaying signals which is obviously not fulfilled for the water signal of adipose tissue. Since WRC in adipose tissue show very small extension and distinct field inhomogeneities, diffusion effects might cause undesired signal dephasing which cannot be compensated by standard spin echo sequences (similar to the situation in the lung). Choosing short echo times is therefore preferable for spin echo sequences as well. Relatively short T_2 and T_2^* values must be expected for water signals of water compartments in fatty tissue when compared to water signal characteristics of parenchyma tissue in organs like liver, kidney, or brain. Even musculature with T_2 values of about 30 ms shows clearly longer relaxation times. It can be concluded that images recorded with long echo times (e.g., T_2-weighted images with typical echo times of 100 ms) are not

sensitive to water in adipose tissue. The water line width is also relevant for ^{1}H localized spectroscopy. A broad water line with low intensity must be expected from the simulations and phantom measurements. The recorded porcine fat spectrum with FWHM = 70 Hz ± 4 Hz for the water signal confirms the results from simulations and phantom measurements qualitatively. It is interesting that the water line has a significantly larger width compared to the fat signals from the same specimen. Field inhomogeneities within the WRC are clearly more pronounced than inside the big fat vacuoles of the adipocytes. Findings are in contrast to usual spectra showing a more or less uniform line width. In spectra of adipose tissue, the water signal intensity can easily be underestimated, or water signal contributions can even be misinterpreted as a baseline effect.

Conflict of Interest

The authors declare no conflict of interest.

3. Part II: Spatially resolved free-induction decay spectroscopy using a 3D ultra-short echo time multi-echo imaging sequence with systematic echo shifting and compensation of B_0 field drifts

Anja Fischer[1], Petros Martirosian[1], Thomas Benkert[2], Fritz Schick[1]

[1] Section on Experimental Radiology, University of Tübingen, Germany

[2] MR Applications Predevelopment, Siemens Healthcare GmbH, Erlangen, Germany

published in

Magnetic Resonance in Medicine 2022, 87(5): 2099-2110 (71)

Abstract

Purpose: Biologically interesting signals can exhibit fast transverse relaxation and frequency shifts compared to free water. For spectral assignment, a UTE imaging sequence was modified to provide pixelwise free induction decay (FID) acquisition.

Methods: The UTE-FID approach presented relies on a multi-echo 3D spiral UTE sequence with six echoes per RF excitation (TE_{min} 0.05 ms, echo spacing 3 ms). A complex pixelwise raw data set for FID spectroscopy is obtained by several multi-echo UTE measurements with systematic shifting of the readout by 0.25 or 0.5 ms, until the time domain is filled for 18 or 45 ms. B_0 drifts are compensated by mapping and according phase correction. Auto-regressive extrapolation of the signal is performed before Gaussian filtering. This method was applied to a phantom containing collagen-water solutions of different concentrations. To calculate the collagen content, a 19-peak collagen model was extracted from a non-selective FID spectrum (50% collagen solution). PDCF (proton-density collagen-fraction) was calculated for 10 collagen solutions (2%–50%). Furthermore, an *in vivo* UTE-FID spectrum of adipose tissue was recorded.

Results: UTE-FID signal patterns agreed well with the non-spatially selective pulse-acquire FID spectrum from a sphere filled with 50% collagen. Differentiation of collagen solution from distilled water in the PDCF map was possible from 4% collagen concentration for a UTE-FID sequence with 128×128×64 matrix (voxel size 1×1×2.85 mm^3). The mean values of the PDCF linearly correlate with collagen concentration.

Conclusion: The presented UTE-FID approach allows pixelwise raw data acquisition similar to non-spatially selective pulse-acquire spectroscopy. Spatially resolved applications for assessment of spectra of rapidly decaying signals seem feasible.

Keywords: ^1H localized spectroscopy, collagen, endogenous contrast methods, magnetic resonance imaging, spatially resolved spectroscopy, UTE imaging

Introduction

Signals from biologically interesting compounds in tissue (e.g., choline, creatine, N-acetyl-aspartate (72), collagen (73), or proteins leading to the so-called macromolecular signals in brain spectra (74) (75) (76)) are usually frequency shifted compared to free water. These frequency shifts are mainly caused by the well-known chemical shift effects, but water protons in molecules attached to proteins can experience additional induced frequency shifts. Myelin water signals for example have been reported to be slightly frequency shifted when compared to free water signals (77) (78).

Due to their fast transverse relaxation water signals of myelin (79) and ^{1}H signals from water and collagen in tendons and bones (80) are only detectable at very short echo times, as enabled by UTE imaging or pulse-acquire spectroscopy sequences.

Spectroscopy techniques are required for proper assessment of multiple frequency components. Common CSI or MRSI (81) (82) methods with 2D or 3D Cartesian spatial encoding of FID signals apply phase encoding strategies between RF excitation of the magnetization and the start of signal acquisition, leading to an inevitable delay of at least about 1 ms.

In contrast, UTE imaging sequences are capable of acquiring signals immediately after excitation ($TE_{min} \approx 0.05$ ms), since spatial encoding is mainly performed after recording data for the center of k-space. Therefore, UTE imaging is more sensitive to rapidly decaying signal components. However, the frequency spectrum of contributing signals cannot be decompensated. In previous applications of UTE sequences for characterization of signal components with short T_2 times, only the signal amplitude values were determined and analyzed as a function of the echo time (83) (84). While this method is very well suited to estimate the relaxation behavior of a single frequency component (i.e., when no other frequency-shifted signals need to be considered) (85) it does not allow a distinct assessment in the case of multiple frequency components contributing to the UTE signal. As mentioned above, a distinct analysis of the signal components requires phase sensitive measurements at different delay times as it is done by spectroscopy sequences.

The present study aims to record a complex time signal with a UTE imaging sequence, thus, providing spatial encoding and spectral information simultaneously. Therefore, this is essentially a spatial-spectral encoded MRSI sequence based on six to 15 temporal interleaves acquired with a stack of spirals 3D UTE sequence. The comparably high number of interleaves is necessary to ensure the required spectral range. However, since the underlying UTE imaging sequence in contrast to common MRSI sequences (86) enables the detection of ultra-short echo times this approach is more specifically referred to as UTE-FID. The FID time signal of the UTE sequence is intended to correspond largely to a non-selective pulse-acquire spectroscopy, but with an advantage that this is recorded separately for each imaging voxel. To limit the measurement time, a multi-echo 3D spiral UTE was used to record six equidistant echoes after each excitation. The time points in-between the six echo times were recorded by repeated application of the UTE sequence with suitably shifted echo times. Since active gradient switching in UTE sequences results in a significant temporal and slightly location dependent B_0 field drift over time (87), appropriate phase correction procedures had to be implemented.

The method was evaluated in phantoms with solutions of collagen powder, which has several different chemical shift components with different relaxation properties. Collagen was chosen since its behavior is comparable to that of other macromolecules, and quantification studies based on UTE measurements already exist. Siu et al. (31) presented a bi-exponential approach using a single collagen frequency to fit the magnitude of the signal obtained by UTE imaging. This approach was reported to allow the detection of collagen from a concentration of approximately 10 g per 100 ml.

Methods

All measurements were performed on a 3T whole-body imager MAGNETOM Prisma^{Fit} (Siemens Healthcare, Erlangen, Germany). The UTE imaging measurements on phantoms with multiple samples were conducted using a 20-channel head-neck coil, while standard non-localized FID-spectroscopy and single-voxel localized STEAM-spectroscopy according to (88) of a sphere filled with 50% collagen solution were executed with a wrist coil. Furthermore, *in vivo* UTE imaging

measurements on a knee were acquired with a knee coil. All coils were selected as they best matched the respective phantom size and geometry, therefore ensuring the highest SNR.

UTE Measurements

A prototypical 3D UTE prototype sequence using a non-selective rectangular RF excitation pulse (with duration of 60 µs) was applied for data acquisition. Slice encoding was achieved by phase encoding. k-Space is sampled by stack of spiral trajectories (51; 89). The UTE sequence allowed recording of raw data for six echo times after each RF excitation. In order to obtain a complete time signal for each voxel with equidistant temporal spacing, the UTE sequence was applied repeatedly with shifted echo times (shifts ΔTE of 0.25 ms or 0.5 ms were used; dwell time is corresponding to ΔTE) analogous to the concept of temporal interleaving in spectral-spatial encoding. A scheme of the sequence is depicted in Figure 23.

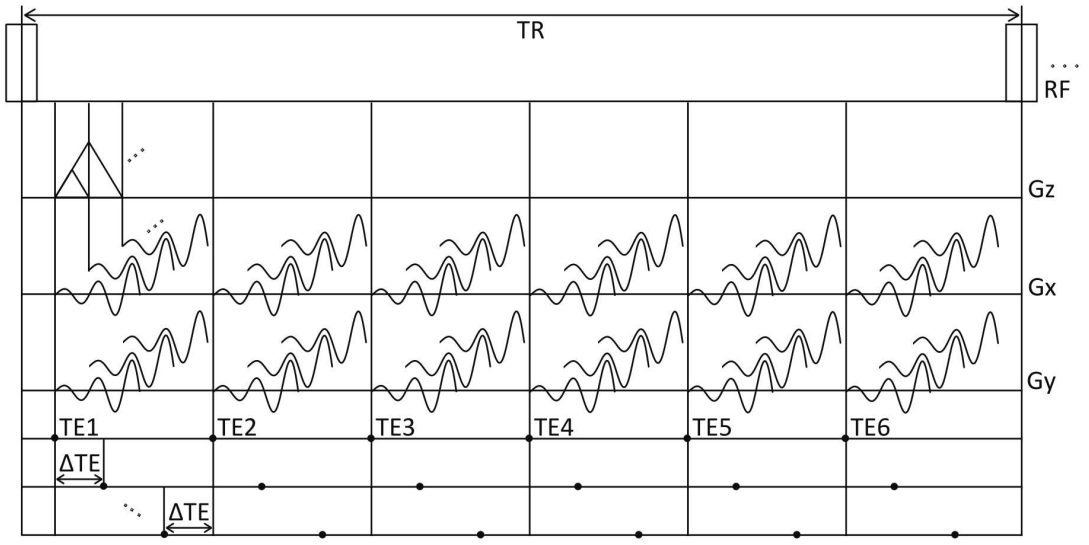

Figure 23. Timing scheme of the UTE-FID sequence. Six equidistant TEs (TE1, TE2, …, TE6) are recorded after each RF excitation. k-Space for each TE is sampled by a stack of spirals. To achieve a temporal spacing of sampling points suitable for spectroscopy, further acquisitions are required using shifted TEs. The TE spacing ΔTE corresponds to the desired dwell time for the spectrum

The 3D UTE sequence recorded images of 64 slices with a 2.85 mm thickness for six different echo times within one acquisition. For a first data set, this sequence was repeated 15 times with a repetition time TR of 49 ms to obtain 90 equidistant echo times between TE_1 = 0.05 ms and TE_{90} = 44.55 ms (resulting in a spectral dwell time of ΔTE = 0.5 ms which translates into 2 kHz spectral bandwidth and,

thus, covers the entire collagen spectrum, which extends over approx. 1200 Hz at a field strength of 3 T). All the echo times of the UTE imaging sequence are, thus, corresponding to delay times TD (with TD being the time delay between RF excitation and time of recording central data of k-space) in the time domain for the FID spectrum. The measurement time for recording this data set was approximately 67 min, which limits clinical applicability. Therefore, a second data set with 72 echo times between TE_1 = 0.05 ms and TE_{72} = 17.8 ms (ΔTE = 0.25 ms) was recorded within 24 min using a reduced TR of 22 ms. This strategy led to oversampling regarding the chemical shift range of collagen signals at 3 T, but would be adequate for higher field strengths as 7 T. Subsequently, for further analysis of the collagen solutions at 3 T every second echo time of this data set was omitted (resulting in ΔTE = 0.5 ms) to evaluate the feasibility of a further reduction of measurement time to 12 min.

Measurements of Static Magnetic Field Drift and Phase Correction

Frequent gradient switching of the UTE sequence led to heating of the system (especially the shim irons) and consequently to significant drifts of the static magnetic field B_0 over time as reported by Hui et al. for 95 different 3T MR scanners (50). Therefore, undesired influences on the frequency and phase of the signals recorded several minutes after the start of the measurement occur. For this reason, B_0 drift-related phase shifts were mapped, and a respective phase correction was implemented to compensate for these effects. Before evaluating the complex data sets, a temporally and spatially dependent phase correction was performed.

The phase shifts resulting from B_0 drifts must be corrected when the signals (separately for each pixel) are used as complex data in the time domain for the FT, which finally leads to complex spectra in the frequency domain. For an adequate temporal phase correction, a reference region in or near the investigated sample is needed in which only a single frequency contributes to the signal (e.g., pure water). The average phase within this region was fitted for each UTE acquisition as a function of echo time by a linear model. Ordinate intercept and gradient of the measured reference phase over time are used to determine correction factors (initially uniform for the entire spatial region).

For extended samples a location-dependent phase correction can be applied. In the phantom measurements, a mask of areas containing pure water was created, and B_0 field maps were derived from the phase images of the successive UTE recordings. A 2D third-degree polynomial function was used to compensate for spatial differences in the B_0 field drift in the images. Location dependent zero and first order phase factors are added to correct for the spatially dependent B_0 field drift for each individual recording.

Calculation of localized UTE-FID spectra

Localized ^{1}H FID spectra for selected regions of interest (ROIs) in the phantom (with uniform content) were calculated from the UTE data. For this purpose, the complex UTE image data from the respective region were first corrected for time- and location-dependent field drift effects. In this process, the complex signal values for each point in the time domain were averaged over all pixels in the ROI. This formed the basis for extrapolation of the measured FID to longer delay times TD (which were not recorded) by a 60^{th}-order auto-regressive model based on Burg's method (90) for the data set with 72 and 90 data points in the time domain, and 30^{th}-order for 36 points in the time domain, respectively. Subsequently, a Gaussian filter (σ = 10 ms) was applied to the FID, and then a FT was performed. The effect of the extrapolation and filtering on the spectrum and FID respectively are depicted in Figure 32.

Standard FID spectroscopy

For comparison, a non-localized standard FID (pulse-acquire) spectroscopy sequence from the manufacturer was applied, providing a minimum TE of 0.15 ms for the first data point in the time domain. This sequence recorded 2048 time points with a dwell time of 0.5 ms. Spectra with and without water suppression were recorded gathering 32 acquisitions with a TR of 1500 ms.

Volume-localized STEAM spectroscopy

Results were further compared to those of spatially resolved single-voxel spectroscopy: A volume-selective STEAM sequence according to (88) with TE = 5.4 ms, TM = 75 ms and TR = 1500 ms was applied, recording 1024 time

points in the time domain with a dwell time of 0.5 ms. For each spectrum, 16 acquisitions were acquired from a volume of 10x10x10 mm^3.

Collagen Phantoms

Different collagen concentrations in aqueous solution were obtained by dissolving 6 g, 12 g, 24 g, 36 g, 48 g and 60 g of NEOCELL (Nutranext, Sunrise, Florida, United States) collagen type 1 and 3 powder in 60 g distilled water. Six blue caps containing these different solutions ranging from 9.1% to 50.0% were placed in a cylinder (diameter 13 cm, height 16 cm) filled with distilled water. This phantom with six known collagen concentrations was used for UTE measurements with 90 and 72 echo times. A ROI of 10x9 pixels was placed in the pure distilled water between blue caps for temporal phase correction (Figure 25B), while for location-dependent phase correction the entire area of distilled water was utilized (see Figure 29A and E). Circular ROIs with a radius of ten pixels were evaluated for each solution to calculate localized FID spectra for all collagen concentrations.

A quantitative determination of collagen concentration was also attempted using the UTE-FID approach with the phantom mentioned above. In addition, to evaluate the sensitivity to low collagen concentrations, the blue caps originally filled with 16.6%, 28.6%, 37.5%, and 44.4% collagen solution (in mass percent) were replaced with blue caps filled with 2%, 4%, 6%, and 8% collagen solutions. Only a UTE data set consisting of 72 echo times was recorded for this purpose.

For non-localized FID spectroscopy and volume-localized STEAM spectroscopy, a thin-walled glass sphere with 20 mm radius was filled with 50% collagen solution (mass percent) again using the NEOCELL collagen type 1 and 3 powder.

Estimation of Proton-Density Collagen-Fraction (PDCF)

Diefenbach et al. (91) presented a generalized method to separate different chemical species based on multi-echo gradient echo-based complex imaging data. Their open-access Python computer programs were used to separate collagen and water signal based on the corrected complex UTE datasets. A bi-exponential model was chosen allowing different relaxation times for collagen and water (somewhat simplified as the collagen signal components show different relaxation behavior). The pixel-by-pixel estimation of the collagen fraction is based on a signal model

derived from a non-localized FID spectrum with 32 Hz water saturation of a 50% solution of the collagen powder in distilled water. MATLAB® R2020a was used to fit eleven peaks (seven between 0.3 and 2.3 ppm and four between 3.2 and 4.2 ppm) with frequencies below (upfield) water and eight peaks (between 6 and 9 ppm) above the water frequency (downfield). Fitting was performed with a multi-Gaussian model provided by MATLAB® based on non-linear least squares allowing for a maximum of 8 components. The measured collagen spectrum, the extracted collagen model and the residuum are depicted in Figure 24. The chemical shift of each signal contribution (0.644 ppm, 0.942 ppm, 1.122 ppm, 1.286 ppm, 1.398 ppm, 1.709 ppm, 2.024 ppm, 3.307 ppm, 3.633 ppm, 3.872 ppm, 4.141 ppm, 6.592 ppm, 6.730 ppm, 7.099 ppm, 7.313 ppm, 7.992 ppm, 8.261 ppm, 8.492 ppm, 8.723 ppm) and its normalized magnitude fraction from the integral of each Gaussian curve (0.144, 0.028, 0.081, 0.009, 0.066, 0.116, 0.039, 0.007, 0.150, 0.005, 0.153, 0.013, 0.011, 0.016, 0.007, 0.029, 0.056, 0.021, 0.081) were extracted and taken as *a-priori* knowledge.

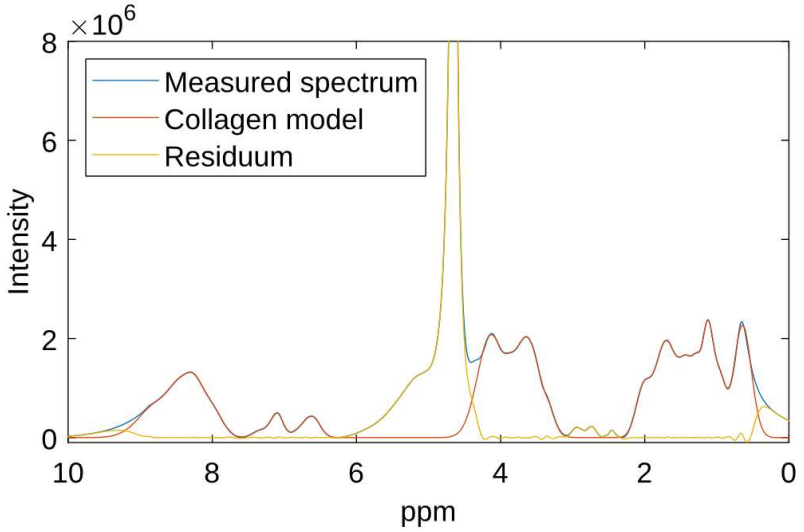

Figure 24. Spectrum of 50% collagen solution with 32 Hz water saturation (blue), fitted 19-peak collagen model (red), and residuum (yellow)

The fitting performance of the chosen model was improved by initial B_0 field mapping based on the phase images of the first acquisition. Analogous to the proton-density fat-fraction (PDFF) according to Reeder et al. (92) a PDCF was calculated based on the resulting “collagen images” and “water images”. The fitting program provides a map showing the Euclidean norm of the residual. This norm

was used to exclude voxels with an unsatisfactory fitting result (Euclidean norm of residual > 1 000).

In vivo UTE imaging measurements of the knee of a healthy volunteer

UTE images of the knee of a 32-year-old, healthy, female volunteer were acquired after giving informed consent for 36 different echo times with analogous measurement parameters to the phantom data set with corresponding number of echo times. Temporal and spatial correction were conducted in the adipose tissue. Therefore, the phase shift of fat compared to water was calculated for each echo time based on chemical shifts (1.3 ppm, 0.9 ppm, 2.05 ppm, 2.75 ppm, 2.3 ppm, 5.28 ppm, 4.18 ppm) and relative contributions (0.51, 0.24, 0.09, 0.02, 0.025, 0.035, 0.08) of a 7-peak fat model. After subtraction of the calculated phase shift, the algorithms of temporal and spatial correction used for the water areas in the phantom study were applied. A localized UTE-FID spectrum is calculated for a 2-by-2-pixel ROI within the subcutaneous adipose tissue.

Results

Static Magnetic Field Drift and Phase Correction

Precise spatial-temporal mapping of B_0 field drift was performed by repetitive measurements with a UTE sequence with unchanged echo times. Thus, temporal B_0 drifts result in easily accessible phase shifts of recorded signals. Figure 25A depicts the progression of phase shift in a ROI containing pure water for 12 consecutive measurements (each of them with six unchanged echo times: 0.05 ms, 3.05 ms, 6.05 ms, 9.05 ms, 12.05 ms, 15.05 ms). For the series of measurements, the same sequence with a duration of 2 min was repeated twelve times without intermission. For example, the signals recorded at the longest echo time (15.05 ms) exhibit a phase drift of more than 0.6 rad corresponding to a frequency drift of ~6 Hz after 24 minutes of continuous UTE imaging.

Figure 25B, C and D show phase shift images (unwrapped phase images corrected by the initial field inhomogeneities of the first acquisition) at TE = 17.8 ms (sixth echo of the twelfth acquisition of the recording with shifted echo times). Figure 25B shows the remaining B_0 drift-related phase shift in a slice without correction, whereas Figure 25C depicts the same phase shift image after temporal drift

correction of all pixels with the same value obtained from the water area marked in Figure 25B. For some areas remote to the reference area, phase shifts up to 0.3 rad (~ 3 Hz remaining spatially dependent field drift) still occur for the sixth echo of acquisition number twelve. Figure 25D shows the situation after temporal and spatial phase correction. It is obvious that further spatial correction clearly reduces remaining local phase shifts. Without correction, the overall phase drift over time was found approximately two times higher than maximum spatial differences in our phantom with a diameter of 13 cm.

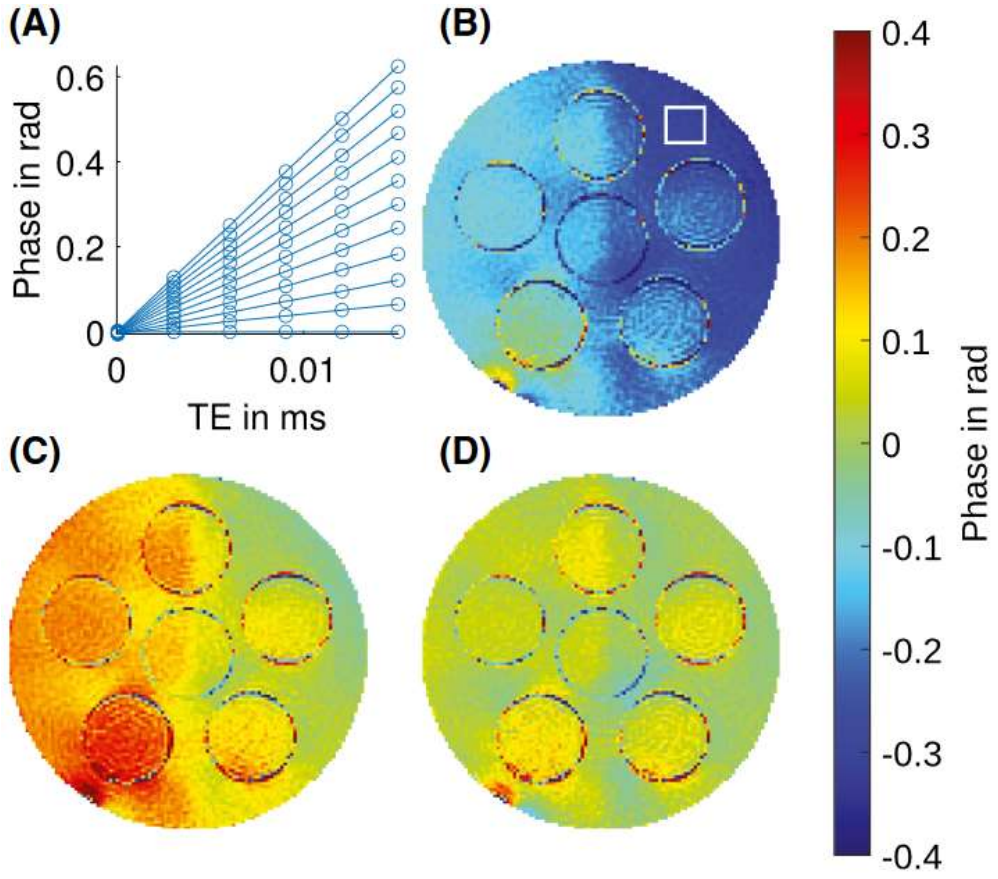

Figure 25. (A) Temporal progression of the drift of averaged phase values within a water ROI for all six echoes in a series of 12 successive UTE measurements with a duration of 2 minutes without intermission. The gradient of the phase values increases from acquisition to acquisition with a faster increase in the beginning. (B) Phase image recorded at TE = 17.8 ms (6th echo of the 12th acquisition of the recording with TE offset). The development of the mean phase value inside the white rectangle serves the subsequent temporal phase shift correction. Resulting phase image with temporal phase shift correction only (C) and with temporal and spatial correction (D). All images are corrected regarding field map bias. A B_0 map was calculated from the images of the first acquisition and used to remove influence of the initial field inhomogeneities

Localized UTE-FID spectroscopy

All areas of the examined phantom with water and different collagen concentrations could be analyzed. Both the correction of the B_0 field drift and the analysis of the FID time signals worked sufficiently well. Localized FID spectra were calculated from the 90, 72, and 36 echo time data sets. The spectra obtained for the different collagen concentrations are shown in Figure 26 for all three data sets. A high correlation between signal intensity and collagen concentration was found for all contributions to the signal pattern.

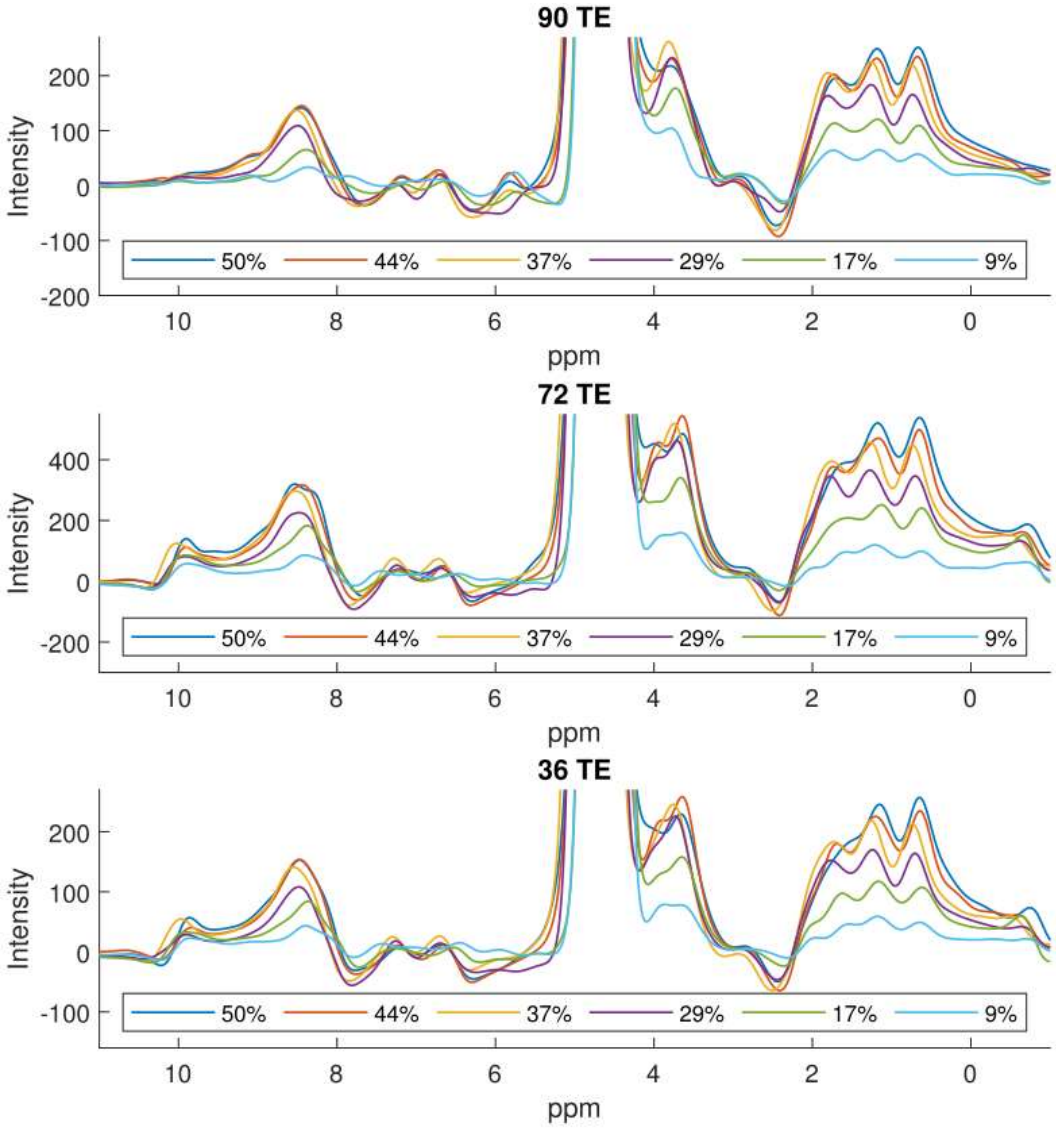

Figure 26. Localized FID spectra taken from the ROIs depicted in Figure 28A based on different numbers and timings of echoes for six different collagen concentrations (values given in mass percent)

Figure 27 shows localized UTE-FID spectra without correction for field drift effects, with a uniform correction over time and with correction for temporal and spatial effects. Localized spectra were calculated from the UTE data set consisting of 72 echo times for six different collagen concentrations. It is obvious that the temporal correction is particularly important as it brings a clear improvement in spectrum quality. Since the field drift in the 3T MRI system used is not very spatially dependent, an additional spatial correction provided only minor advantages for areas situated close to the reference water area.

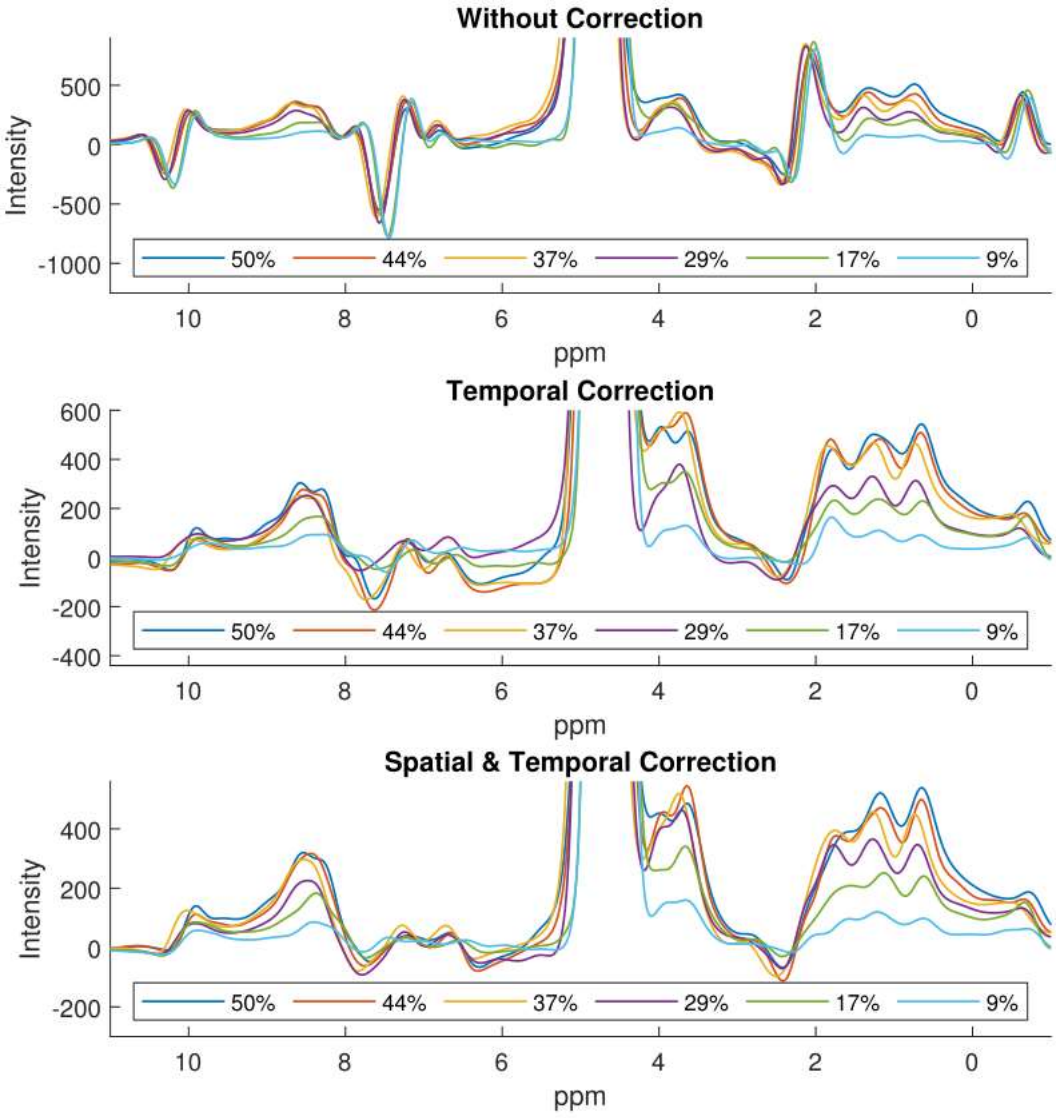

Figure 27. Localized FID spectra obtained from a UTE-FID data set with 72 TEs, ΔTE = 0.25 ms and TR = 22 ms without correction for field drift effects (top), with a uniform correction over time (middle), and with correction for temporal and spatial effects (bottom). Six different collagen concentrations (values given in mass percent) are considered

Figure 28 shows the comparison of a STEAM spectrum recorded with TE = 5.4 ms with a non-localized pulse-acquire FID spectrum and a UTE-FID spectrum (from the UTE data set with 72 echo times) of 50% collagen solution. All three spectra were recorded without water suppression.

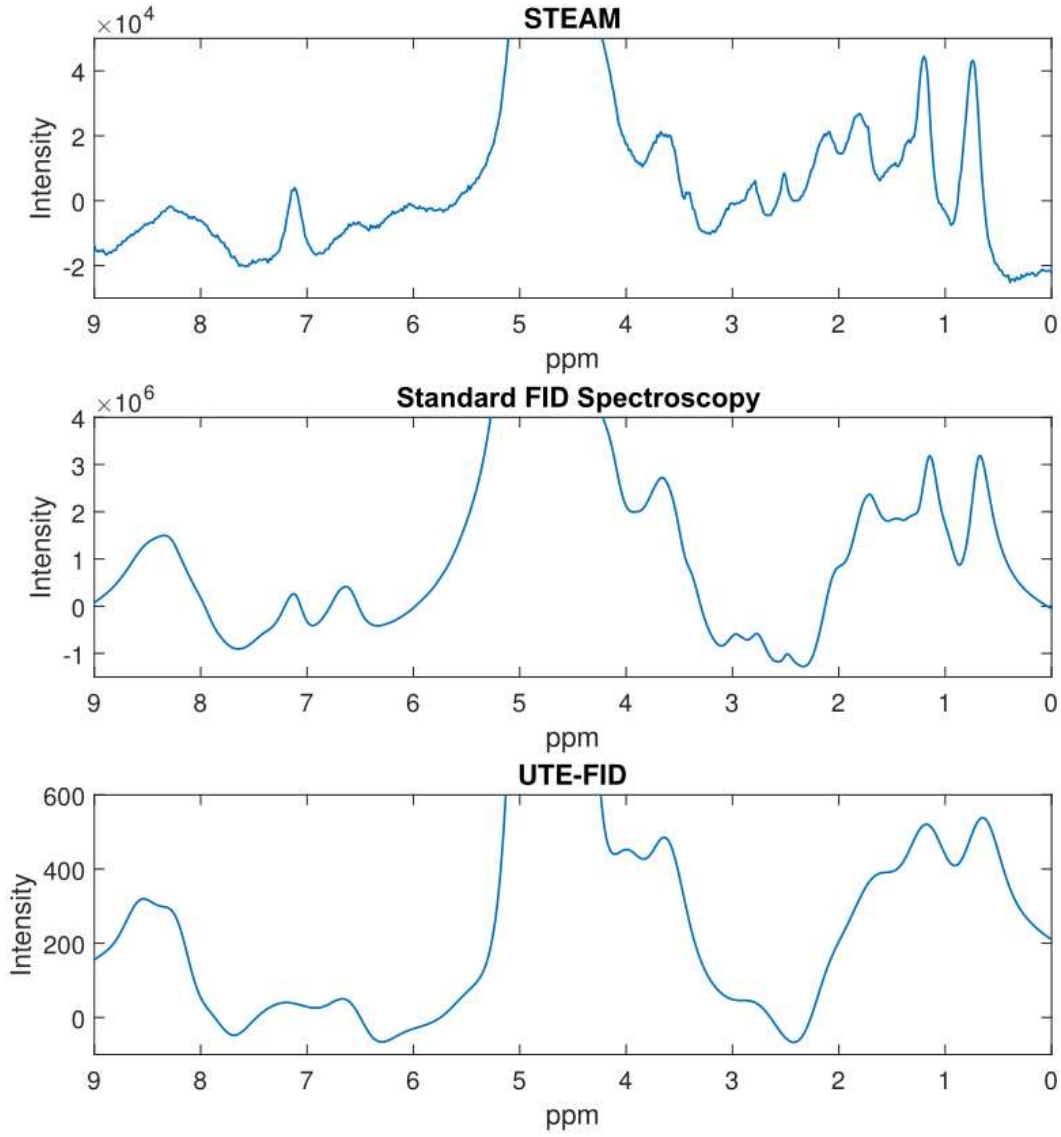

Figure 28. Spectra of 50% aqueous collagen solution: STEAM spectrum with TE = 5.4 ms and TM = 75 ms (top), a non-selective FID spectrum (middle), and a UTE-FID spectrum calculated from the set of UTE images with 72 different TEs (bottom)

The signal pattern in the localized STEAM spectrum shows clear deviations from the localized UTE-FID spectrum. In contrast, spectra from the non-selectively recorded FID (from a spherical sample) and the UTE-FID spectra (from the phantom with multiple samples) show more similarity, but the spectral lines are

wider in the UTE-FID spectrum due to the Gaussian filtering in the time domain. According to Wishart et al. (93) the resonances between 0.5 and 2.5 ppm in the FID spectra are attributable to the aliphatic protons of valine, hydroxyproline, proline and lysin which are the most common amino acids of collagen. The resonances evident downfield of water in all three spectra are similar to those found by Winkler et al. (94) to disappear when the solvent was changed to D_2O. Their origin is assumed to be in exchangeable protons of amine, amide, and OH groups.

Estimation of PDCF (Proton-Density Collagen-Fraction)

The arrangement of the collagen solutions in the phantom and their concentrations in mass percent are incorporated in Figure 29A. PDCF maps were calculated for the UTE data sets with 90, 72, and 36 echo times; they are shown in Figure 29B, C, and D, respectively. For all samples of collagen solution, there is a clear deviation of the determined collagen concentration from surrounding pure water.

In order to better identify the detection limit for collagen, further measurements were performed in which the four mean concentrations of the phantom were replaced by lower concentrations in the range of 2% to 8% (arrangement according to Figure 29E).

The UTE-FID sequence with 72 echo times and $\Delta TE = 0.25$ ms was used. The resulting PDCF map is shown in Figure 29F. From a concentration of 4%, the collagen solution is distinguishable from the surrounding distilled water region.

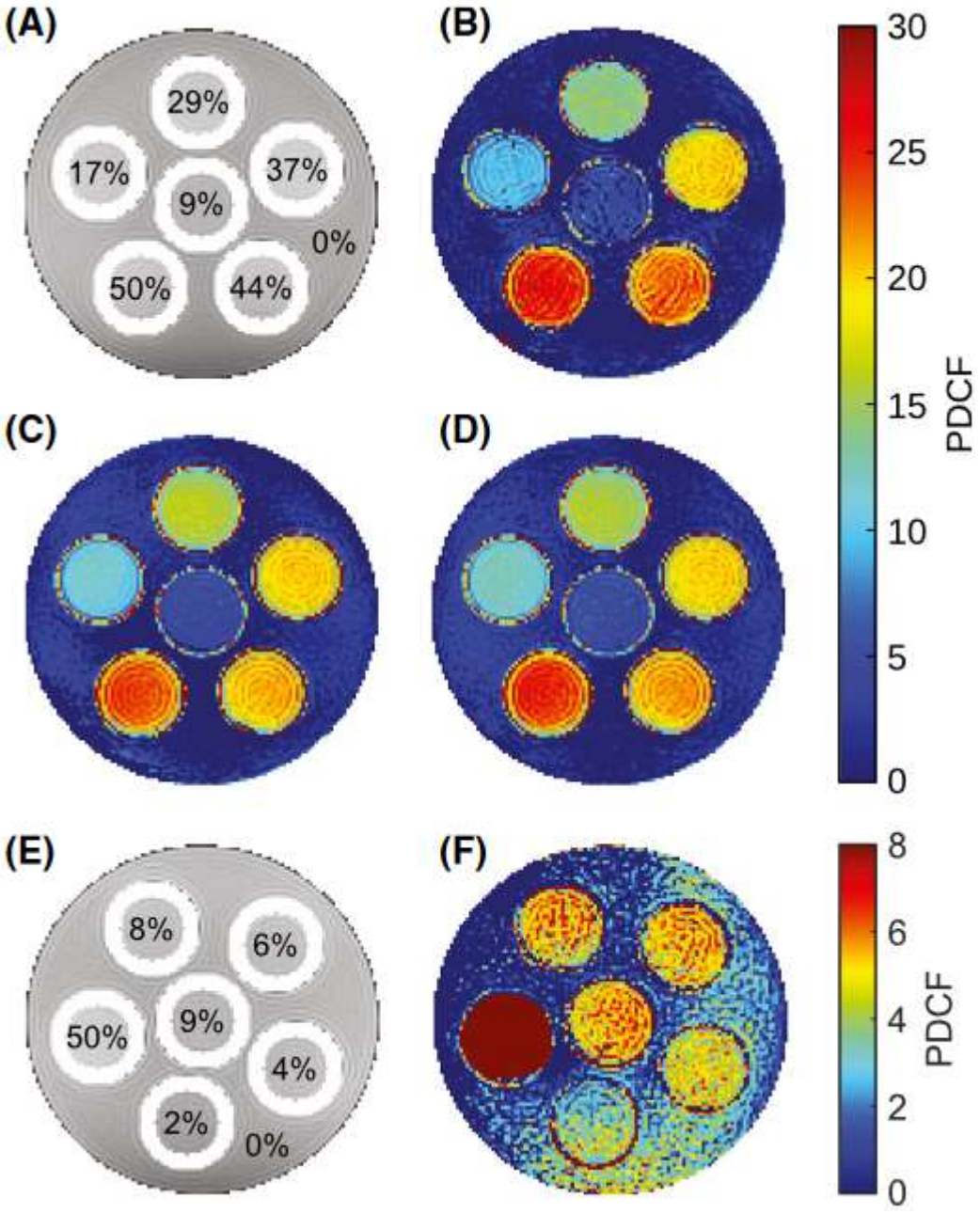

Figure 29. (A) Magnitude image recorded at TE = 0.05 ms indicating the collagen concentration in mass percent for each area of evaluation. The area of distilled water (0%) enabled temporal (ROI depicted in Figure 2A) and spatial drift correction (entire distilled water area). (B) PDCF map obtained using the UTE sequence with 90 TEs, ΔTE = 0.5 ms and TR = 49 ms. (C) PDCF map obtained from 72 TEs with ΔTE = 0.25 ms and TR = 22 ms. (D) PDCF map obtained from 36 TEs with ΔTE = 0.5 ms and TR = 22 ms. (E) Magnitude image at TE = 0.05 ms indicating the lower collagen powder concentrations in mass percent for each area of evaluation in the modified phantom. Again, the area of distilled water (0%) was used for B_0 drift correction. (F) PDCF map of the modified phantom (according to (D)) obtained using the UTE sequence with 72 TEs, ΔTE = 0.5 ms, and TR = 49 ms

The mean and standard deviation of the PDCF were calculated for each sample in a circular ROI with a radius of ten pixels. In addition, the entire area of distilled water was used to define a PDCF reference value at 0% collagen concentration. The results are shown in Figure 30A for the three data sets with 90, 72, and 36 different echo times, respectively.

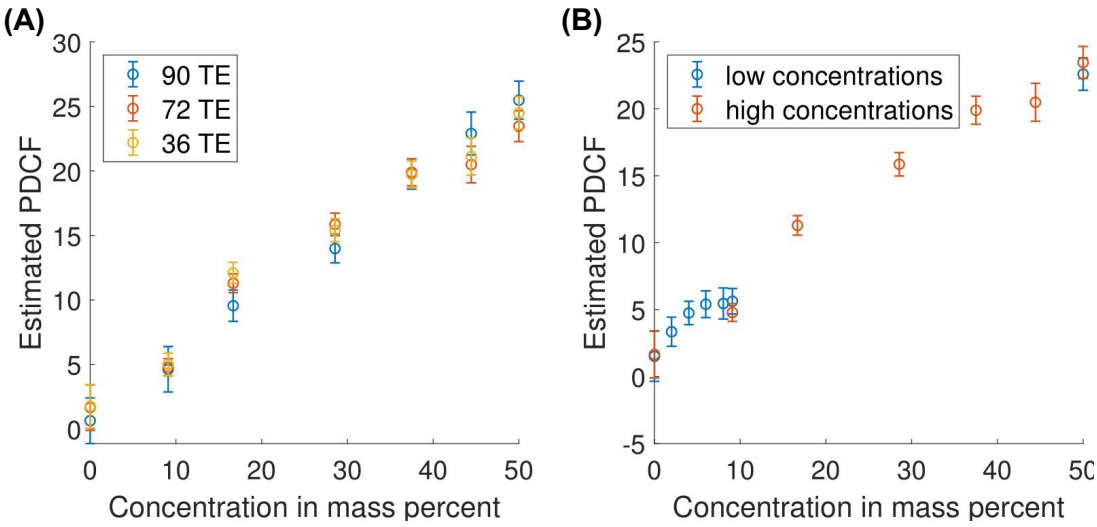

Figure 30. (A) Mean values and standard deviation of the PDCF maps calculated from complex image data at 90 TEs, 72 TEs, and 36 TEs plotted against collagen concentration in mass percent. (B) Mean values and standard deviation of the PDCF maps calculated from complex image data of 72 TEs for all measurements including those with low collagen concentrations

A fit of the measured values to a linear model with a weighting of the individual values with the normalized reciprocal values of the standard deviation was performed separately for all three data sets with high collagen concentrations. The fit parameters are summarized in Table 1.

Table 1. Fit parameters of the linear correlation between estimated PDFC and collagen concentration in mass percent.

Number of TEs	Ordinate section	Gradient	Adjusted R-square
90	0.529	0.501	0.995
72	2.220	0.444	0.962
36	2.473	0.447	0.965

While the acquisition with 90 echo times and ΔTE = 0.5 ms yielded the highest adjusted R-square, no reduction of R-square was found when reducing the number of echo times from 72 to 36 and simultaneously increasing ΔTE = 0.25 ms to

ΔTE = 0.5 ms (according to the sampling theorem). Therefore, a dwell time of 0.5 ms is sufficient for the PDCF estimation at 3 T but should be shortened accordingly at higher field strengths.

The mean values and standard deviation of the PDCF obtained from the UTE measurements with 72 echo times for all collagen concentrations are shown in Figure 30B (with PDCF values of the samples with high collagen concentrations shown in red, and PDCF values of the samples with low collagen concentrations in blue). The mean values and standard deviations show significant differences from distilled water already at a concentration of 2%.

In vivo UTE imaging measurements of the knee of a healthy volunteer

Figure 31A shows a UTE image of the knee of a 32-year-old volunteer for the first echo time (0.05 ms). The blue square indicates the 2-by-2-pixel ROI selected for calculation of a localized UTE-FID spectrum. The resulting spectrum is plotted in Figure 31B and is comparable to well-known fat spectra. A dominant CH_2 resonance is evident at approximately 1.3 ppm. Furthermore, the fat resonances of CH_3 (~0.9 ppm), glycerin (~4.1 ppm) and vinyl (~5.4 ppm) are visible. The allylic and α-methylene resonance merge to one line at 2.1 ppm. Additionally, spectral lines at 4.7 ppm and 2.9 ppm are attributed to water and the diallylic fat resonance, respectively.

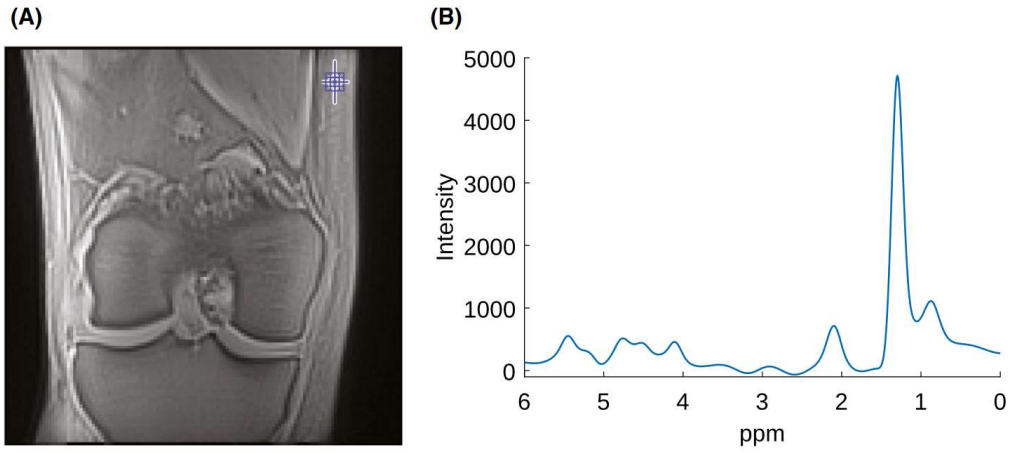

Figure 31. (A) UTE image of a healthy knee at TE = 0.05 ms. The blue square indicates the 2-by-2-pixel ROI selected for calculation of a localized UTE-FID spectrum. (B) Localized UTE-FID spectrum of subcutaneous adipose tissue. The spectral lines are assigned to (CH_3 at 0.9 ppm, CH_2 at 1.3 ppm, allylic fat resonance and α-methylene at 2.1 ppm, diallylic fat resonance at 2.9 ppm, glycerin at 4.1 ppm, water at 4.7 ppm, and vinyl at 5.4 ppm

Discussion and Conclusion

The proposed UTE-FID spectroscopy represents a new approach to localized spectroscopy that is particularly sensitive to rapidly relaxing signals. It was possible to reproduce the signal patterns of dissolved collagen powder known from the non-selective pulse-acquire FID spectrum with good quality, demonstrating an approximately linear dependence of the signal intensities on concentration.

In addition to examining collagen structures such as tendons and ligaments, a possible clinical application is in the detection of organ fibrosis, which according to Zeisberg and Kalluri (95) is responsible for one third of natural deaths worldwide. Excessive accumulation of extracellular matrix is usually caused by prolonged organ damage and can occur in liver, kidney, heart and lung (96), but also in skeletal muscle (97). In a healthy liver, there is about 2% collagen content, whereas in an alcoholic liver in the final stage, an increase to sometimes more than 8% can be detected (98). In order to detect the accumulation of collagen I/III-rich tissue, liver biopsy, despite its local limitation, still serves as the gold standard today (99). However, as this method is associated with various risks, a non-invasive detection would be preferable, especially for follow-up and early detection (100). In addition to ultrasound (fibroscan), MRI offers various possibilities: Current MR methods use contrast agents or measure liver fibrosis indirectly via tissue elasticity, relaxation, diffusion or perfusion (101). The study presented here for direct detection of collagen signals compares well with previous measurements by Siu et al. (12), who, however, only used signal amplitude in UTE sequences and not phase information (as in our approach). The method presented here appears to be advantageous as it allows the discrimination of collagen solution and distilled water in the PDCF map from a concentration of about 4% (compared to previous work with a minimum concentration of about 10%).

Comparing the PDCF maps and FID spectra obtained with different numbers and timings of echo times, the best results could be achieved with 90 echo times. However, UTE-FID records from recording 36 echo times within 12 min recording time are comparable. Shorter recording times advantageously also lead to lower phase drift problems. In general, at least on the 3T whole-body system used, it has been shown that the temporal B_0 field drifts are quite pronounced but can be

successfully corrected. The spatial dependence of the B_0 field drift is rather low, and its correction can certainly be omitted in many possible *in vivo* applications, especially when the evaluation is restricted on small areas. In the collagen phantom with a diameter of 13 cm, the temporal field drift was two times the maximum spatial difference in an axial view. El-Sharkawy et al (87) reported a temporal field drift of 0.7 ppm in 4 hours, while over a comparable distance in axial view a maximum difference in spatial field drift of about 0.4 ppm was observed. The relative amounts of temporal and spatial B_0 field drift are expected to depend on the number and positions of shim irons used to correct for slight magnet manufacturing inaccuracies and are unique to each MR device.

For example, the 2D MRSI spectroscopy at 3 T presented by Chang et al. (102) acquires a matrix of 32x32 voxels with a size of 6.25x6.25x10 mm^3 within 14 min. This method has a comparable measurement time to the presented UTE-FID spectroscopy, but a much lower spatial resolution. However, one disadvantage of the UTE-FID method is the significantly higher stress on the gradient system and the associated heating of the iron pieces used for passive shimming, resulting in B_0 field drifts. The spatial encoding of fast relaxing signals by UTE sequences is also not optimal, since a large part of the spatial information is only read out with a longer delay after the RF excitation. Furthermore, with the UTE-FID approach, only a relatively short time range can be read out directly after the RF excitation when short repetition times (and short examination times) are desired. To obtain narrow lines in the spectrum, the time signals must be extrapolated for longer TD. However, this is usually less problematic, especially since rapidly relaxing signal components for longer TD disappear in the noise. Additionally, motion of body parts might cause interleaving artifacts especially for measurements with a high number of interleaves which however was not the case for the *in vivo* knee study.

For many tissues particularly outside the brain, fat signals are to be expected, which often overlay the desired fast relaxing signals of protein (e.g., collagen). For a meaningful evaluation, the signal model underlying the PDCF determination must be supplemented by the signals of the fat spectrum. However, it can be assumed that by using an approach with multiple signal components, an improvement can be achieved compared to simpler models with often one single frequency for rapidly decaying signals.

The UTE-FID spectrum extracted from a 2-by-2-pixel ROI within subcutaneous tissue exhibits resonances attributable to different fat resonances and thereby demonstrates the feasibility of *in vivo* measurements with the presented ^{1}H localized FID spectroscopy.

Acknowledgements

The MRS package containing the applied STEAM sequence was developed by Edward J. Auerbach and Małgorzata Marjańska and provided by the University of Minnesota under a C2P agreement.

Conflict of Interest

Thomas Benkert is an employee of Siemens Healthineers. All other authors declare no conflict of interests.

Supporting Information

Effect of auto-regressive extrapolation and Gaussian filtering on spectral appearance (a) and FID (b)

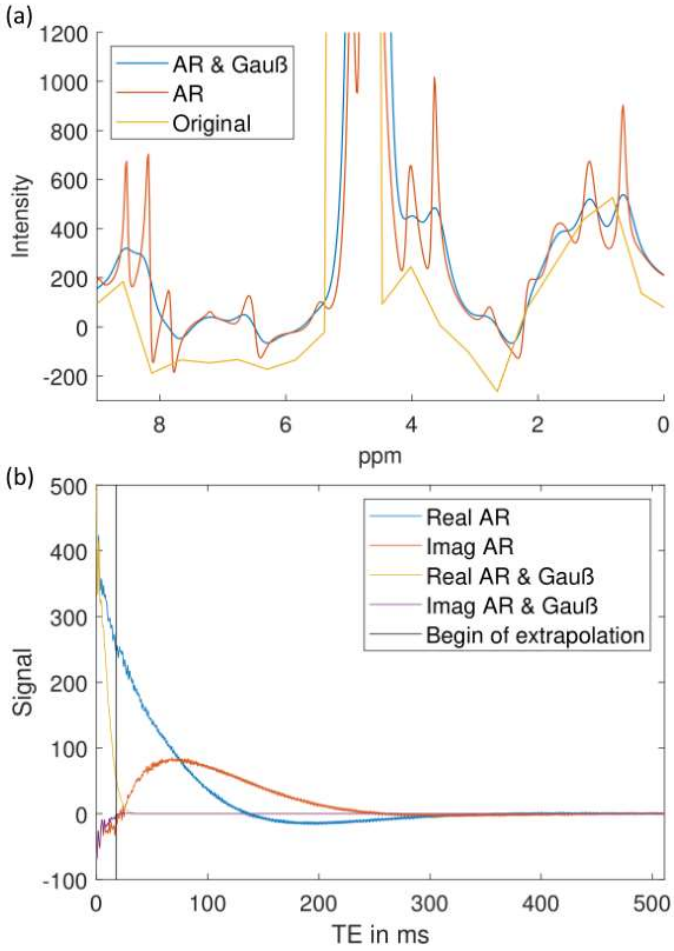

Figure 32. (a) UTE-FID spectrum obtained from 50% collagen solution without further processing in the time domain (yellow), after extrapolation (red) and with additional Gaussian filtering (blue). All spectra are based on a complex data set acquired for 72 different echo times (TE 1 = 0.05 ms; ΔTE = 0.25 ms). Extrapolation is calculated by Burg's method with a 60th order auto-regressive model. The extrapolation expands the FID to 2048 data points and therefore increases spectral resolution. Gaussian filtering with σ = 10 ms smooths the spectrum by decreasing the influence of later (mainly extrapolated) data points in the time domain but also broadens the spectral lines. (b) Complex FID (TE_1 = 0.05 ms; ΔTE = 0.25 ms) of 50% collagen solution containing 72 measured and 1976 extrapolated data points without (blue and red) and with (yellow and purple) Gaussian filtering. The Gaussian filtering accelerates the decay of the FID and therefore decreases the influence of the extrapolated data points after FT. A black line indicates the transition from measurement to extrapolation which is calculated by Burg's method with a 60th order auto-regressive model.

4. Part III: Frequency shifts of free water signals from compact bone – Simulations and measurements using a UTE-FID sequence

Anja Fischer[1,2], Petros Martirosian[1], Jürgen Machann[1,2,3], Bernd Fränkle[4]; Fritz Schick[1]

[1] Section on Experimental Radiology, University of Tübingen, Germany

[2] Institute for Diabetes Research and Metabolic Diseases (IDM) of the Helmholtz Center Munich at the University of Tübingen, Tübingen, Germany

[3] German Center for Diabetes Research (DZD), Tübingen, Germany

[4] Institute of Mechanical Process Engineering and Mechanics, Karlsruhe Institute of Technology, Karlsruhe, Germany

submitted to

Magnetic Resonance in Medicine

Abstract

Purpose: Free water in cortical bone is either contained in a canal system (mainly Haversian canals parallel to the bone axis) and, thus, cylindrical structures or ellipsoidal, approximately spherical pores (lacunae). These porous structures have been reported to crucially influence bone quality and mechanical stability. The purpose of this study is to calculate and measure the frequency distribution in dependence of the geometry.

Methods: FEM (finite element modeling) and analytical approaches were performed to characterize the free water components in cavities of different geometry. The previously introduced UTE-FID technique providing spatially resolved FID-spectra was used to measure the frequency distribution of bone water pixel-wise for different orientations of the bone axis in the outer B_0 field.

Results: A frequency difference between water in spherical pores and water in canals parallel to B_0 of up to approximately 100 Hz at 3 T results. The resulting resonance frequencies showed good agreement with the findings in UTE-FID spectra. If Larmor frequencies from free water in compact bone are compared to outer references (e.g. tissue in the free shaft) shares of free water in cavities of different geometry can be estimated.

Conclusion: Spatially resolved UTE-FID examinations allow the determination of the frequency distribution of short-TE signals from free water in cortical bone. This frequency distribution indicates the composition of the signal contributions from spherical holes and cylindrical canals which allows for further characterization of bone structure and status.

Introduction

Bones form the basic weight-supporting structure in vertebrates therefore serving for protection of various essential organs and tissues (103; 104). These purposes require a particularly resilient material. For this reason, bone mainly consists of hard minerals such as calcium phosphate and collagen fibers (103; 105). These two materials are supplemented by water, which crucially contributes to the mechanical characteristics of bone (103; 106). Based on the structure of the bone, different water compartments are distinguishable: Free water is present in hollow spaces, whereas bound water appears in conjunction with collagen or minerals (106). While bound water is associated with bone mineral density and, thus, stability of the bone, the opposite is the case for free water which provides a marker for porosity (107; 108). For this reason, a sole determination of the total water content in cortical bone is not sufficient to draw conclusions regarding bone quality; it is desirable to evaluate the properties of bound and free water independently of each other. Since the ^{1}H MR signal of bound water relaxes approximately ten times faster compared to free water, biexponential models based on UTE images with their short echo times showed promising results (108). However, off-resonant signal contributions, as for example from fatty tissue adjacent to the relatively thin layer of compact bone, bias the results of this method *in vivo* (109). Furthermore, the magnetic field distribution inside the free water compartments and therefore water resonance frequencies depend on the geometric situation and susceptibilities of bone and soft materials involved. A strong susceptibility difference has been reported between compact bone material and water ($\chi_{\mathrm{bone}} = 11.3 \cdot 10^{-6}$ (68); $\chi_{\mathrm{water}} = 9.035 \cdot 10^{-6}$ (67); $\chi_{\mathrm{diff\,(water-bon\ )}} = -2.265 \cdot 10^{-6}$) which is approximately threefold compared to the difference between fat and water. Therefore, to predict the behavior of the MR signal, it is important to consider the geometries of the water inclusions. The main reservoirs of free water in cortical bone are the Harversian canals with a diameter of approximately 50 µm in the center of the osteon and the ellipsoidal, osteocyte-containing lacunae with approximately 5 µm diameter (110; 111; 112). Furthermore, Harversian canals and lacunae are connected via nearly perpendicularly oriented Volkmann canals and canaliculi (113). The free water is, thus, either present in cylindrical or spherical cavities surrounded by compact bone. For both geometries, mathematical models

concerning the magnetic field distribution have been reported (42). While the magnetic field inside a sphere of relative susceptibility $\Delta\chi$ compared to its surrounding remains unaffected, a magnetic field shift inside the cylinder depending on the angle between the cylinder axis and the main magnetic field results. Consequently, an orientation-dependent resonance frequency shift between the free water signal component originating from cylindrical water containments with respect to the spherical free water component is to be expected which merge to one broad free water resonance. A frequency shift thereof might allow a determination of the ratio between cylindrical and spherical pores. Previous studies have shown that both, aging and osteoporosis are predominantly associated with a dilation of the Haversian canals due to osteoclastic resorption on their inner walls as schematized in Figure 33 (113; 114). Thus, changes of the free water resonance frequency might provide an indicator for osteoporotic changes of cortical bone in addition to the ratio of bound and free water.

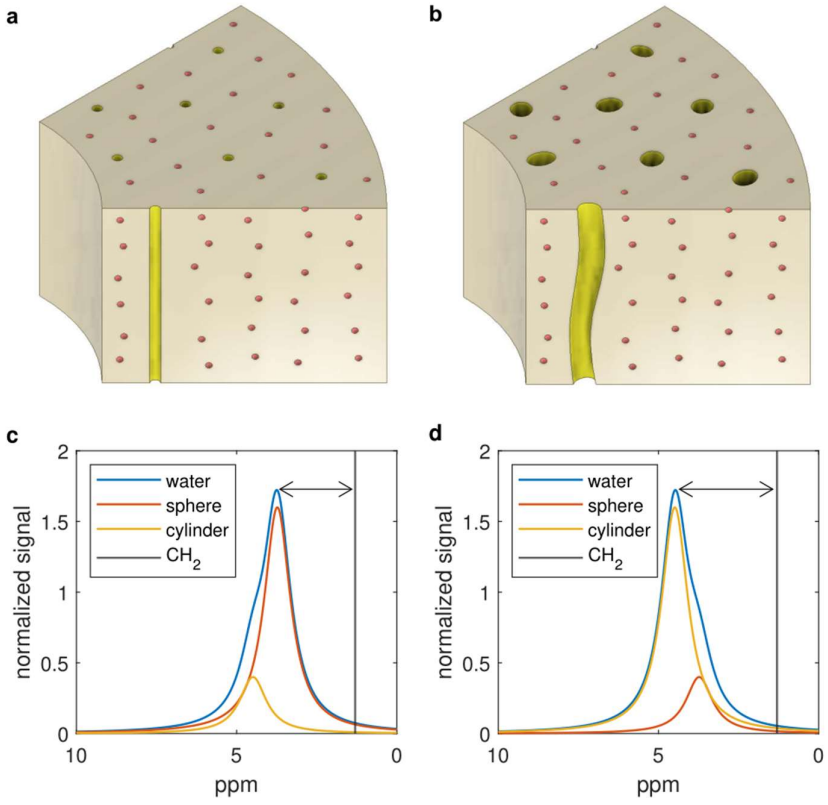

Figure 33. Schematic illustration of the water filled pores in compact bone (yellow: Haversian canals; red: spherical lacunae) before (a) and after (b) dilation of the Haversian canals. Predicted water resonance characteristics simulated for 20% (c) and 80% (d) of free water originating from Haversian canals compared to a methylene reference (black line).

The initial challenge of differentiating bound and free water in cortical bone by MRI was the fast transverse relaxation process of both water components (2-3 ms for free water and 0.2-0.4 ms for bound water at 3T) (108; 115; 116). Standard sequences allowed for the detection of tissues with a transverse relaxation time of more than approximately 10 ms (117). However, with the invention of UTE techniques, MR signals with relaxation times down to 0.001-0.1 ms became accessible (53). By acquisition of multiple images with different TEs, bound and free water components could be differentiated by biexponential models based on the magnitude curve of the signal decay. Additional frequency components bias this model. These off-resonant signal components can either originate from additional chemical components or field inhomogeneities in the cortical bone or represent chemical shift artifacts from signals which originate from outside the considered area. The features of the latter depend on the sequence design. For the UTE sequence with spiral k-space trajectories artifacts from off-resonant signal contributions strongly deviate from chemical shift artifacts in Cartesian sampled images (118). Thus, the present work also investigates the chemical shift artifact obtained by the employed UTE sequence (with spiral readout). Respective influences on the differentiation of bound and free water are analyzed by comparison of examinations of a bovine femur before and after removing the bone marrow from the medullary canal. The present work exploits a newly developed UTE-FID method for calculating spatially resolved spectra from phase sensitive UTE multi-echo imaging (71). First, the geometry of the long bones and the water-containing cavities in the cortical bone are evaluated to draw conclusions about the bulk magnetic susceptibility shift of the free water components. The influence of the geometry of the bone itself is accessed by FEM while the geometry of the cavities is considered by mathematical models. Based thereon a prediction of the resonance frequencies of probably present free water components (one for spherical and one for parallel cylindrical cavities) dependent on the orientation of the bone in the external magnetic field is aimed for. Subsequently, the predictions are compared to the acquired spectra. Thus, the aim of the present study is to analyze the bone water model, which in addition to a bound water component consists of two merging free water components, and its feasibility as a marker for alterations in bone structure.

Methods

Four potential influencing factors were considered in simulations of the magnetic field distribution in compact bone and systematic experiments: [1] the impact of the bone marrow in the medullary canal due to chemical shift artifacts, [2] the influence of the orientation of the bone in the magnetic field on the field distribution, [3] effects on the free water components caused by the geometry of the water cavities, and [4] the detectability of bone quality markers.

Influencing factor [1]: To address the chemical shift artifacts, the proton density fat fraction (PDFF) map obtained by a 3D volumetric interpolated breath-hold examination (VIBE) sequence via multi-point Dixon reconstruction is compared to the PDFF calculated from the complex UTE dataset using a program provided by Diefenbach et al. (119; 120; 121; 122; 91). The algorithm for separation of the water and fat component is based on a 9-peak fat model (123).

Influencing factor [2]: The field distribution dependence on the bone orientation in the magnetic field is estimated with simulations based on the geometry of the long bone and additionally calculated from two phase images (TE=0.05 ms and 3.05 ms) of the UTE acquisition of a bovine femur. Since these echo times do not meet the in-phase condition, measurement-based mappings were calculated only for the hollowed femur, which is assumed to be dominated by the (mean) water frequency. Furthermore, the simulations of the B_0 field distribution are required to estimate the frequency offset relevant for the areas in compact bone considered for the calculation of a UTE-FID spectrum.

Influencing factor [3]: Subsequently, the resonance frequencies of the free water components in cylindrical water cavities parallel to the bone axis and spherical pores in the compact bone can be estimated. Theoretical frequency shifts for 0°, 45° and 90° angulation between bone axis and main magnetic field are compared to results extracted from the UTE-FID spectra.

Influencing factor [4]: Spectra are also evaluated to differentiate bound and free water. Results are compared to a biexponential model based on the magnitude

curve of the FID. Furthermore, an *in vivo* spectrum is exploited to demonstrate the determination of the free water resonance frequency.

Simulation of field distribution in hollow cylinders

FEM using a conjugate gradient solver was performed on COMSOL Multiphysics® 4.3b to simulate the magnetic field distribution and thereby to account for bulk magnetic susceptibility effects. Long bones are characterized by a hollow cylindrical geometry. Therefore, the model is based on a hollow cylinder with a ratio between hole and cylinder of 0.5 which approximately corresponds with the dimensions of the bovine femur. The ratio between length and radius of the cylinder was set to 5 in the simulations. The cylinder features the magnetic susceptibility difference $\chi_{\mathrm{diff\,(water-bon\ )}} = -2.265 \cdot 10^{-6}$ between compact bone and surrounding water. Simulations are performed twice for all three angulations (0°, 45° and 90° towards the main magnetic field) with the cylinder cavity filled with water and bone marrow/fat ($\chi_{\mathrm{marrow}} = 8.2 \cdot 10^{-6}$ (68); $\chi_{\mathrm{diff\,(water-marrow)}} = 8.35 \cdot 10^{-7}$), respectively. For the area of the hollow cylinder and its direct environment the mesh of the finite element model was set to extra fine, while for the surrounding spherical infinite element shell a coarse mesh was found sufficient. This resulted in approximately 212 000 finite elements for the entire geometry. The underlying physical model is based on the (static part of) Maxwell equations and allows for the calculation of the macroscopic field distribution $\vec{B}_{\mathrm{mac}}$. To obtain the external magnetic field $\vec{B}_{\mathrm{ext}}$, the macroscopic field distribution was supplemented by a Lorentz sphere correction according to

$$\vec{B}_{\mathrm{ext}} = \left(1 - \frac{2}{3}\frac{\chi_{\mathrm{diff}}}{(1+\chi_{\mathrm{diff}})}\right)\vec{B}_{\mathrm{mac}} \qquad 28$$

with the magnetic susceptibility difference χ_{diff} of the material compared to water since all simulations are performed with relative susceptibilities with the one of water set at 0 (124).

The magnetic field simulations are extracted for the central slice of the respective cylinder oriented perpendicular to its axis. In the case of the water filled hollow bone cylinder two values are selected: the value at the center of the central hole and the value in the center of the compact bone along the image diagonal. The value from the central cavity of the tube serves for calibration. Therefore, a spectrum is

acquired from the UTE images for this location based on which the frequency shift of the water resonance (deviation from 4.7 ppm) is estimated and exploited as offset correction for the further spectra. The bulk magnetic susceptibility effects described in the following are given as relative values compared to the center of the water filled medullary canal. The location along the diagonal is considered since the extracted value is valid for analogous regions along all four diagonals. Thus 4 ROIs can be evaluated *in vitro*. Furthermore, the bulk magnetic susceptibility shift in this region represents the average shift inside the compact bone of the considered plane for all orientations.

The resulting resonance frequency (derived from the field simulations) is directly attributable to spherical water filled pores whereas an additional geometry-induced frequency shift ΔB must be considered for the cylindrical reservoirs with relative permeability Δx to their surrounding according to

$$\Delta B = \frac{1}{6} B_{\text{ext}} \cdot \Delta x \cdot (3 \cos 2\,\theta - 1) \qquad 29$$

dependent on the angle θ between cylinder axis and main magnetic field (42).

Experiments

Measurements were performed on a 3T whole-body MR imager MAGNETOM Prisma^{Fit} (Siemens Healthcare AG, Erlangen, Germany) using a 20-channel head-neck coil for *in vitro* measurements (and 15-channel knee coil for *in vivo* measurement). Complex raw data was acquired for six equidistant TEs by a 3D UTE prototype sequence using a rectangular, non-selective excitation pulse with 60 µs duration and a spiral duration of 1 600 µs. To reduce the temporal spacing, this UTE sequence was repeated twelve (six) times with shifted TEs resulting in a spectral dwell time of ΔTE=0.25 ms (0.5 ms) and a complex dataset with 72 (36) TEs ranging from TE_1=0.05 ms to TE_{72}=17.8 ms (TE_{36}=17.55 ms). Each dataset consists of 66 slices (160x160 mm^2 FoV, 160x160 matrix size) with a thickness of 2.8 mm and requires a measurement time of 40 min (20 min) using a repetition time of TR=22 ms and sampling k-space by stack-of-spirals trajectories (51; 89). The same resolution was ensured for the Dixon Vibe recordings. An echo train of 15 echoes was acquired (TE_1=1.27 ms) with a repetition time of 20 ms and a bandwidth per pixel of 1184 Hz.

A 15 cm piece from the middle of a bovine femur was placed centrally in a cylindrical water filled container. The container was positioned in the isocenter of the head-neck coil and the scanner and only rotated around its own axis by a defined angle between measurements. The section plane was aligned perpendicular to the bone axis which was oriented at 0°, 45°, and 90° to the external magnetic field B_0. The measurements were first performed with fatty bone marrow inside the medullary canal and repeated with the same measurement parameters after removing the bone marrow (replaced by water).

After obtaining informed consent UTE images for 36 different TEs were acquired of the knee of a female, 32-y-old, healthy volunteer.

Spatially selective UTE-FID spectroscopy studies

Spatially resolved FID spectra from the compact bone are calculated for ROIs of 3-by-3 voxels (3x3x2.8 mm^3) from the UTE-FID datasets according to the procedure of data processing including correction for time- and location-dependent field drift effects proposed in (71). For this purpose, a 20^{th}-order auto-regressive model is used for the extrapolation of 1976 (2012) additional time points (resulting in 2048 data points in total) followed by the application of a Gaussian filter with σ=10 ms. The placement of the ROIs is exemplary depicted for parallel orientation to the main magnetic field in Figure 36a for the hollowed femur, in Figure 37a for the femur containing bone marrow and in Figure 41 for the *in vivo* measurement. *In vitro* it is attempted to place the ROIs along the diagonals in agreement with the area for extraction of the field simulations. For the bone without bone marrow an additional spectrum is acquired in the center of the water filled medullary canal (white 1-by-1 voxel ROI in Figure 36a). The calculation of the spectra is calibrated to 4.7 ppm at the maximum of the water frequency for this ROI. This calibration is performed for each dataset of the water filled bone separately to ensure the comparability of the absolute resonance frequencies. In the case of the femur filled with bone marrow only relative frequency differences of the different water reservoirs are considered.

Fitting of the spatially resolved UTE-FID spectra is performed based on a model consisting of two or three Lorentzian lines, respectively, according to

$$A_1\left(\frac{s_1}{s_1^2+(x-t_1)^2}\right)+A_2\left(\frac{s_2}{s_2^2+(x-t_2)^2}\right)\left[+A_3\left(\frac{s_3}{s_3^2+(x-t_3)^2}\right)\right]+c. \qquad 30$$

The locations of the Lorentzian lines which are defined by the fitting parameters t_1, t_2 and t_3, are restricted to the range of the water resonance between 3.7 ppm and 5.7 ppm, while the other fitting parameters were limited to positive values. The transverse relaxation time T_2^* can be extracted from the fitting parameters s_1, s_2 and s_3 for every water reservoir separately according to

$$T_{2,i}^* = \frac{1}{2} s_i \omega_{\mathrm{L}} \pi \qquad 31$$

with the Larmor frequency ω_{L}. For the fatty marrow filled bone, the spectra are cut off at the turning point between the water resonance and the minimum towards the fat resonance, while the entire spectra are included for the empty (water filled) femur.

The results of this approach are compared to a biexponential model according to

$$A_1 \exp\left(-\frac{x}{T_{2,1}^*}\right)+A_2 \exp\left(-\frac{x}{T_{2,2}^*}\right)+c \qquad 32$$

which is applied to the magnitude curve of the FID. For both, the two-component Lorentzian model and the biexponential model, the bound water share is estimated based on the ratio of A_2/A_1 with A_2 representing the water component with the broad linewidth and the short transverse relaxation time. All fitting procedures are performed using a non-linear least squares algorithm provided by MATLAB® R2020a.

Results

Off-resonance artifacts

The medullary canal appears enlarged and with a corona in the PDFF maps calculated based on the UTE-FID data (Figure 34a bottom half) compared to the multi-echo DIXON Vibe image (top half). These chemical shift artifacts are expected to affect the calculated spectra as well as the FIDs. Spectra and FIDs obtained from three ROIs with different distance (close, central, and distant) to the bone marrow are depicted in Figure 34b and c, respectively. A methylene

resonance from fatty acids is evident in all three spectra but decreases in intensity relative to the water resonance with increasing distance to the medullary canal. This additional resonance is represented by an oscillation in the FIDs of those pixels.

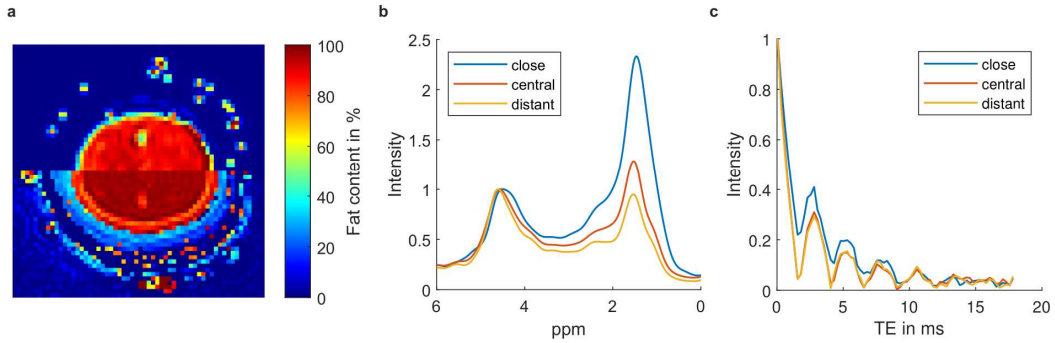

Figure 34. *a. PDFF maps obtained by a GRE-based Cartesian Dixon method on the top and based on the phase sensitive UTE datasets on the bottom. Both measurements are performed at parallel orientation of the bone marrow filled bovine femur. b. Spatially resolved spectra and c. real part of the FID of the compact bone calculated from UTE datasets for three voxels with increasing distance to the medullary canal at parallel orientation of a bovine femur to the magnetic field.*

Field distribution and geometry effects

The simulated field maps are depicted in Figure 35 for 0° (left), 45° (middle) and 90° (right) orientation of the femur axis towards the external magnetic field B_0. The top row features the results for the water filled femur and compares the simulations (upper half) with the measured field maps (bottom half). The field maps simulated for the femur with bone marrow are depicted in the bottom row.

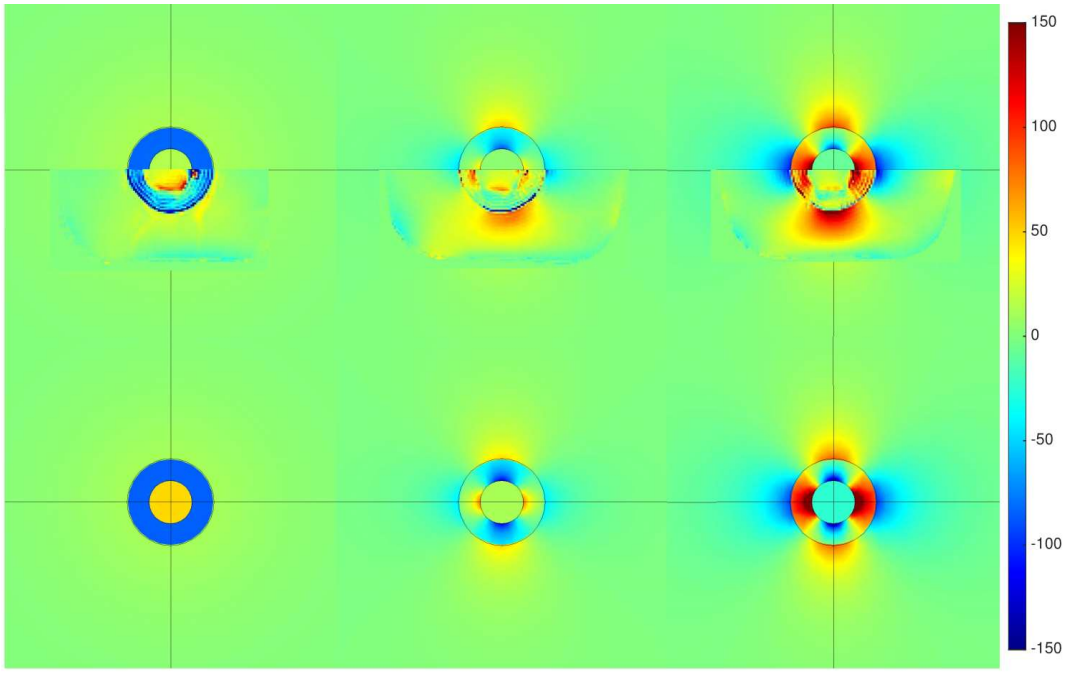

Figure 35. *Field maps simulated with COMSOL Multiphysics® 4.3b for a water filled (top row) and bone marrow filled (bottom row) long bone surrounded by water represented by a long cylinder with a ratio of length to radius of 5 for 0°, 45° and 90° (left to right) orientation of the cylinder axis to the main magnetic field (along z-direction). Field maps obtained from measurements of a hollowed bovine femur are depicted in the bottom half of the top row.*

Field inhomogeneities for water and bone marrow filled bone increase from parallel to perpendicular orientation. Furthermore, the results for the water filled bone show agreement between simulations and measurements. Based on the simulated maps for the water filled bone the frequency shift due to bulk macroscopic magnetic susceptibility effects for the area of the selected ROI is extracted. For this purpose, the frequency difference between the center of the water filled medullary canal and the area of the ROI for the calculation of spectra (in the middle of the cortical layer along the first angle bisector in the upper right quadrant) is estimated. Considering a chemical shift of 4.7 ppm in the center (serves for calibration of the spectra of the hollowed femur), the chemical shift at the location of the ROIs for the extraction of spectra is derived for the three different angulations. Due to the angular symmetry the determination along the bisector in one quadrant is sufficient. While the resulting chemical shift is directly attributable to spherical water containments an additional shift caused by microscopic bulk susceptibility effects based on Equation 29 must be considered for cylindrical cavities. For the bone marrow filled femur a selection of a water reference in the medullary canal is unfeasible. For this reason,

only chemical shift differences between spherical and cylindrical cavities are considered. The resulting resonance frequencies are summarized in Table 2. Since it can be assumed, that both free water components merge to one broad line, the mean value of the chemical shifts of the two free water components is included additionally. This value is subsequently compared to the free water resonance frequency obtained by the two-component Lorentzian model which approximates the free water component with one Lorentzian distribution.

Table 2. *Overview of the expected resonance frequencies in ppm of the free water components originating from spherical and cylindrical porous structures in compact bone based on simulations and the frequency values extracted from measurements. For the water filled bone the resonance frequency at the center of the medullary canal of the considered slice is set to 4.7 ppm and serves as reference. For the bone marrow filled femur only chemical shift differences between spherical and cylindrical cavities are accounted for.*

	Simulations (in ppm)				Water filled Bone (in ppm)				Marrow
Orientation	f_{sphere}	$f_{cylinder}$	Δf	$\varnothing f$	$\varnothing f_{sphere}$	$\varnothing f_{cylinder}$	$\varnothing\Delta f$	$\varnothing f_{2c\text{-}lor}$	$\varnothing\Delta f$
0°	4.00	4.76	0.76	4.38	4.04 ±0.04	4.44 ±0.04	0.40 ±0.05	4.32 ±0.05	0.52 ±0.05
45°	4.50	4.66	0.19	4.58	4.37 ±0.06	4.68 ±0.06	0.31 ±0.09	4.54 ±0.07	0.29 ±0.08
90°	5.07	4.69	-0.38	4.88	4.99 ±0.11	4.55 ±0.06	-0.44 ±0.13	4.73 ±0.04	-0.43 ±0.10

UTE-FID

Figure 36a depicts the placement of the UTE-FID ROIs for the measurements at parallel orientation of the femur without bone marrow (water filled) and surrounded by water, on a magnitude image (TE=0.05 ms). The corresponding spectra are plotted in Figure 36b, and for diagonal and perpendicular orientation in Figure 36c and d, respectively.

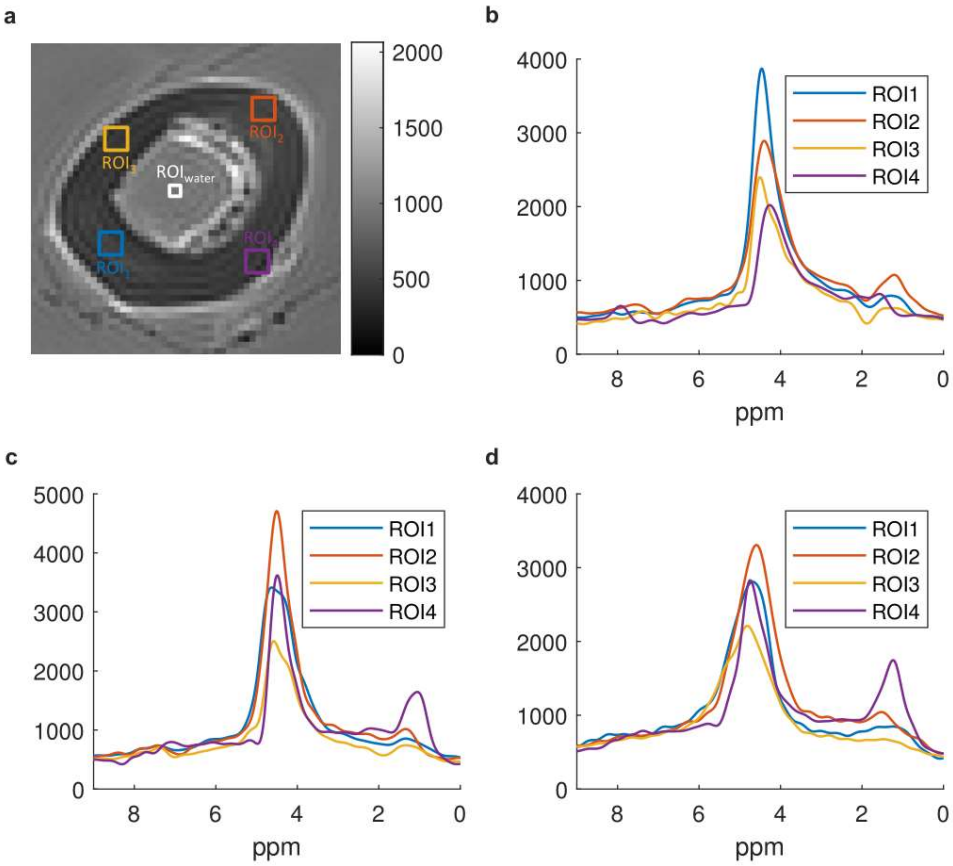

Figure 36. *a. Magnitude image of the slice chosen for evaluation at an orientation of the bone with removed marrow parallel to the external magnetic field. The ROIs used for UTE FID calculation are indicated by squares. The reference water spectrum for the estimation of the water resonance offset is calculated from the area indicated by the white square in the center of the bone. b.-d. Spatially resolved UTE-FID spectra of compact bone for 0°, 45° and 90° orientation of the water filled bovine femur to the external magnetic field.*

Analogously, Figure 37 shows the spectra obtained of the bone marrow filled femur. In contrast to the spectra of the hollowed femur, a second intense resonance line between 1 and 2 ppm occurs in all spectra of the bone marrow filled femur. This spectral line is attributable to chemical shift artifacts of the methylene resonance and is also partially evident in the spectra of the hollowed femur (especially for ROI_4 at diagonal and perpendicular orientation). The resulting fit of the water resonance by a two- and three-component Lorentzian model is depicted exemplarily for ROI_1 at parallel orientation in the graphs of Figure 38. For both spectra the three-component model distinguishes two narrow water resonances. A larger one at approximately 4.5 to 4.6 ppm and a smaller one around 4.0 ppm. Due to this additional component (by splitting the free water component with long T_2^* into two

narrow resonance lines which are attributed to spherical and cylindrical porous structures), the model consisting of three Lorentzian components better reproduces the flanks of the water resonance. Results on the resonance frequencies extracted by the Lorentzian models are summarized in Table 2.

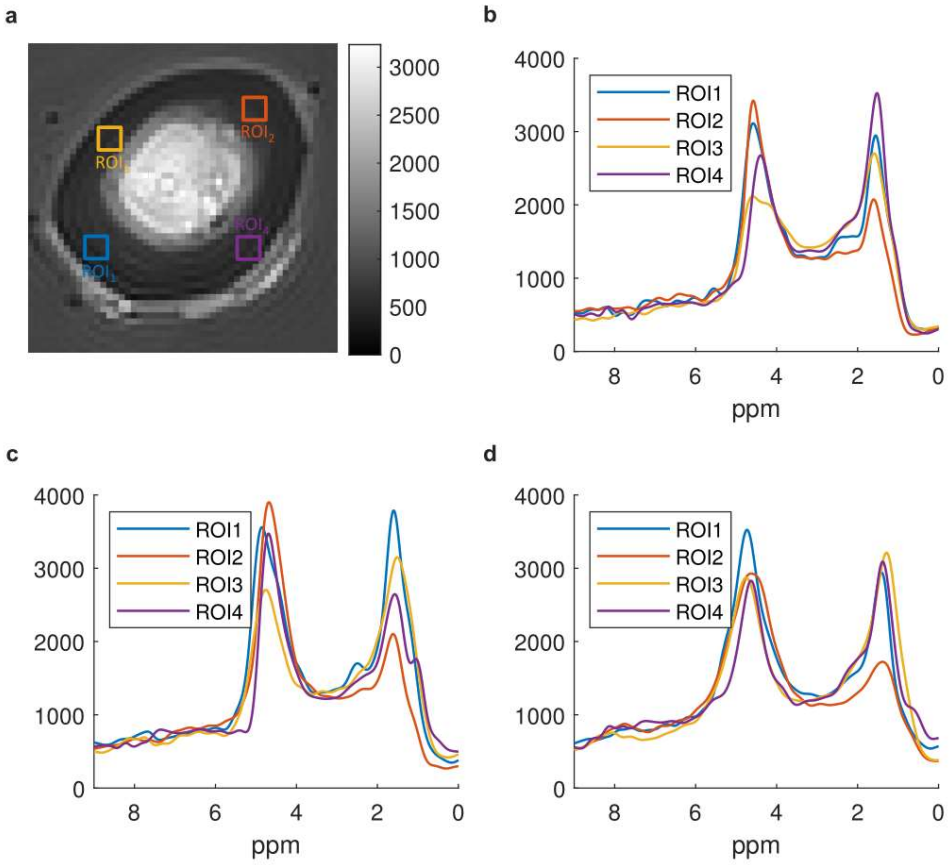

Figure 37. *a. Magnitude image of the slice chosen for evaluation at an orientation of the bone marrow filled bone parallel to the external magnetic field. The ROIs used for UTE FID calculation are indicated by squares. b.-d. Spatially resolved UTE-FID spectra of compact bone for 0°, 45° and 90° orientation of the bone marrow filled bovine femur to the external magnetic field.*

Comparison

Figure 38 summarizes the results of the methods for the water and bone marrow filled femur at parallel orientation to the main magnetic field. The spectra and the FID are extracted from ROI_1 (see Figure 36 and Figure 37). While the restriction to the water resonance in the UTE-FID spectra ensues reproducibility of the fit between the two measurements, the oscillation of the magnitude of the FID for the bone marrow filled femur due to chemical shift artifacts complicates the fit by a biexponential model.

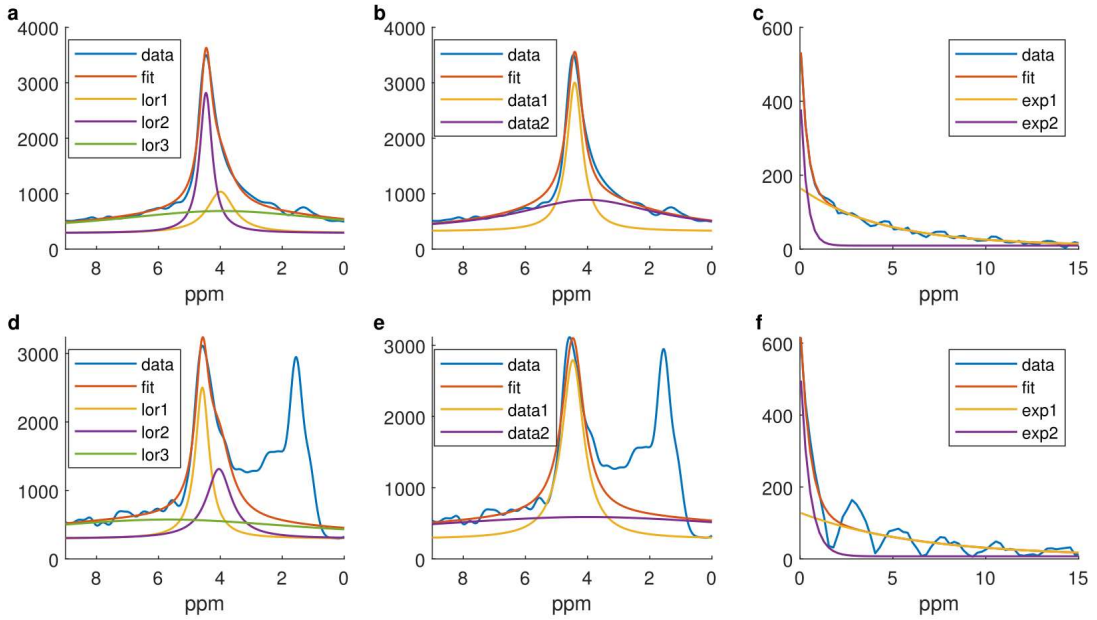

Figure 38. *Evaluation of ROI$_1$ at parallel orientation of the water (a-c) and bone marrow (d-f) filled bovine femur to the external magnetic field. (a, d) Fit of the calculated UTE-FID spectrum (blue) with a three-component Lorentzian model (red) consisting of three Lorentzian distributions (yellow, purple and green). (b, e) Fit of the calculated UTE-FID spectrum (blue) with a two-component Lorentzian model (red) consisting of two Lorentzian distributions (yellow and purple). (c, f) Fit of the magnitude of the measured FID (blue) by a biexponential model (red) consisting of a slowly (yellow) and fast (purple) relaxing component.*

The bound to free water ratio obtained by the two methods (two-component Lorentzian and biexponential) is compared in the graphs of Figure 39.

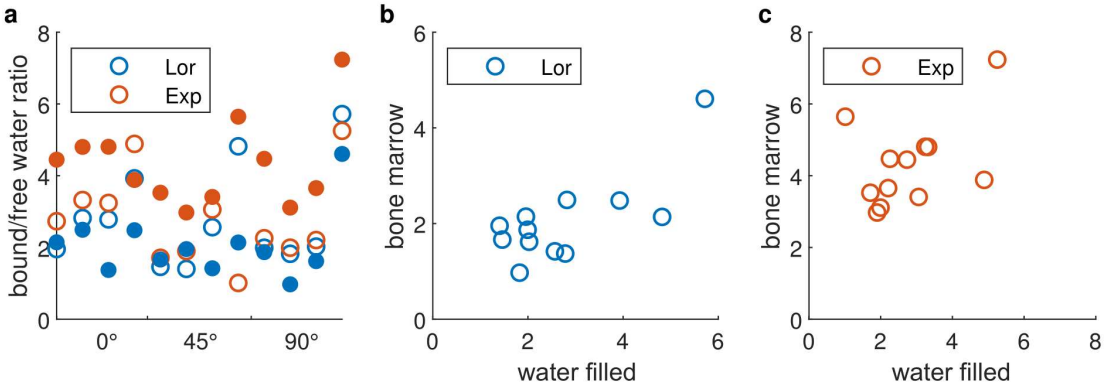

Figure 39. a. *Overview of the bound/free water ratio obtained by biexponential (blue) and two-component Lorentzian model (red) for the different orientations and the water (blank) and bone marrow (filled) filled femur. Scatter plot of the relationship between the bound water ratio obtained by the two-component Lorentzian (**b**) and biexponential (**c**) model of the water versus the bone marrow filled femur.*

Transverse relaxation times are extracted for the free and the bound water component with both models and represented in Figure 40.

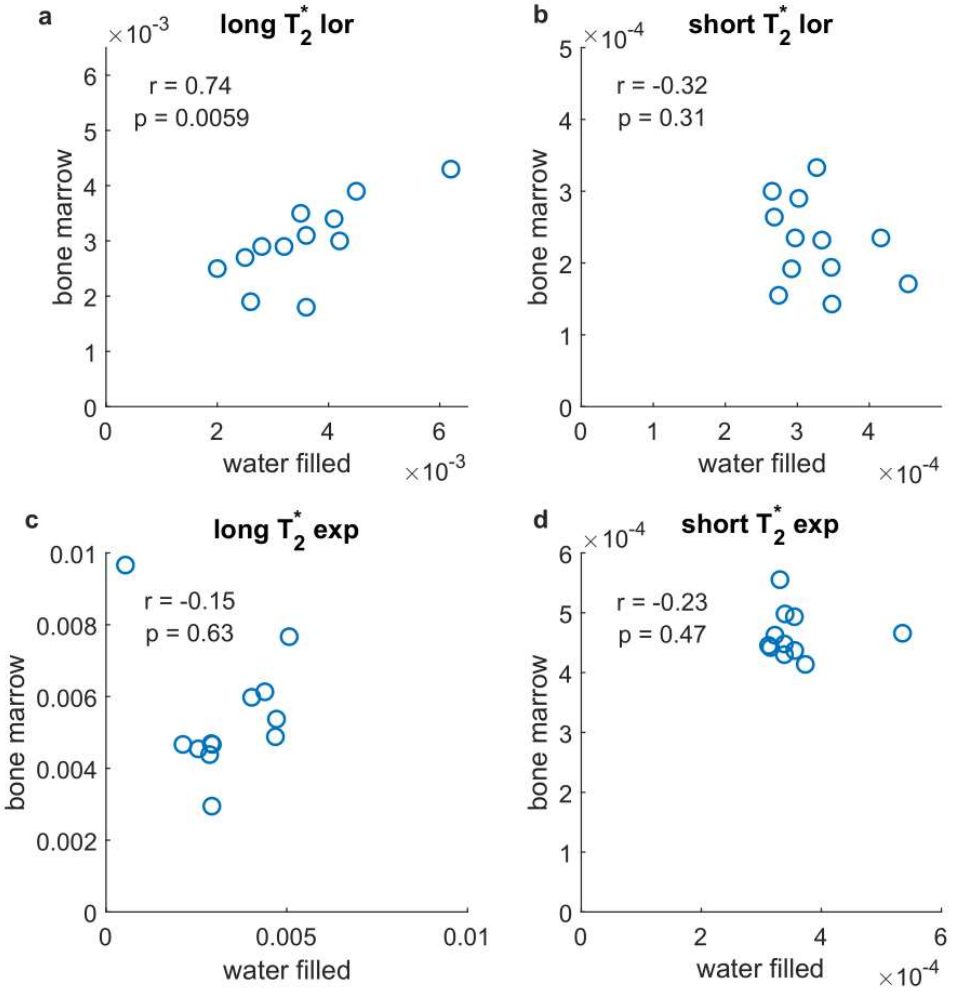

Figure 40. *a. Scatter plot of the relationship between the free water transverse relaxation time obtained by the two-component Lorentzian model of the water and the bone marrow filled femur. A very significant positive correlation is indicated. b. Scatter plot of the relationship between the bound water transverse relaxation time obtained by the two-component Lorentzian model of the water and the bone marrow filled femur. No significant correlation is indicated. c. Scatter plot of the relationship between the free water transverse relaxation time obtained by the biexponential model of the water and the bone marrow filled femur. No significant correlation is indicated. d. Scatter plot of the relationship between the bound water transverse relaxation time obtained by the biexponential model of the water and the bone marrow filled femur. No significant correlation is indicated. All relaxation times are reported in seconds.*

All relevant parameters which were extracted from the different models are summarized in Table 3 in the supporting information.

In vivo UTE-FID measurement

As illustrated by Figure 33c and d, the frequency at maximum intensity of the water resonance depends upon the ratio between water originating from Haversian canals versus Lacunae. By exploitation of the artificial methylene signal from the medullary canal as a reference (set to 1.3 ppm) an absolute determination of the water frequency is feasible. Furthermore, the resonance frequency of the two free water components relative to the methylene signal can be derived from the simulations and theoretical considerations (f_{sphere}=3.73 ppm and $f_{cylinder}$=4.49 ppm at parallel orientation). Figure 41 shows the *in vivo* spectrum extracted from the compact bone of a femur. A resonance frequency of 4.28 ppm is extracted for the water resonance at maximum intensity which is attributable to a majority of free water residing in cylindrical structures parallel to the bone axis. A comparable result (4.26 ppm) is obtained for the bovine femur at parallel orientation.

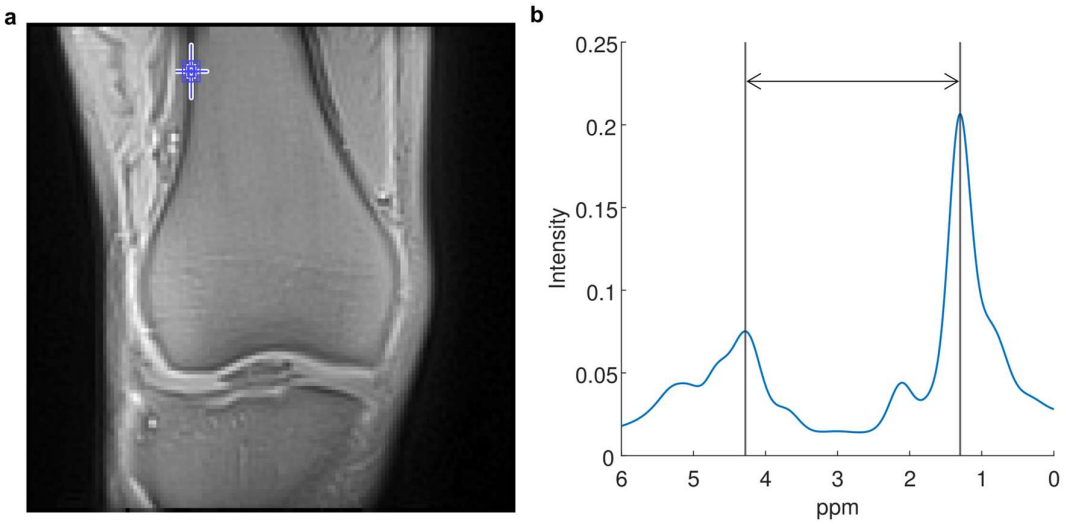

Figure 41. a. In vivo UTE magnitude image acquired at TE=0.05 ms from the knee of a healthy volunteer indicating the ROI considered for the calculation of a spatially selective UTE-FID spectrum. b. The corresponding spectrum from compact bone exhibits a dominant methylene resonance which is exploited as a reference to estimate the absolute water resonance at maximum intensity (indicated by the black lines).

Discussion

The main advantage of the new method is the accessibility of spectral information with ultra-short echo times for ROIs down to the dimensions of a single voxel. The latter is especially beneficial for the evaluation in osteoporotic cortical bone which is characterized by a decrease in thickness (114). Results show that the frequency

distribution of water signals allows for further characterization. Theoretical considerations of the geometry of the potential reservoirs of free water in cortical bone suggest that the free water signal consists of two components (cylindrical pores parallel to the bone axis and spherical pores) with deviating resonance frequencies. A splitting of these frequencies depending on the orientation of the bone in the external magnetic field is reported. Thereby parallel orientation of the bone to the magnetic field results in the widest splitting. The spectra calculated from the UTE-FID data exhibit water resonances which reveal asymmetries or slight shoulders which might be attributable to the overlap of two resonance lines. These anomalies of the water resonance predominantly occur on the upfield side for parallel orientation and on the downfield side for perpendicular orientation which would agree with a signal component of spherical water containments. A fit of the water resonance with a model consisting of three Lorentzian distributions (two for free water and one for bound water) was, thus, performed and reveals resonance frequencies which are approximately in accordance with theoretical considerations. This model shows improved conformity with the acquired water resonance compared to the two-component Lorentzian model solely differentiating bound and free water. Nevertheless, the results of the two-component Lorentzian model already confirm the postulated model of free water residing in cylindrical and spherical pores: The resonance frequencies of free water extracted from the UTE-FID spectra agree with the mean values of the two theoretically derived free water components for the different orientations of the bovine femur (Table 2). Thus, one Lorentzian curve seems to sufficiently approximate the free water resonance which represents the merging lines of spherical and cylindrical porous structures. However, it is important to mention, that this merging of two resonance lines in addition to a broadening of the spectral line also results in supplementary dephasing of the signal and, thus, an acceleration of the relaxation process in gradient echo sequences. The sensitivity to frequency shifts between the water resonances is unique to the postulated modeling by Lorentzian distributions and embodies its main advantage compared to approaches solely considering the magnitude curve of the signal decay.

Furthermore, the present study has shown that for the quantification of the fractions of bound and free water in cortical bone by UTE-based approaches, blurred off-

resonant signals originating from fatty acids must be accounted for (125; 118). These were shown to result in an oscillation of the FID and additional frequency components in the spectrum. Hence, in accordance with the findings of Lu et al. (126), an overestimation of the bound water share and the relaxation times of free and bound water results for the biexponential model. However, fat or long-T_2 saturation or the modeling of an additional fat component as reported in previous studies fulfill this purpose (126; 127; 109). In contrast, when assessing the frequency characteristics of the free water component as a marker for cortical bone structure, the artificial methylene resonance can be exploited as a frequency reference.

In vivo parallel orientation of the long bones to the MR bore and, thus, to the main magnetic field represent the common positioning. Independent thereof, this placement is also preferable for quantitative determination of the water resonance frequency. First, since the field inhomogeneities in the compact bone are least dominant for this orientation as shown by the field simulations and the measurements. Second, this positioning results in the largest frequency gap between the two proposed free water components. Thus, a characterization of the free water composition as a marker for osteoporotic changes in compact bone based on its frequency at maximum intensity is most feasible for this orientation. The recorded *in vivo* spectrum reveals a dominant methylene resonance and additional spectral components attributable to fat which must be accounted for by methods for the separation of bound and free water to reduce bias thereof. However, by application of the additional methylene resonance as a reference when evaluating the free water frequency characteristics, conclusions about the relation of water residing in cylindrical versus spherical porous structures is feasible. Therefore, the resonance frequency at maximum intensity of the water resonance relative to the methylene resonance is compared to the frequencies predicted by the simulations for cylindrical and spherical pores.

Conclusion

The consideration of chemical shift artifacts and susceptibility differences was crucial for the evaluation of complex UTE images in terms of characterizing the water compartments in cortical bone. The calculated spectra based on phase

sensitive UTE datasets allowed to test the theoretically predicted frequency and relaxation behavior of the signal components. The results matched with the hypotheses; however, additional verification is recommendable.

Measurements at parallel orientation of the axis of long bones to the main magnetic field is preferable due to reduced bulk susceptibility effects. For this orientation two free water components with different resonance frequencies might be attributable to cylindrical and spherical water-containing cavities. A potential marker for the relation of these two merging spectral lines and, thus, on bone quality might be the frequency at maximum intensity of the water resonance. For this approach, the additional methylene resonance resulting from off-resonance artifacts serves as a reference.

In contrast, the estimation of the bound water ratio requires consideration of the characterized off-resonance artifact to obtain reliable results. Two approaches to qualitatively estimate the bound to free water ratio of cortical bone were evaluated regarding their vulnerability to chemical shift artifacts. The two-component Lorentzian model generated promising results and featured a very significant positive correlation between the measurement before and after removing the bone marrow from the bovine femur.

Conflict of Interest

The authors declare no conflict of interests.

Acknowledgements

Supported in part by a grant (01GI0925) from the German Federal Ministry of Education and Research (BMBF) to the German Center for Diabetes Research (DZD e.V.)

Dr. Thomas Benkert (Siemens Healthcare AG, Erlangen, Germany) is gratefully acknowledged for technical assistance.

Supporting Information

Table 3. *Parameters of the three different fit models which were relevant for data analysis.*

0°		Water filled bone				Bone marrow filled bone			
		ROI_1	**ROI_2**	**ROI_3**	**ROI_4**	**ROI_1**	**ROI_2**	**ROI_3**	**ROI_4**
2-c. lor.	**A1**	796.7	750.3	567.3	482.1	1057	946.5	1221	831.8
	A2	1559	2116	1579	1893	2267	2361	1677	2064
	T21	0.0042	0.0035	0.0036	0.0036	0.003	0.0035	0.0018	0.0031
	T22	4.54E-04	3.47E-04	3.48E-04	2.92E-04	1.71E-04	1.94E-04	1.43E-04	1.92E-04
	t1	4.415	4.321	4.384	4.162	4.474	4.484	4.266	4.313
3-c. lor.	**A1**	393.2	286.4	259	162.4	592.5	443.7	821.9	475.1
	t1	3.995	4.477	4.502	4.321	4.582	4.586	3.999	4.41
	A2	611.6	389.1	433.2	264.9	493.5	540.6	259.3	400.5
	t2	4.464	4.138	4.052	3.977	4.046	4.19	4.619	3.896
	A3	1856	2094	1833	1712	1556	1532	1391	1310
Biexp.	**A1**	156.3	142	115.6	84.39	121.5	107.1	104.8	126.4
	T1	4.393	4.029	2.55	4.714	6.133	5.978	4.543	5.372
	A2	427	471.9	374.8	412.4	540.4	514.4	503.8	490.9
	T2	0.3395	0.3551	0.2934	0.331	0.4981	0.4935	0.6026	0.5554
45°		**Water filled bone**				**Bone marrow filled bone**			
		ROI_1	**ROI_2**	**ROI_3**	**ROI_4**	**ROI_1**	**ROI_2**	**ROI_3**	**ROI_4**
2-c. lor.	**A1**	1304	1208	715.6	565.8	1277	1182	943.8	849.3
	A2	1905	1695	1836	2727	2126	2311	1340	1817
	T21	0.0028	0.0041	0.0032	0.0062	0.0029	0.0034	0.0029	0.0043
	T22	2.74E-04	4.16E-04	2.97E-04	3.34E-04	1.55E-04	2.35E-04	2.35E-04	2.32E-04
	t1	4.48	4.773	4.447	4.451	4.73	4.717	4.708	4.622
3-c. lor.	**A1**	843.8	728.4	425.5	225.7	502.4	601.3	410.8	384.2
	t1	4.329	4.85	4.26	4.546	4.894	4.737	4.855	4.728
	A2	300.8	429.1	214.5	309.2	632.8	601	445.8	413.1
	t2	4.724	4.556	4.617	4.332	4.474	4.693	4.477	4.414
	A3	2040	1824	1928	2647	1706	2564	1260	1707
Biexp.	**A1**	236.3	226.5	128.4	269.5	169.8	169.7	162.1	108.3
	T1	2.94	4.685	2.865	0.5356	4.668	4.882	4.383	9.663
	A2	404.6	430.3	392.8	272.8	598.8	504.8	552.5	611.4
	T2	0.3121	0.3556	0.3226	0.5352	0.4453	0.437	0.4626	0.4658
90°		**Water filled bone**				**Bone marrow filled bone**			
		ROI_1	**ROI_2**	**ROI_3**	**ROI_4**	**ROI_1**	**ROI_2**	**ROI_3**	**ROI_4**
2-c. lor.	**A1**	1090	1202	945.5	518.4	1221	1515	1073	577.8
	A2	2172	2193	1914	2964	2284	1475	1738	2662
	T21	0.0025	0.0026	0.002	0.0045	0.0027	0.0019	0.0025	0.0039
	T22	2.68E-04	3.02E-04	2.65E-04	3.27E-04	2.64E-04	2.90E-04	3.00E-04	3.33E-04
	t1	4.745	4.622	4.838	4.699	4.716	4.601	4.754	4.629
3-c. lor.	**A1**	308.7	679.2	710	149.3	1082	1128	816.5	424.7
	t1	4.504	4.488	4.751	4.455	4.749	4.496	4.71	4.576
	A2	637.5	365.8	116.6	345.9	178.3	256.8	138.2	108.5
	t2	4.94	4.893	5.355	4.777	4.019	4.95	5.029	4.783
	A3	2295	2311	2000	2927	2640	1516	1993	2674
Biexp.	**A1**	192.7	228.9	178	102.8	143	176.7	160.2	97.54
	T1	2.91	2.926	2.127	5.067	4.689	2.948	4.667	7.668
	A2	435.1	456.5	392.9	539.8	639.5	549.8	585.6	705.8
	T2	0.3383	0.3384	0.3153	0.3733	0.4479	0.4301	0.4419	0.4138

Discussion

As the previous sections have shown the relaxation behavior of the MR signal is characteristic for the tissue composition. First, a potential acceleration of the relaxation process can result due to non-uniform magnetic susceptibility which causes inhomogeneities of the magnetic field. This was shown exemplary for a water signal originating from inflamed adipose tissue (Part I). Second, a decrease of relaxation time is also detectable in presence of macromolecules due to a reduction of molecular motion. While local fields are almost completely balanced in the presence of rapid motion, a reduction of the latter results in relevant field fluctuations and an acceleration of the relaxation process (128). This effect is mainly responsible for the short transverse relaxation times of fibrotic tissue, bone and tendon (Part II and III). Especially water which is bound to these macromolecules features restricted motion and, thus, short relaxation times. Therefore, this water compartment can - based on its relaxation time - be differentiated from free water. In some tissues such as bone these water components exhibit different medical implications, wherefore a determination of their ratio is desired. Furthermore, bulk susceptibility effects must be considered for the free water component as shown in Part III. Independent of the source which causes the acceleration of the relaxation process, sequences with ultra-short echo times are preferable for MR signals with short relaxation times. Thus, a prototypical 3D stack of spiral trajectories UTE sequence was applied in Part II and III and a method is described which allows for a pixelwise calculation of spectra from a dataset of phase sensitive images. All studies were performed on a 3T whole-body imager. The following section summarizes the conclusions of the different studies and provides insights on their limitations as well as an outlook.

The first part focused on a potential water component in adipose tissue which might provide an indicator for underlying inflammation. The aim of the study was to evaluate whether the measurement of the signal originating from this potential component by MR techniques is feasible. The geometry of the water accumulated in the extracellular space between adipocytes was replicated by finite element simulations and phantom measurements to access the bulk susceptibility shift induced magnetic field inhomogeneities. Based thereon a prediction of the

relaxation behavior and the line shape was feasible. A T_2^* relaxation time between 5 ms and 8 ms at 3 T was extracted from both, simulations and phantom measurements. These relate to a spectral line width of the water resonance of approximately 40 Hz to 70 Hz. Even faster relaxation behavior and broader lines might be observable *in vivo* due to additional field disturbances caused by iron uptake in the macrophages. Thus, short TEs are required for gradient echo measurements of the water component and even recommendable for spin echo sequences due to diffusion effects in the small water areas with high field gradients. Furthermore, it must be considered, that the line shape is non-Lorentzian and, thus, the signal decay deviates from a mono-exponential decay. For this reason, deviations for multi-echo Dixon approaches are expectable which rely on an exponential behavior of the signal decay of the individual frequency components. Additionally, the difference of the relaxation times between water and fat must be accounted for. These are also relatable to the difference between the line width of the water resonance compared to that obtained for the fat resonances in the spectrum acquired from a porcine subcutaneous adipose tissue sample. While a line width of approximately 15 Hz was reported for the methylene resonance of fatty acids, that of water amounted to 70 Hz, which corresponds well with the results obtained by simulations and phantom measurements. Nevertheless, the consideration of porcine subcutaneous adipose tissue without the estimation of inflammatory markers exerts a limitation of the study. However, studies have shown that the adipose tissue of swine report no obesity or diet induced changes of inflammatory status and macrophage content, which is highest in subcutaneous adipose tissue (70; 69). In contrast, the number of water-rich macrophages was shown to increase in human adipose tissue in presence of inflammation, which was especially present in visceral adipose tissue in connection with obesity (62; 63; 64; 65; 66). If the reported results are confirmed by further MR measurements in human adipose tissue, water signal accessed by MR sequences with short TEs might serve as non-invasive biomarker for inflammation thereof.

As concluded previously, short relaxation times require sequences with short TEs. A sequence with ultra-short TEs was exploited in Part II for the calculation of spatially selective spectra based on phase sensitive images. The newly developed method was evaluated on aqueous collagen type 1 and 3 solutions. The resulting

spectra are in accordance with those obtained by a non-localized pulse-acquire FID sequence applied on a sphere filled with the same solution. Furthermore, the collagen signal pattern exhibits a positive correlation with the concentration. Based on the spectra a collagen signal model was extracted which served the differentiation of water and collagen in an approach comparable to the Dixon method for fat and water separation. This approach yielded a detectability and quantifiability of movable collagen chains starting at a mass percent concentration of approximately 2-4%. Compared to a previous study by Siu et al. with a sensitivity starting at 10% this improvement opens new fields of application such as the staging of liver fibrosis where collagen content is reported to range from 2% to more than 8% (31; 98). However, it remains to be verified whether a similar sensitivity also results for structured collagen chains as present in fibrotic tissue. Furthermore, the underlying method solely considers water and collagen signals, wherefore a supplementation by a fat signal pattern is crucial for the application in the liver. As an alternative, a detection of collagen in the liver or other organs might be performed based on the proposed spectroscopy technique where for example the collagen resonances downfield of the water resonance which are not concealed by a potential dominant methylene resonance might serve as collagen indicator. The applicability of the UTE-FID spectroscopy technique *in vivo* was verified on a data set from the knee of a healthy volunteer: A spectrum extracted from the subcutaneous adipose tissue revealed the typical frequency pattern which is to be expected in adipose tissue. The presented method enables a calculation of pixelwise spectra which with the applied sequence parameters results in a minimal possible ROI size of 1x1x2.8 mm^3. In addition to the ultra-short TE of 0.05 ms, this represents the main advantage over other techniques such as the 2D MRSI spectroscopy presented by Chang et al. (102). Nevertheless, UTE imaging is also associated with disadvantages as for example stress on the gradient system wherefore correction for temporal and spatial field drift effects are required. However, the new method has a wide range of potential applications since it enables the acquisition of spatially resolved information on the frequency composition due to chemical or bulk susceptibility shifts despite short relaxation times.

The benefits of the acquisition of pixelwise frequency spectra of the MR signal with ultra-short echo times were pointed out in Part III based on the application on cortical bone. The main advantage is the accessibility of the frequency distribution characteristics of the water signal. FEM and analytical simulations indicate that the free water signal consists of two merging water resonances. One originating from spherical pores and a second due to free water from cylindrical structures (mainly the Haversian canals). For the frequency of the latter an orientation dependent frequency shift results. Asymmetries and slightly pronounced shoulders might embody this splitting in the acquired spatially selective spectra and correspond with the predicted frequencies. Nevertheless, further measurements are necessary to review the characteristics of the free water component and to address potential medical fields of application. However, when modeling the free water component by one Lorentzian distribution, the resulting resonance frequency corresponds well with the average of the two predicted frequencies (for spherical and cylindrical water containing pores). This finding strengthens the postulated model of free water. The frequency difference between the two components reveals the largest value at parallel orientation of the cylinder axis to the main magnetic field. Since the majority of canals is oriented parallel to the bone axis in long bones, a frequency difference of approximately 100 Hz is predicted for the common positioning of the patient axial in the bore of the MR imager. Nevertheless, this position is preferable since the magnetic field simulations for the long bone geometry exhibit the most homogeneous field distribution for parallel orientation. Therefore, bulk magnetic susceptibility shifts dependent on the placement of the ROI and field inhomogeneity effects are neglectable. It was shown that the frequency of the water resonance line at maximal intensity might serve as an indicator of the ratio of free water from spherical versus cylindrical pores. However, an absolute determination of the water resonance frequency requires a reference. In an *in vitro* experiment with removed bone marrow, a central voxel in the water filled medullary canal served as reference. For *in vivo* measurements the methylene resonance of the bone marrow is suggested as a reference. It was shown that chemical shift induced off-resonances for the underlying UTE sequence occur due to off-resonance blurring. Thus, the methylene resonance which is dominant in the bone marrow is also detectable in the cortical bone. This signal is present as an oscillation in the magnitude curve of the FID and as an additional spectral line at approximately

1.3 ppm in the spectrum. While this additional resonance provides a reference for the frequency determination of the water resonance it might bias the determination of the bound water share. Bi-exponential models were found by Lu et al. to overestimate the bound water fraction in the presence of a methylene induced off-resonance (126). This finding is in accordance with the results reported in Part III. While the bound water share of the empty bone was estimated to approximately 70% by the bi-exponential approach and a fit of a two-component Lorentzian model to the water resonance, an overestimation to 80% was obtained by the bi-exponential model in the presence of bone marrow. Meanwhile a spectrum-based approach sparing the frequency range of the CH_2 resonance yields a bound water fraction of 65%. In conclusion, an unbiased determination of the fraction of bound water requires consideration of the characterized off-resonance blurring.

All three parts indicate potential new biomarkers in different tissues which depend upon MR measurements with (ultra-)short echo times. Furthermore, they require a resolution of the frequency spectrum to distinguish signal components which exhibit different frequencies or frequency distributions either due to chemical shift or bulk magnetic susceptibility shift. Both requests are met by the newly introduced spatially selective UTE-FID (Part II). Assumably, this method will also contribute to other fields of application with comparable requirements.

References

1. **Pauli, W.** Entdeckung des »Kernspins« zur Erklärung der Hyperfeinstruktur der Atomspektren. *Naturwissenschaften.* 1924, Vol. 12.

2. **OECD.** Magbetic resonance imaging (MRI) exams (indicator). [Online] 2022. [Cited: 10 5, 2022.]

3. **NobelPrize.org.** Press release. *Nobel Prize Outreach AB 2022.* [Online] [Cited: 10 10, 2022.] https://www.nobelprize.org/prizes/medicine/2003/press-release/.

4. **Partain, C L.** The 2003 Nobel Prize for MRI: Significance and impact. *J Magn Reson.* 2004, Vol. 19, 5, pp. 515-526.

5. **NobelPrize.org.** The Nobel Prize in Physics 1944. *Nobel Prize Outreach AB 2022.* [Online] [Cited: 10 7, 2022.] https://www.nobelprize.org/prizes/physics/1944/summary/.

6. **Rabi, I I, et al.** A new method of measuring nuclear magnetic moment. *Phys Rev.* 1938, Vol. 53, 4, p. 318.

7. **Purcell, E M, Torrey, H C and Pound, R V.** Resonance absorption by nuclear magnetic moments in solids. *Phys Rev.* 1946, Vol. 69, 1-2, pp. 37–38.

8. **Bloch, F.** Nuclear induction. *Phys Rev.* 1946, Vol. 70, 7-8, pp. 460-474.

9. **Bloch, F, Hansen, W W and Packard, M E.** The nuclear induction experiment. *Phys Rev.* 1946, Vol. 70, 7-8, pp. 474-485.

10. **NobelPrize.org.** The Nobel Prize in Physics 1952. *Nobel Prize Outreach AB 2022.* [Online] [Cited: 10 7, 2022.] https://www.nobelprize.org/prizes/physics/1952/summary/.

11. —. Richard R. Ernst – Facts. *Nobel Prize Outreach AB 2022.* [Online] [Cited: 10 7, 2022.] https://www.nobelprize.org/prizes/chemistry/1991/ernst/facts/.

12. —. Kurt Wüthrich – Facts. *Nobel Prize Outreach AB 2022.* [Online] [Cited: 10 7, 2022.] https://www.nobelprize.org/prizes/chemistry/2002/wuthrich/facts/.

13. **Lauterbur, P C.** Image formation by induced local interactions: examples employing nuclear magnetic resonance. *Nature.* 1973, Vol. 242, 3-6, pp. 190-191.

14. **Mansfield, P and Grannell, P K.** NMR 'diffraction' in solids. *J Phys C: Solid State Physics.* 1973, Vol. 6, 22, pp. L422–L426.

15. **Damadian, R.** Tumor detection by nuclear magnetic resonance. *Science.* 1971, Vol. 171, 3976, pp. 1151–1153.

16. **Endo, M.** History of medical physics. *Radiol Phys Technol.* 2021, Vol. 14, 4, pp. 345-357.

17. **Ladd, M E, et al.** Magnetresonanztomographie und -spektroskopie. [book auth.] W Schlegel, C P Karger and O Jäkel. *Medizinische Physik: Grundlagen - Bildgebung - Therapie - Technik.* s.l. : Springer Spektrum, 2018.

18. **Kachelrieß, M.** Computertomographie. [book auth.] W Schlegel, C P Karger and O Jäkel. *Medizinische Physik: Grundlagen - Bildgebung - Therapie - Technik.* s.l. : Springer Spektrum, 2018.

19. **Iniewski, K.** *Medical imaging: principles, detectors, and electronics.* s.l. : John Wiley & Sons Ltd., 2009.

20. **Elster, A D.** An index system for comparative parameter weighting in MR imaging. *J Comput Assist Tomogr.* 1988, Vol. 12, 1, pp. 130-134.

21. **Yokoo, T, et al.** A quantitative approach to sequence and image weighting. *J Comput Assist Tomogr.* 2010, Vol. 34, 3, pp. 317-331.

22. **Dixon, W T.** Simple proton spectroscopic imaging. *Radiology.* 1984, Vol. 153, 1, pp. 189-194.

23. **Ma, J.** Dixon Techniques for Water and Fat Imaging. *J Magn Reson Imaging.* 2008, Vol. 28, 3, pp. 543–558.

24. **Hood, M N, et al.** Chemical shift: the artifact and clinical tool revisited. *Radiographics.* 1999, Vol. 19, 2, pp. 357-371.

25. **Schick, F, et al.** Comparison of localized proton NMR signals of skeletal muscle and fat tissue in vivo: two lipid compartments in muscle tissue. *Magn Reson Med.* 1993, Vol. 29, 2, pp. 158-167.

26. **Bergin, C J, Glover, G H and Pauly, J M.** Lung parenchyma: magnetic susceptibility in MR imaging. *Radiology.* 1991, Vol. 180, 3, pp. 845-848.

27. **Togao, O, et al.** Ultrashort echo time (UTE) MRI of the lung: assessment of tissue density in the lung parenchyma. *Magn Reson Med.* 2010, Vol. 64, 5, pp. 1491-1498.

28. **Bergin, C J, Pauly, J M and Macovski, A.** Lung parenchyma: projection reconstruction MR imaging. *Radiology.* 1991, Vol. 179, 3, pp. 777-781.

29. **Ma, Y-J, et al.** Quantitative Ultrashort Echo Time (UTE) Magnetic Resonance Imaging of Bone: An Update. *Front Endocrinol.* 2020, Vol. 11.

30. **Chang, E Y, Du, J and Chung, C B.** UTE Imaging in the Musculoskeletal System. *J Magn Reson Imaging.* 2015, Vol. 41, 4, pp. 870–883.

31. **Siu, A G, et al.** Characterization of the ultrashort-TE (UTE) MR collagen signal. *NMR Biomed.* Oct 2015, Vol. 28, 10, pp. 1236-1244.

32. **de Graaf, R A.** *In Vivo NMR Spectroscopy: Principles and Techniques.* 2. s.l. : John Wiley & Sons Ltd., 2007.

33. **Neelavalli, J and Cheng, Y-C N.** Magnetic Susceptibility. [book auth.] E M Haacke and J R Reichenbach. *Susceptibility Weighted Imaging in MRI: Basic Concepts and Clinical Applications.* s.l. : Wiley-Blackwell, 2011.

34. **Levitt, M H.** *Spin dynamics: basics of nuclear magnetic resonance.* s.l. : John Wiley & Sons Ltd., 2001.

35. **Brown, R W, Cheng, Y-C N and Haacke, E M.** *Magnetic resonance imaging: physical principles and sequence design.* 2. s.l. : Wiley Blackwell, 2014.

36. **Dale, B M, Brown, M A and Semelka, R C.** *MRI Basic Principles and Applications.* 5. s.l. : John Wiley & Sons, Ltd, 2015.

37. **Hendee, W R and Ritenour, E R.** *Medical Imaging Physics.* 4. s.l. : Wiley Blackwell, 2010.

38. **Freude, D.** Nuclear Magnetic Resonance. *Spectroscopy.* s.l. : University Leipzig, 2006.

39. **Jacobsen, N E.** *NMR spectroscopy explained: simplified theory, applications and examples for organic chemistry and structural biology.* s.l. : John Wiley & Sons Ltd., 2007.

40. **Becker, E D.** *High Resolution NMR - Theory and chemical applications.* 3. s.l. : Academic Press, 2000.

41. **Kirkby, L A.** *Physik - Der Studienbegleiter.* s.l. : Springer Spektrum, 2012.

42. **Cheng, Y C N, Neelavalli, J and Haacke, E M.** Limitations of calculating field distributions and magnetic susceptibilities in MRI using a Fourier based method. *Phys Med Biol.* 2009, Vol. 54, 5, pp. 1169-89.

43. **Durrant, C J, Hertzberg, M P and Kuchel, P W.** Magnetic susceptibility: further insights into macroscopic and microscopic fields and the sphere of Lorentz. *Concepts Magn Reson.* 2003, Vol. 18A, 1, pp. 72-95.

44. **Yablonskiy, D A.** Quantitation of Intrinsic Magnetic Susceptibility-Related Effects in a Tissue Matrix Phantom Study. *Magn Reson Med.* 1998, Vol. 39, 3, pp. 417-428.

45. **Koch, M K, Rothman, D L and de Graaf, R A.** Optimization of static magnetic field homogeneity in the human and animal brain in vivo. *Prog Nucl Magn Reson Spectrosc.* 2009, Vol. 54, 2, pp. 69-96.

46. **Ziener, C H, et al.** Diffusion effects on the CPMG relaxation rate in a dipolar field. *J Magn Reson.* 2010, Vol. 202, 1, pp. 38-42.

47. **Schick, F.** Sequenzen in der MRT - Teil 1. *Radiologe.* 2006, Vol. 7, pp. 615-627.

48. **Hidalgo-Tobon, S S.** Theory of gradient coil design methods for magnetic resonance imaging. *Concepts Magn Reson Part A Bridg Educ Res.* 2010, Vol. 36A, 4, pp. 223-242.

49. **Schick, F.** Sequenzen in der MRT - Teil 2. *Radiologe.* 2006, Vol. 9, pp. 803 - 817.

50. **Hui, S C N, et al.** Frequency drift in MR spectroscopy at 3T. *NeuroImage.* Nov 2021, Vol. 241.

51. **Qian, Y and Boada, F E.** Acquisition-weighted stack of spirals for fast high-resolution three-dimensional ultra-short echo time MR imaging. *Magn Reson Med.* 2008, Vol. 60, 1, pp. 135-145.

52. **Schick, F.** Grundlagen der Magnetresonanztomographie. *Radiologe.* 2005, Vol. 45, p. 69.88.

53. **Robson, M D, et al.** Magnetic Resonance: An Introduction to Ultrashort TE (UTE) Imaging. *J Comput Assist Tomogr.* 2003, Vol. 27, 6, pp. 825-846.

54. **Ma, Y-J, et al.** Ultrashort echo time (UTE) magnetic resonance imaging of myelin: technical developments and challenges. *Quant Imaging Med Surg.* 2020, Vol. 10, 6, pp. 1186-1203.

55. **Fischer, A and Schick, F.** Towards detection of inflammation in adipose tissue: Microscopic field simulations to estimate water signal properties. *Z Med Phys.* 2021, Vol. 13, 4, pp. 394-402.

56. **WHO.** Global and regional trends by WHO regions,overweight: 1990–2019. [Online] 2019. [Cited: 5 5, 2020.] https://apps.who.int/gho/data/view.main.NUTWHOOVERWEIGHTv.

57. **Wensveen, F M, et al.** Nk cells link obesity-induced adipose stress to inflammation and insulin resistance. *Nat Immunol.* 2015, Vol. 16, 4, pp. 376-385.

58. **Tordjman, J, Guerre-Millo, M and Clément, K.** Adipose tissue inflamma-tion and liver pathology in human obesity. *Diabetes Metab.* 2008, Vol. 34, 6, pp. 658-663.

59. **Alexopoulos, N, Katritsis, D and Raggi, P.** Visceral adipose tissue as a source of inflammation and promoter of atherosclerosis. *Atherosclerosis.* 2014, Vol. 233, 1, pp. 104-112.

60. **Berg, A H and Scherer, P E.** Adipose tissue, inflammation, and cardiovascular disease. *Circ Res.* 2005, Vol. 96, 9, pp. 939-949.

61. **Spalding, K L, et al.** Dynamics of fat cell turnover in humans. *Nature.* 2008, Vol. 453, 7196, pp. 783-787.

62. **Ye, J, et al.** Hypoxia is a potential risk factor for chronic inflammation and adiponectin reduction in adipose tissue of ob/ob and dietary obese mice. *J Clin Invest.* 2007, Vol. 293, 4, pp. 1118-1128.

63. **Weisberg, S P, et al.** Obesity is associated with macrophage accumulation in adipose tissue. *J Clin Invest.* 2003, Vol. 112, 12, pp. 1769-1808.

64. **Park, S-H, et al.** Ikkβ is essential for adipocyte survivaland adaptive adipose remodeling in obesity. *Diabetes.* 2016, Vol. 65, 6, pp. 1616-1629.

65. **Cinti, S, et al.** Adipocyte death defines macrophage localization and function in adipose tissue of obese mice and humans. *J Clin Invest.* 2005, Vol. 46, 11, pp. 2347-2355.

66. **Murano, I, et al.** Dead adipocytes, detected as crown-like structures, are prevalent in visceral fat depots of genetically obese mice. *J Lipid Res.* 2008, Vol. 49, 7, pp. 1562-1568.

67. **Schenck, J F.** The role of magnetic susceptibility in magnetic resonance imaging: Mri magnetic compatibility of the first and second kinds. *Med Phys.* 1996, Vol. 23, 6, pp. 815-850.

68. **Hopkins, J A and Wehrli, F W.** Magnetic susceptibility measurement of insoluble solids by NMR: magnetic susceptibility of bone. *Magn Reson Med.* 1997, Vol. 37, 4, pp. 494-500.

69. **Faris, R J, et al.** Inflammation in response to n3 fatty acids in a porcine obesity model. *Comp Med.* 2012, Vol. 62, 2, pp. 459-503.

70. **Vieira-Potter, V J, et al.** Disconnect between adipose tissue inflammation and cardiometabolic dysfunction in ossabaw pigs. *Obesity (Silver Spring).* 2015, Vol. 23, 12, pp. 2421-2429.

71. **Fischer, A, et al.** Spatially resolved free-induction decay spectroscopy using a 3D ultra-short echo time multi-echo imaging sequence with systematic echo shifting and compensation of B0 field drifts. *Magn Reson Med.* 2022, Vol. 87, 5, pp. 2099-2110.

72. **Inglese, M, et al.** Global average gray and white matter N-acetylaspartate concentration in the human brain. *NeuroImage.* Jun 2008, Vol. 41, 2, pp. 270-276.

73. **Kaflak-Hachulska, A, Samoson, A and Kolodziejski, W.** 1 H MAS and 1 H --> 31 P CP/MAS NMR study of human bone mineral. *Calcif Tissue Int.* Oct 2003, Vol. 73, 5, pp. 476-486.

74. **Giapitzakis, I-A, Avdievich, N and Henning, A.** Characterization of macromolecular baseline of human brain using metabolite cycled semi-LASER at 9.4T. *Magn Reson Med.* Aug 2018, Vol. 80, 2, pp. 462-473.

75. **Murali-Manohar, Saipavitra, et al.** T2 relaxation times of macromolecules and metabolites in the human brain at 9.4 T. *Magn Reson Med.* Aug 2020, Vol. 84, 2, pp. 542-558.

76. **Boucneau, Tanguy, et al.** In vivo characterization of brain ultrashort-T2 components. *Magn Reson Med.* Aug 2018, Vol. 80, 2, pp. 726-735.

77. **Leutritz, Tobias, et al.** Accurate quantification of water–macromolecule exchange induced frequency shift: Effects of reference substance. *Magn Reson Med.* Jan 2013, Vol. 69, 1, pp. 263-268.

78. **Luo, J, et al.** Protein-induced water 1H MR frequency shifts: Contributions from magnetic susceptibility and exchange. *J Magn Reson.* Jan 2010, Vol. 202, 1, pp. 102-108.

79. **Lee, Jongho, et al.** So you want to image myelin using MRI: An overview and practical guide for myelin water imaging. *J Magn Reson Imaging.* Feb 2021, Vol. 53, 2, pp. 360-373.

80. **Filho, Guinel H, et al.** Quantitative characterization of the achilles tendon in cadaveric specimens: T1 and T2* measurements using ultrashort-TE MRI at 3T. *AJR Am J Roentgeno.* Mar 2009, Vol. 192, 3, pp. W117-W124.

81. **Bogner, W, et al.** High-resolution mapping of human brain metabolites by free induction decay 1H MRSI at 7T. *J Magn Reson.* Jun 2012, Vol. 25, 6, pp. 873-882.

82. **Nassirpour, Sahar, et al.** Compressed sensing for high-resolution nonlipid suppressed 1H FID MRSI of the human brain at 9.4T. *Magn Reson Med.* Dec 2018, Vol. 80, 6, pp. 2311-2325.

83. **Du, J, Takahashi, A M and Chung, C B.** Ultrashort TE spectroscopic imaging (UTESI): Application to the imaging of short T2 relaxation tissues in the musculoskeletal system. *J Magn Reson Imaging.* Feb 2009, Vol. 29, 2, pp. 414-421.

84. **Bydder, G.** Review. The Agfa Mayneord lecture: MRI of short and ultrashort T2 and T2* components of tissues, fluids and materials using clinical systems. *Br J Radiol.* Dec 2011, Vol. 84, 1008, pp. 1067-1082.

85. **Araujo, Ericky C A, et al.** Quantitative ultrashort TE imaging of the short-T2 components in skeletal muscle using an extended echo-subtraction method. *Magn Reson Med.* Sep 2017, Vol. 78, 3, pp. 997-1008.

86. **Posse, S, et al.** MR spectroscopic imaging: Principles and recent advances. *J Magn Reson Imaging.* Jun 2013, Vol. 37, 6, pp. 1301-1325.

87. **El-Sharkawy, AbdEl Monem, et al.** Monitoring and correcting spatio-temporal variations of the MR scanner's static magnetic field. *MAGMA.* Nov 2006, Vol. 19, 5, pp. 223-236.

88. **Tkác, I, et al.** In vivo 1H NMR spectroscopy of rat brain at 1 ms echo time. *Magn Reson Med.* Apr 1999, Vol. 41, 4, pp. 649-656.

89. **Mugler, J P, et al.** *Breath-hold UTE lung imaging using a stack-of-spirals acquisition.* Toronto : s.n., 2015.

90. **Burg, J P.** *A new analysis technique for time series data.* Eschede : s.n., 1968.

91. **Diefenbach, Maximilian N, Liu, Chunlei and Karampinos, Dimitrios C.** Generalized parameter estimation in multi-echo gradient-echo-based chemical species separation. *Quant Imaging Med Surg.* Mar 2020, Vol. 10, 3, pp. 554-567.

92. **Reeder, S B, Hu, H H and Sirlin, C B.** Proton density fat-fraction: A standardized MR-based biomarker of tissue fat concentration. *J Magn Reson Imaging.* Nov 2012, Vol. 36, 5, pp. 1011-1014.

93. **Wishart, D S, et al.** HMDB 4.0 - The Human Metabolome Database for 2018. [Online] Nucleic Acids Res, Jan 2018. http://www.hmdb.ca/.

94. **Winkler, Tobias, et al.** *Behavior of the signal components of collagen solutions in vitro using UTE-MRI and MRS sequences.* Montreal : s.n., 2019. #2258.

95. **Zeisberg, A and Kalluri, R.** Cellular mechanisms of tissue fibrosis. 1. common and organ-specific mechanisms associated with tissue fibrosis. *Am J Physiol Cell Physiol.* Feb 2013, Vol. 304, 4, pp. 216-225.

96. **Rockey, D C, Bell, P D and Hill, J A.** Fibrosis - a common pathway to organ injury and failure. *N Engl J Med.* Mar 2015, Vol. 372, 12, pp. 1138-1149.

97. **Mahdy, M A A.** Skeletal muscle fibrosis: an overview. *Cell Tissue Res.* Mar 2019, Vol. 375, 3, pp. 575-588.

98. **Aycock, Richard S and Seyer, Jerome M.** Collagens of normal and cirrhotic human liver. *Connect Tissue Res.* Jan 1989, Vol. 23, 1, pp. 19-31.

99. **Ellis, E L and Mann, D A.** Clinical evidence for the regression of liver fibrosis. *J Hepatol.* May 2012, Vol. 56, 5, pp. 1171-1180.

100. **Bataller, R and Brenner, D A.** Liver fibrosis. *J Clin Invest.* Feb 2005, Vol. 115, 2, pp. 209-218.

101. **Petitclere, L, et al.** Liver fibrosis: Review of current imaging and MRI quantification techniques. *J Magn Reson Imaging.* May 2017, Vol. 45, 5, pp. 1276-1295.

102. **Chang, P, et al.** Non-water-suppressed 1H FID-MRSI at 3T and 9.4T. *Magn Reson Med.* Aug 2018, Vol. 80, 2, pp. 442-451.

103. **Timmins, P A and Wall, J C.** Bone Water. *Calc Tiss Res.* 1977, Vol. 23, pp. 1-5.

104. **Su, N, et al.** Bone function, dysfunction and its role in diseases including critical illness. *Int J Biol Sci.* 2019, Vol. 15, 4, pp. 776-787.

105. **Boskey, AL.** Bone composition: relationship to bone fragility and antiosteoporotic drug effects. *BoneKEy Reports.* 2013, Vol. 2.

106. **Granke, M, Does, D M and Nyman, J S.** The role of water compartments in the material properties of cortical bone. *Calcif Tissue Int.* 2015, Vol. 97, 3, pp. 292-307.

107. **Horch, R A, et al.** Non-invasive predictors of human cortical bone mechanical properties: T2-discriminated 1H NMR Compared with high resolution x-ray. *PLoS ONE.* 2011, Vol. 6, 1.

108. **Diaz, E, et al.** Ultrashort echo time spectroscopic imaging (UTESI): an efficient method for quantifying bound and free water. *NMR Biomed.* 2012, Vol. 25, 1, pp. 161-168.

109. **Li, S, et al.** Effects of inversion time on inversion recovery prepared ultrashort echo time (IR-UTE) imaging of bound and pore water in cortical bone. *NMR Biomed.* 2015, Vol. 28, 1, pp. 70–78.

110. **Martin, R B.** Porosity and specific surface of bone. *Crit Rev Biomed Eng.* 1984, Vol. 3, pp. 179-222.

111. **Marotti, G, et al.** Structure Function Relationships in the Osteocyte. *Italian J Mineral and Electrolyte Metabolism.* 1990, Vol. 4, pp. 93-106.

112. **Núñez, J A, et al.** Simultaneous visualisation of calcified bone microstructure and intracortical vasculature using synchrotron X-ray phase contrast enhanced tomography. *Sci Rep.* 2017, Vol. 7, 13289.

113. **Wang, X and Ni, Q.** Determination of cortical bone porosity and pore size distribution using a low field pulsed NMR approach. *J Orthop.* 2003, Vol. 21, 2, pp. 312-319.

114. **Benfu, C, Xueming, T and Hui, L.** Osteoclastic resorption of Haversian systems in cortical bone of femoral neck in aged women - a scanning electron microscopy study. *Chin Med J.* 1996, Vol. 109, 9, pp. 705-710.

115. **Bae, W C, et al.** Quantitative ultrashort echo time (UTE) MRI of human cortical bone: correlation with porosity and biomechanical properties. *J Bone Miner Res.* 2012, Vol. 27, 4, pp. 848-857.

116. **Li, S, et al.** Ultrashort echo time bi-component analysis of cortical bone - a field dependence study. *Magn Reson Med.* 2014, Vol. 71, 3, pp. 1075–1081.

117. **Henkelman, R M, Stanisz, G J and Graham, G J.** Magnetization transfer in MRI: a review. *NMR Biomed.* 2001, Vol. 14, 2, pp. 57-64.

118. **Delattre, B M A, et al.** Spiral demystified. *Magn Reson Imaging.* 2010, Vol. 28, 6, pp. 862-881.

119. **Zhong, X, et al.** Liver fat quantification using a multi-step adaptive fitting approach with multi-echo GRE imaging. *Magn Reson Med.* 2014, Vol. 72, 5, pp. 1353-1365.

120. **Bashir, M R, et al.** Quantification of hepatic steatosis with a multistep adaptive fitting MRI approach: Prospective validation against MR spectroscopy. *AJR Am J Roentgeno.* 2015, Vol. 204, 2, pp. 297-306.

121. **Yokoo, T, et al.** Estimation of hepatic proton-density fat fraction by using MR imaging at 3.0 T. *Radiology.* 2011, Vol. 258, 3, pp. 749-759.

122. **Min, J, et al.** Estimation of hepatic fat fraction using modified Dixon magnetic resonance imaging techniques: Effect of liver cirrhosis. *Clin Imaging.* 2018, Vol. 51, pp. 50-58.

123. **Hamilton, G, et al.** In vivo characterization of the liver fat 1H MR spectrum. *NMR Biomed.* 2011, Vol. 24, 7, pp. 784-790.

124. **Sturniolo, S and Yates, J R.** The Lorentz sphere visualized. *J Chem Phys.* 2019, Vol. 150.

125. **King, K F.** Spiral scanning with anisotropic field of view. *Magn Reson Med.* 2005, Vol. 39, 3, pp. 448-456.

126. **Lu, X, et al.** Three-dimensional ultrashort echo time imaging with tricomponent analysis for human cortical bone. *Magn Reson Med.* 2019, Vol. 82, 1, pp. 348-355.

127. **Jerban, S, et al.** Correlations of cortical bone microstructural and mechanical properties with water proton fractions obtained from ultrashort echo time (UTE) MRI tricomponent T2* model. *NMR Biomed.* 2020, Vol. 33, 3, p. e4233.

128. **Mitchell, D G, et al.** The biophysical basis of tissue contrast in extracranial MR imaging. *AJR Am J Roentgenol.* 1987, Vol. 149, 4, pp. 831-837.

Acknowledgements

First and foremost, I would like to express my sincere gratitude to my supervisor Prof. Dr. Dr. Fritz Schick for his invaluable feedback, support, and guidance throughout the last years, which enabled this thesis in the first place.

Besides I would like to extend my thanks to Prof. Dr. Klaus Scheffler for his willingness to provide the second report.

I also owe gratitude to Jürgen, Petros and Günter, who always had an open ear for my questions and problems and supported me with their valuable knowledge.

Furthermore, I would like to thank the entire Section on Experimental Radiology for creating a working atmosphere which I will deeply miss. Special thanks are addressed to my office colleagues Jessie, Mystele, Emilie and Leonie.

I also owe thanks to my sister Silke for being my greatest inspiration and role model as well as to my parents for enabling my dual career in sports and academics by always having my back and supporting every step I took.

Last but not least, I want to thank Bernd. I want to thank him for always believing in me, his unconditional support and having no days off.